Advancing melt electrospinning writing for fabrication of biomimetic structures

Dissertation zur Erlangung des naturwissenschaftlichen Doktorgrades
der Julius-Maximilians-Universität Würzburg

vorgelegt von

Gernot Hochleitner

aus Erlangen

Würzburg 2017

Eingereicht bei der Fakultät für Chemie und Pharmazie am

14.08.2017

Gutachter der schriftlichen Arbeit

1. Gutachter: Prof. Dr. rer. nat. Jürgen Groll

2. Gutachter: Prof. Dr. rer. nat. Robert Luxenhofer

Prüfer des öffentlichen Promotionskolloquiums

1. Prüfer: Prof. Dr. rer. nat. Jürgen Groll

2. Prüfer: Prof. Dr. rer. nat. Robert Luxenhofer

3. Prüfer: Prof. Dr. Dr. Lorenz Meinel

4. Prüfer: PD Dr. Tessa Lühmann

5. Prüfer: Prof. Dr.-Ing. Martin Bastian

Datum des öffentlichen Promotionskolloquiums

08.05.2018

Doktorurkunde ausgehändigt am

____

This work was conducted from February 2013 until August 2017 at the Department for Functional Materials in Medicine and Dentistry, University Hospital of Würzburg, Würzburg, Germany under supervision of Prof. Dr. rer. nat. Jürgen Groll.

„Da steh ich nun, ich armer Tor,
Und bin so klug als wie zuvor!“

Johann Wolfgang Goethe – Faust

LIST OF PUBLICATIONS

As first author:

1) **Gernot Hochleitner**, Julia F. Hümmer, Robert Luxenhofer, Jürgen Groll, *High definition fibrous poly (2-ethyl-2-oxazoline) scaffolds through melt electrospinning writing*, Polymer 2014, 55, 5017-5023

2) **Gernot Hochleitner**, Tomasz Jüngst, Toby D. Brown, Kathrin Hahn, Claus Moseke, Franz Jakob, Paul D. Dalton, Jürgen Groll, *Additive manufacturing of scaffolds with sub-micron filaments via melt electrospinning writing*, Biofabrication 2015, 7, 035002

3) Fei Chen*, **Gernot Hochleitner***, Tim Woodfield, Jürgen Groll, Paul D. Dalton, Brian G. Amsden, *Additive Manufacturing of a Photo-Cross-Linkable Polymer via Direct Melt Electrospinning Writing for Producing High Strength Structures*, Biomacromolecules 2016, 17, 208−214, *shared first authorship

4) **Gernot Hochleitner**, Almoatazbellah Youssef, Andrei Hrynevich, Jodie N. Haigh, Tomasz Jungst, Jürgen Groll, Paul D. Dalton, *Fibre pulsing during melt electrospinning writing*, BioNanoMat 2016, 17(3-4), 159–171

5) **Gernot Hochleitner**, Martina Kessler, Michael Schmitz, Aldo R. Boccaccini, Jörg Teßmar, Jürgen Groll, *Melt Electrospinning Writing of defined scaffolds using polylactide-poly(ethylene glycol) blends with 45S5 bioactive glass particles*, Materials Letters 2017, 205, 257–260

6) **Gernot Hochleitner***, Eva Fürsattel*, Reiner Giesa, Jürgen Groll, Hans-Werner Schmidt, Paul D. Dalton, *Melt Electrowriting of Thermoplastic Elastomers*, Macromolecular Rapid Communications 2018, 1800055, *shared first authorship

7) **Gernot Hochleitner***, Fei Chen*, Carina Blum, Paul D. Dalton, Brian G. Amsden, Jürgen Groll, *Melt electrowriting below the critical translation speed to fabricate crimped elastomer scaffolds with non-linear extension behaviour mimicking that of ligaments and tendons*, Acta Biomaterialia 2018, 72, 110-120, *shared first authorship

As co-author:

8) Felix Hanßke, Onur Bas, Cédryck Vaquette, **Gernot Hochleitner**, Jürgen Groll, Erhard Kemnitz, Dietmar W. Hutmacher, Hans G. Börner, *Via precise interface engineering towards bioinspired composites with improved 3D printing processability and mechanical properties*, Journal of Materials Chemistry B 2017, published online

9) Miguel D. Castilho, Dries Feyen, María Flandes-Iparraguirre, **Gernot Hochleitner**, Jürgen Groll, Pieter A. F. Doevendans, Tina Vermonden, Keita Ito, Joost P. G. Sluijter, Jos Malda, *Melt electrospinning writing of poly-hydroxymethylglycolide-co-ε-caprolactone-based scaffolds for cardiac tissue engineering*, Advanced Healthcare Materials 2017, 1700311

10) Miguel D. Castilho, **Gernot Hochleitner**, Wouter Wilson, Marc van Rijsbergen, Jürgen Groll, Jos Malda, Keita Ito, *Mechanical behavior of a soft hydrogel reinforced with three-dimensional printed microfibre scaffolds*, Scientific reports 2018, 8(1), 1245

11) Sarah Bertlein, Daichi Hikimoto, **Gernot Hochleitner**, Julia F. Hümmer, Tomasz Jungst, Michiya Matsusaki, Mitsuru Akashi, Jürgen Groll, *Development of Endothelial Cell Networks in 3D Tissues by Combination of Melt Electrospinning Writing with Cell-Accumulation Technology*, Small 2018, 14(2), 1701521

12) Mylène de Ruijter, Andrei Hrynevich, Jodie N. Haigh, **Gernot Hochleitner**, Miguel D. Castilho, Jürgen Groll, Jos Malda, Paul D. Dalton, *Out-of-Plane 3D-Printed Microfibers Improve the Shear Properties of Hydrogel Composites,* Small 2018, 14(8), 1702773

13) Andrei Hrynevich, Bilge Şen Elçi, Jodie N. Haigh, Rebecca McMaster, Almoatazbellah Youssef, Carina Blum, Torsten Blunk, **Gernot Hochleitner**, Jürgen Groll, Paul D. Dalton, *Dimension-Based Design of Melt Electrowritten Scaffolds,* Small 2018, 1800232

TABLE OF CONTENTS

LIST OF ABBREVIATIONS

AM	additive manufacturing
CAD	computer-aided design
CNC	computer numerical control
CTS	critical translation speed
CV	coefficient of variation
DIV	days *in vitro*
DSC	differential scanning calorimetry
EBM	electron beam melting
ECM	Extracellular matrix
EHD	electrohydrodynamic
ES	electrospinning
FDM	fused deposition modeling
GMP	good manufacturing practice
hMSC	human mesenchymal stem cell
HV	high voltage
LCST	lower critical solution temperature
MEW	melt electrospinning writing
MS	melt spinning
PCL	poly(ε-caprolactone)
PCLAC	poly(ε-caprolactone-*co*-acryloyl carbonate)
PLACLAC	poly(L-lactide-*co*-ε-caprolactone-*co*-acryloyl carbonate)
PED	precise extrusion deposition
PEO	polyethylenoxide
PEtOx	poly(2-ethyl-2-oxazoline)
PGA	polyglycolide

PID	proportional-integral-derivative
PLA	polylactide
POx	poly(2-oxazoline)
PP	polypropylene
PPO	polypropylenoxide
PS	polystyrene
PVC	polyvinylchloride
ROP	ring opening polymerisation
RT	room temperature
SD	standard deviation
SEC	size exclusion chromatography
SEM	scanning electron microscopy
SFM	scanning force microscopy
SOP	standard operation procedure
STL	stereo-lithography (file format)
TE	tissue engineering
THF	tetrahydrofuran
TOC	total organic content
UAM	ultrasonic additive manufacturing
UV	ultraviolet
XRD	x-ray diffraction

LIST OF SYMBOLS

a	fit parameter
b	fit parameters
Đ	polydispersity
dm/dt	mass flow
dm_1/dt	polymer mass flow through the spinneret
dm_2/dt	polymer mass flow of the jet
dm_3/dt	polymer mass flow of deposited fibres
$d\gamma/dt$	shear rate
E	Young’s modulus
E_A	activation energy
E_{el}	electrical field strength
F_{el}	electrical force
fØ	fibre diameter
h	spinning distance
$\hat{H}$	falling height
i	intensity
IØ	inner diameter
l	length of a pipe or spinneret
L	mesh width
m	mass
M/A	ratio median devided by average
m_1	polymer mass in spinneret and reservoir
m_2	polymer mass of *Taylor Cone* and jet
m_3	polymer mass of deposited fibres
M_n	number average molar mass

M_w	mass average molar mass
N	sample size
n_{pl}	power-law index for Rabinowitsch correction
p	pressure
p_c	capillary pressure
p_e	electrical pressure
q	charged particle
Q	single electrical charge
R	ideal gas constant
r	inner radius of a pipe or spinneret
r_{cry}	radius of a spherical crystal
r_{el}	distance between charges
r_{jet}	jet radius
r_s	mean surface curvature
R_a	average surface roughness
R_q	root mean square roughness
s_c	collector speed
T	temperature
t	time
$\tan\delta$	loss factor
T_g	glass transition temperature
T_m	melting point
T_{mo}	melting onset temperature
U	voltage
V	volume
$\widehat{V}$	belt collector speed

W_f	specific work of fracture
$\bar{y}$	sample mean
Y	value of the set
z	axial coordinate along the spinning distance
α	fit parameter
β	fit parameter
Δp	pressure gradient
ϵ	permittivity
ε	strain
ϵ_0	permittivity of vacuum
ε_u	ultimate tensile strain
η	viscosity
λ	rheological parameter
μ	surface tension
ρ_{el}	specific electrical conductivity
σ	stress
σ_{max}	maximum tensile strength
σ_u	ultimate tensile strength
τ	retardation time
φ	electrical potential

1 Introduction

Today, one of the greatest challenges in the field of biomaterials science and medicine still remains to regenerate damaged tissue.[1] While the clinical use of tissue transplantations is considered as gold standard, such therapies exhibit serious drawbacks. Examples are the necessary sacrifice of healthy tissue, high blood loss, morbidity and chronic pain for autologous tissue substitution or potential rejection, infections, disease transmission and fracture risk for allogeneic tissue substitution.[2-4] Furthermore, prevailing demographical changes concerning an increasingly aging population in our modern society demand for synthetic alternatives to replace or repair soft and hard tissue.[5]

Especially in the last two decades a rethinking emerged regarding such design strategies of suitable synthetic constructs.[6] Here, one of Hippokrates' insights "*The natural healing force within each of us is the greatest force in getting well.*" seems to be more valid than ever. Following this hypothesis, a tissue engineering (TE) scaffold should match the properties of the host tissue matrix in order to provide cells a suitable environment for migration, growing and fulfilment of their biological function. Therefore, scaffolds should mimic the very often highly oriented and complex fibrous morphology of the natural extracellular matrix (ECM), the natural habitat of the cells, on the nano- and micro level (Figure 1).

An established research strategy involves solution electrospinning (ES) of matrices with fibres that are only a few micro-meters or less in diameter.[7, 8] While those are highly appreciated due to their structural resemblance to the natural ECM, ES often requires toxic solvents and usually leads to randomised 2D non-woven meshes. Thus, common ES lacks of an opportunity to fine-tune the fibre position and orientation on the cell scale. In contrast to this, extrusion-based additive manufacturing (AM) methods can be used for highly customised 3D structures.[9] However, only fibres with usually hundred micro-meter in diameter or larger can be processed and hence, resulting scaffolds may not promote an optimal biomimetic environment for cells.

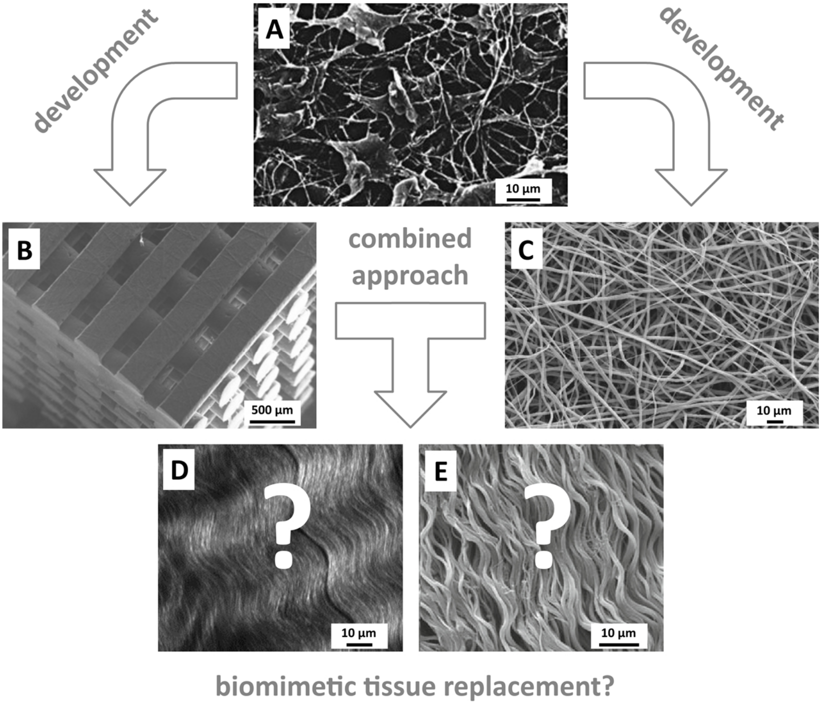

Figure 1: Development of synthetic scaffolds for TE. A) Keratocytes in the ECM as example for native 3D networks on cell level.[10] B) High definition synthetic construct with thick fibres printed with extrusion AM.[11] C) Random 2D non-woven mesh with thin fibres fabricated by ES.[12] Examples for highly organised and crimped collagen fibre structures in D) ligaments[13] and E) tendons[14]. By combining the approaches ES and AM, more biomimetic structures could be processed.
(A: Copyright © 2010 Karger Publishers, Basel, Switzerland, B: © IOP Publishing. Reproduced with permission. All rights reserved. C: Permission kindly provided by Taylor & Francis. D: With permission of SPIE and Dr. Kimani C. Toussaint E: Springer)

One promising way to overcome this limits, is to combine the specific benefits of AM and ES.[9] Printing of thin fibres to highly defined artificial ECMs would enable to fabricate more biomimetic structures and potentially helps to design improved implants for biomedical applications. Hence, the aim of the thesis was to advance and research a novel AM approach, termed melt electrospinning writing (MEW), within the context of biomaterial science. This covered pioneering opportunities of processing different synthetic biopolymers to highly defined and biomimetic microscale constructs for TE.

To introduce AM technologies, a general overview is provided in chapter 2: **State-of-the-art**. This section also introduces MEW as valuable tool for printing TE scaffolds made of aliphatic polyesters. The subsequent four chapters comprise the research work, starting with chapter 3: **Fibre pulsing**. Herein, poly(ε-caprolactone) and poly(2-ethyl-2-oxazoline) were used to address a commonly occurring process instability. A hypothesis explains its origin followed by an approach to characterise and overcome it. Based on this, a way to print submicron sized poly(ε-caprolactone) fibres to highly defined scaffolds is concerned in chapter 4: **Ultrafine fibres**. Further material scientific analysis was conducted as well as an utilisation approach for cell culture. Chapter 5: **Printing below CTS** includes a study of manufacturing non-linear structural features with poly(ε-caprolactone) and the resulting mechanical properties of scaffolds containing those architectural characteristics. Finally, chapter 6: **Photo-crosslinkable polymers** provides an approach to mimic the tensile behaviour of native ligaments or tendons based on poly(L-lactide-*co*-ε-caprolactone-*co*-acryloyl carbonate). Process engineering investigations, mechanical testing and cytocompatibility studies are presented.

2 State-of-the-art

Within chapter 2.1 on page 5ff, a universal review on AM technology is provided including recent economical, societal, technical and scientific aspects. Afterwards, the basics for MEW, polymer extrusion and electrohydrodynamic fibre processing, are introduced (chapter 2.2, page 18ff). Subsequently, challenges regarding TE scaffolds in chapter 2.3 on page 41ff and synthetic biopolymers in chapter 2.4 on page 46ff are discussed with respect to MEW.

2.1 Additive Manufacturing

2.1.1 A new technology picks up pace

Since its invention in the 1980's by Charles W. "Chuck" Hull[15-20], additive manufacturing (AM) has become a motor for innovation, be it for prototyping, tooling, manufacturing and repair of industrial components[21, 22], mainstream use[23] or the scientific progress itself (Figure 2). In the beginning barely used for something different than prototyping of models by the automotive industry[24], additive approaches emerged as versatile method to manufacture an abundance of products. These range from the nano-[25, 26] to macroscale objects made of organic polymers[27], metals[28], ceramics[29], composite materials[30] or biomaterials even including living cells[31].

Sometimes referred as "3D printing", AM approaches join materials via layer-by-layer processing to solid 3D objects using a computer model.[32] This re-thinking in fabrication strategy goes hand in hand with several advantages and disadvantages, influencing the existing manufacturing paradigm or even shifts in business models by its disruptive nature.[18, 33, 34] Nevertheless, AM will not replace the established mass production as a whole but rather fit in the landscape of industrial production and scientific lab use.

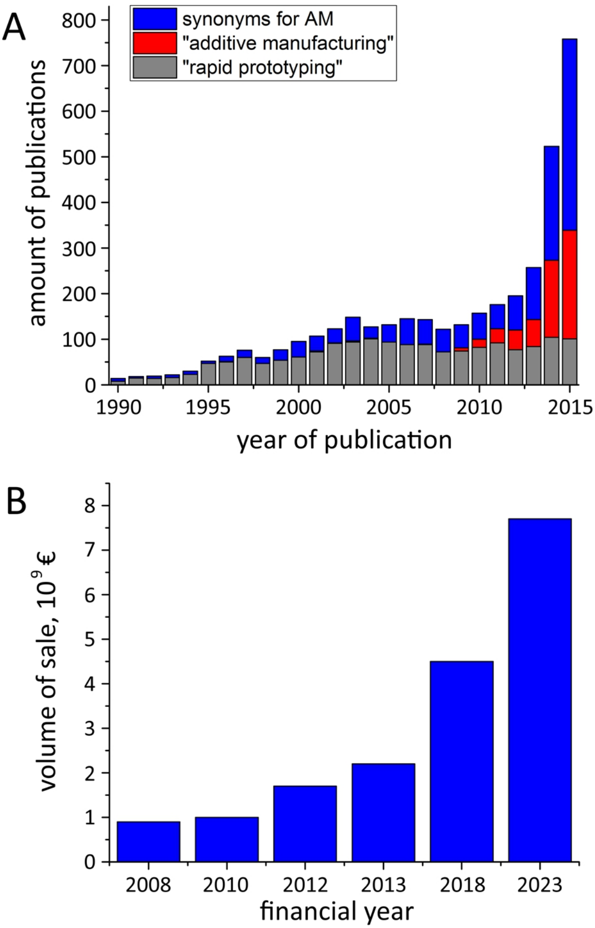

Figure 2: Impact of AM on economy and science. A) Amount of AM publications from 1990 to 2015. The number of "additive manufacturing", "rapid prototyping" and a combination of several synonyms for AM are provided. A substantial increase in scientific activity the last years can be observed. Keywords for synonyms used: "three-dimensional printing", "three dimensional printing", "3D printing", "additive fabrication", "additive process", "additive techn*", "additive layer manufacturing" "layer manufacturing", "freeform fabrication", "freeform manufacturing", "freeform process*", "layer process*", "layer fabrication", "rapid manufacturing". The symbols (*) are wildcards. B) Global economic expansion of the AM market based on official data and predictions*
(A: The search was conducted using title-words at "WEB OF SIENCE™", © Thomson Reuter, access 21.04.2016, B: data from https://de.statista.com, © Statista 2016, access 21.04.16)

Especially for large batch size manufacturing, established methods like casting, extrusion and injection moulding are the most economical choice (Figure 3). While expensive tools and the related development as starting investments are necessary, the unit costs are minimal. In contrast to this, AM shows increased unit costs but no additional tools or fixtures are required.[35] This simplicity attained by printing products directly from digital models makes AM a reasonable process to fabricate individual or customised products at small to medium scale batches with approximately 50 to 5000 units.[36]

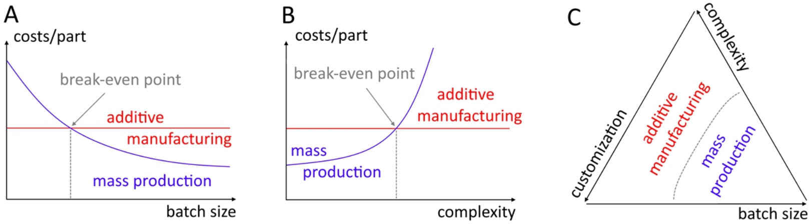

Figure 3: Comparison of mass production and AM concerning economical aspects. A) AM can be more economical than traditional mass production at low or medium batch sizes. B) With increasing product complexity or customisation, AM becomes economical. C) Three-axle illustration of economical regions of AM and mass production. Based on [37].

Additive approaches do not only offer unique and flexible design strategies without the need for assemblies[26, 27], but also development and changeover times are largely reduced if not even omitted. From this point of view, AM surpasses even workshop manufacturing and cutting-based machinery.[35] For example gradient or lightweight constructs with tailored infill structures like honeycomb designs[38], cooling channels[16] and electronical components to sense and react[39] can be integrated utilising AM.

Further, such approaches can help to launch new products more quickly and facilitate to bring them early to the market. Hence, customised high-end components with novel functionalities are already in use by the automotive, military and aerospace industry or for medical applications to name only a few examples.[16, 18, 33, 39]

However, the audience for additive processes is huge due to the variety of devices and capabilities available. Starting from device costs of 300 to 1,000 € with *fused deposition modeling* (FDM) for hobbyists[40] at low performance, high-tech AM equipment for processing of safety-related parts[39] like *selective laser sintering* (SLS) or *electron beam melting* (EBM) for medical implants[41] can cost 500,000 € with ease.[42] In between, several different techniques and devices are purchasable for everyday objects[37], fashion[43], furniture or art[44, 45], architectural modelling[46], education[39], surgery planning[47] and more (Figure 4), helping to introduce alternative ways for mass-customisation.

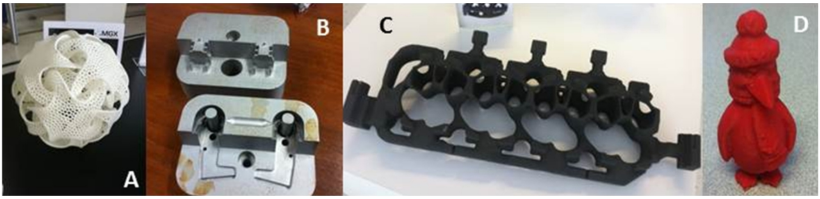

Figure 4: Example products processed by AM. A) Complex designed decoration made of nylon-11 via laser based powder bed fusion B) Rapid tooling of dies for injection moulding made of stainless steel via laser based powder bed fusion. C) Automotive cylinder head water jacket manufactured via binder jetting. D) Penguin mascot from Youngstown State University via desktop material extrusion printer.[37]
(© 2014, with permission from Elsevier)

In addition to the versatility, also environmental benefits emerge. In contrast to subtractive or formative processing, additive approaches could help to save natural resources or raw material and minimise process-related waste by avoiding cutting or shaping tools, coolants and further auxiliary resources.[33] Moreover, new printing-on-demand strategies help also to reduce the necessity of warehousing accompanied by lower overhead costs, less transport and packing which ultimately leads to saved fuel, energy and landfill.[33, 48-53]

Consequently, the whole supply chain ranging from raw material or component suppliers, equipment manufacturer, distributors and at least retailers could be altered[54, 55], some expect more “agile” supply chains.[33] Further, AM has the potential to change company structures or management thinking[56] and foster lean production as well as cloud manufacturing where several parties could share devices.[33, 39, 57] In such a way local printing-on-demand could also transform shop floors to desktop processing facilities and substantially change the occupational profile.

For this reasons not only social media (e.g. Economist, TheNewEconomy, Forbes, USA Today, CNBC, CNN) promoted AM or “3D printing” as a (third) industrial revolution[18, 35] with the potential to change the whole society. Following this vision, people could simply download models or design products by themselves and print them in decentralised shops around the corner, in malls or even at home with personal AM devices instead of ordering these from companies. This would obviously have tremendous legal and economic consequences in addition to changes in the public or societal view on goods and manufacturing.[33] Nevertheless, some of these methods are still in an early stage of development. While Rapid Prototyping has been used successfully for three decades, research areas like life science, tissue engineering and organ bioprinting are stuck in its infancy.[58-60]

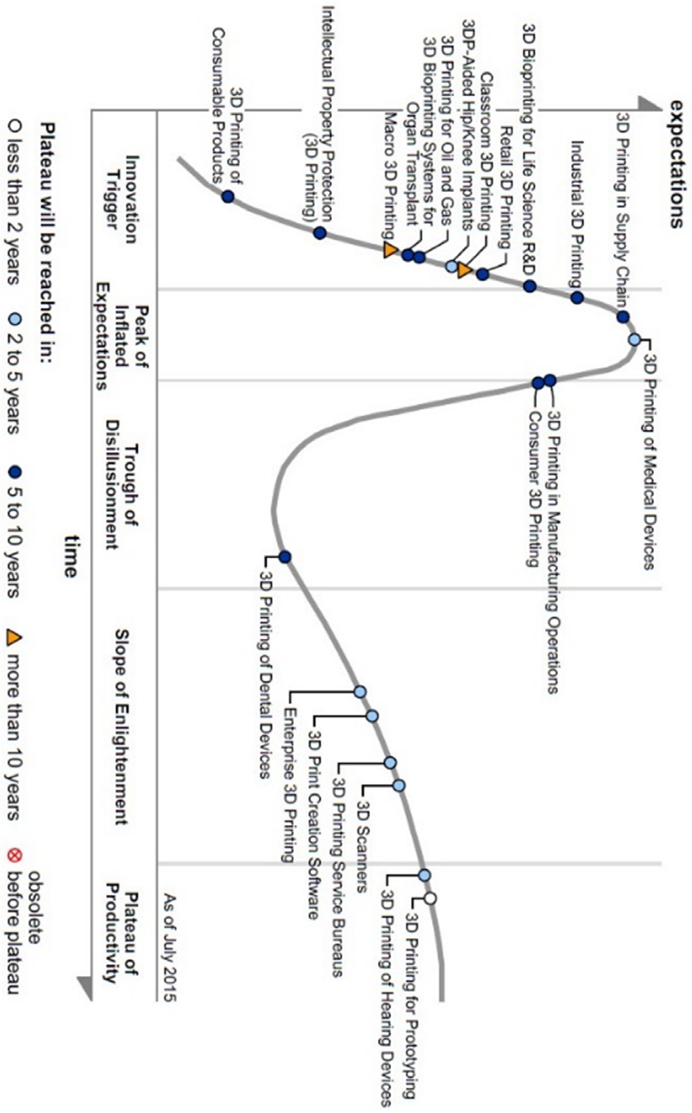

Figure 5: Gartner Hype Cycle for 3D printing 2015. Classification of different AM technologies according to the state-of-the-art.
(Permission kindly provided by Gartner, https://www.gartner.com, access 22.04.2016.)

The AM state-of-the-art and the related expectation by society can be expressed by the Gartner hype cycle (Figure 5). After the invention of the technology, the public expectations grow at first. Afterwards the limitations and disadvantages manifest followed up by time-consuming development and integration into the industrial world. Some innovations may fail along this progress. However, prototyping as the origin of AM reached the so-called “plateau of productivity” as it is already used in daily business by a large number of companies.

Even though, “industrial 3D printing” still lacks of several properties, since multiple challenges need to be overcome. The promise to print ready-to-sell products in one step is still not widespread reality. For example post-processing may be necessary to improve the surface finish or the overall component quality.[16, 37] Regarding this, also deposition accuracy in three dimensions must be increased to fulfil high industrial standards. Due to the layer-by-layer deposition mechanical properties, particularly in z-direction, can be suboptimal[24] or so-called stair-steps [39] may occur leading to a poor appearance quality. Additionally, the material range for AM is still small[27], although novel processes can lead to unique material compounds which cannot be joined using traditional technologies as welding or soldering.

Unlike mass production, AM throughput is low in general, nevertheless, the processing speed must be increased significantly for economical utilisation. Furthermore, large components in the meter-scale cannot be manufactured using the majority of AM techniques. Notably rapid tooling applications helping the established mass production could benefit from quickly processed moulds by AM for instance. Herein, high component quality and reproducibility is essential. In order to overcome related challenges, in-line control and measures must be implemented to react appropriately already during manufacture. Prior to this, advanced modelling or simulations (e.g. finite element method) of AM processes and component texture would help to deepen the understanding and push the recent limits of technology. Moreover, suitable education, training and user-friendly software solutions could improve AM's recent state-of-the-art. [16, 18, 24, 33, 39]

Table 1: Typical advantages and disadvantages of AM compared to those of traditional manufacturing. The listed statements are based on discussed data in this chapter and are generalised. Therefore, they may not fully apply to all single processes available.

	Advantages		**Disadvantages**
+	More complex and optimised components	-	Lack of training and education
+	Novel functional and integrated components	-	Lack of validation or certification methods
+	One-step processes without further assembly or material joining	-	Lack of proper technical solutions including software
+	Customisation and individualisation	-	Poor component properties
+	No tool-costs	-	Limited materials available
+	Faster product changes and reduced product-to-market time	-	Poor reproducibility
+	Reduced resource losses and waste	-	Limited component size
+	Optimised supply chain	-	Slow manufacturing
+	Printing-on-demand	-	High costs for large batch sizes
+	Printing at point of use		
+	New business models and cloud manufacturing		
+	Easy share of designs and models		
+	Decentralisation of fabrication processes and potential public emancipation		

Table 1 provides an overview of the advantages and disadvantages of AM opposed to traditional manufacturing methods as summary with respect to the information provided in this chapter.

All in all, AM shows an enormous development potential[27, 33], since it is still a young technology just picking up pace. However, forecasts about AM's impact in future is speculative. Nevertheless, one thing is certain: additive processing inspires a large public and helps the scientific progress inherently.

2.1.2 Technical aspects

AM fabrication follows always a methodical procedure, as reflected in Figure 6. At the beginning, a computer model as instruction file must be designed considering the limitations and nature of the desired component and the particular process going to be used (including material, dimensions, geometry, support structure, etc.). Therefore, a computer-aided design (CAD) is deployed which can also be created by utilising reverse-engineering via (optical) scanning of 3D objects.[61] As most prevalent software solution, a conversion of the CAD file to a so-called stereo-lithography (STL) format is conducted. Here, a transformation into a triangulated structure or coordinate triplets listing x, y, and z with an external closed surface takes place.[24] This is followed by a so-called slicing step, where the design is translated into a printable set of 2D layers suitable for bottom-up or layer-by-layer processing. Afterwards, the information is transferred to the AM device taking the final product dimensions, position and orientation into account.

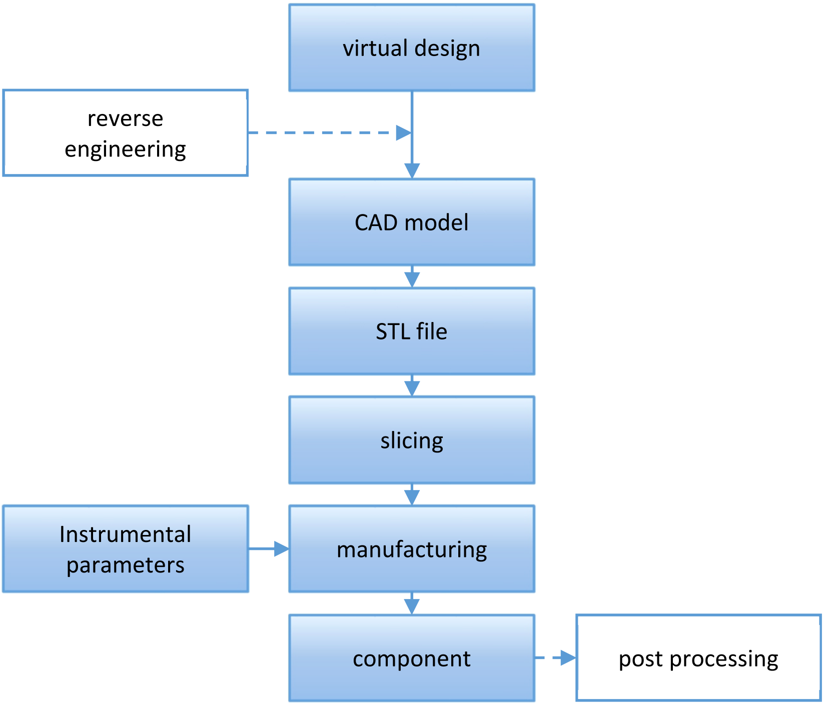

Figure 6: Schematic of AM procedure from a computer model to a product. Reverse engineering and post-processing can be optional steps. Based on [33, 35, 62, 63].

Meanwhile instrumental parameters (e.g. feed rate, energy input, temperature, collector velocity) controlling the deposition process of the material or precursor must be adjusted with respect to the final product and fabrication demands. Now, the physical manufacturing process is ready to be started. While the processing itself is mostly full-automated, an in-line monitoring can be implemented to react simultaneously on changes enabling a feedback-loop system for advanced control to prevent undesired errors. Due to the diversity of AM technology, the different processes are separately discussed in the following subchapters.

After deposition, the components must be removed – this is usually conducted by hand and thus, requires manpower. Here, necessary cooling rates etc. of the installation space, collector and product have to be taken into account to ensure quality standards and comply with safety aspects. Usually, a following post-processing step needs to be performed in order to improve product quality.

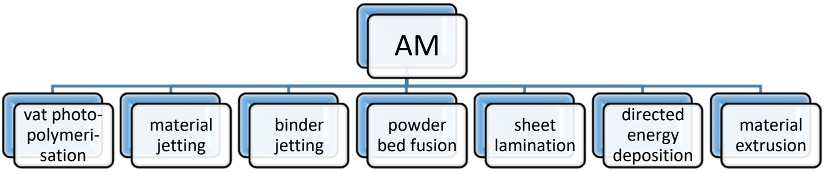

Figure 7: Classification of AM approaches according to ASTM "International Technical Committee F42 on additive manufacturing technologies".[64]

In the literature, several different classifications of AM methods can be found. For example classifications regarding the aggregate state of the material (precursor respectively) before deposition[17, 24, 27] or the printing head technology[65] have been chosen. Herein, the seven major classes according to the ASTM "International Technical Committee F42 on additive manufacturing technologies"[64], are presented and discussed since they provide a systematic view on the nature of the process without consideration of trademarked terms (Figure 7). In the next subchapter, material extrusion AM is introduced due to the relevance for the melt electrospinning writing process.

2.1.3 Material extrusion

AM via material extrusion utilises molten polymers, gels, pastes or liquid composites which are extruded by pressure, screws or rollers through a nozzle onto planar moving and stepwise declining platform or tray (Figure 8).[27, 66] Subsequently, the material solidifies by cooling, UV-irradiation curing or remains in shape due to rheological performance.[67] In order to print more complex components, supporting structures are necessary. These can be provided by multi-component print heads which are frequently included due to the simple setup. In contrast to other AM methods like vat polymerisation, material extrusion systems are capable of printing hollow structures to reduce manufacturing time and to save material or weight.

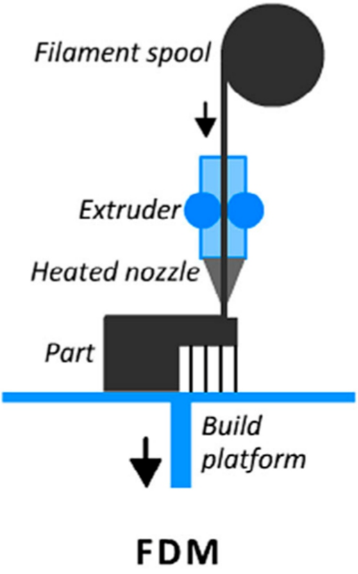

Figure 8: Schematic example for material extrusion by FDM.[61]
(Permission kindly provided by Taylor& Francis)

Due to the typical layer thicknesses of 0.2 to 0.5 mm[68], components can be processed quickly at the expense of the surface finish. For conventional use, FDM is one of the cheapest and most popular processes, even though the product quality may suffer from suboptimal fusion of deposited fibres and a low printing resolution.[68] Other examples for material extrusion are Precise Extrusion Deposition (PED)[66] or 3D Bioprinting [31].

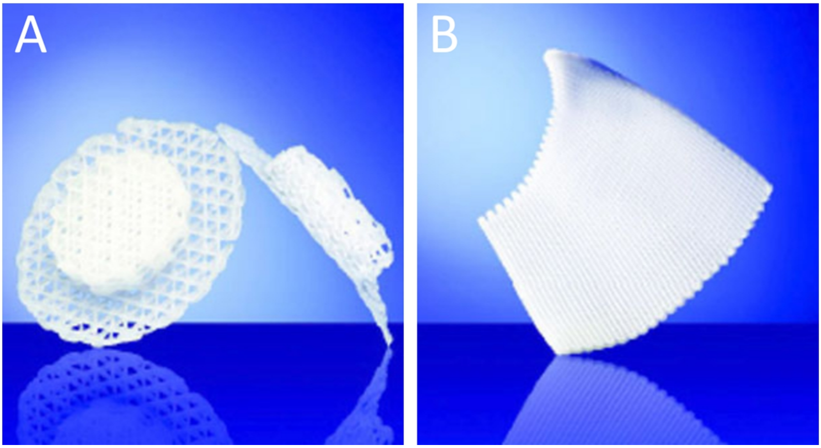

Figure 9: Medical implants printed by FDM. A) Osteoplug^{TM} for covering trephination burr holes in neurosurgery. B) Osteomesh^{TM} for craniofacial surgery to repair various types of fractures. Both products are made of synthetic biopolymer poly(ε-caprolactone) fibres and highly porous to foster cell ingrowth. The implants are biodegradable and can be replaced by healing tissue. (©2017 Osteopore^{TM}, description and permission for reprint kindly provided by Osteopore International Pte Ltd, https://osteopore.com/index.html)

However, FDM can even be used to manufacture highly porous and cell-invasive medical implants made of biodegradable micron-fibres[69], as reflected in Figure 9. Nevertheless, approaches to reduce the resulting fibre diameter are fundamental to extend the usability and to mimic the native extracellular matrix of human tissue. In this context, the extrusion of polymeric melts through small nozzles is further discussed in the subsequent chapter and bridges over to electrohydrodynamic fibre processing and melt electrospinning writing.

2.2 Novel strategies for printing fibrous micro constructs

2.2.1 The rheological limits of polymer extrusion

Usually AM polymer extrusion devices are limited to layer-thicknesses of 0.1 – 0.2 mm.[27] Nevertheless, the deposition of smaller fibres (≈ 50 µm) is feasible in principle[70], but also accompanied by a vast decrease of the throughput capability. An explanation for this can be given considering the rheological processing conditions. Importantly, deposited fibre diameters are largely defined by the inner diameter of the printing nozzle (or pipe) as it defines the outer shape. With respect to the Hagen-Poiseuille equation[71] the correlation of the volume flow rate through a pipe with circular profile can be expressed as:

$$\frac{dV}{dt} = \frac{\pi \cdot \Delta p \cdot r^4}{8 \cdot \eta \cdot l} \tag{1}$$

V = volume; t = time; Δp = pressure gradient; r = inner radius of the pipe;

l = length of the pipe; η = viscosity of the fluid

By spending attention to the dependency of the volume flow rate proportional to the nozzle's inner diameter to power of four, the substantial influence of the printing nozzle diameter can be explained. Indeed, the Hagen-Poiseuille equation is appropriate for viscous Newton fluids only, nevertheless can this formulation be a helpful guideline for viscoelastic polymer processing at the first glance. By taking the shear-thinning nature of polymers into account (β < 1), the extrusion process of the melt through the nozzle is usually expressed with following equation (adapted from [68, 72-75]):

$$\eta = \alpha \cdot \left(\frac{d\gamma}{dt}\right)^{\beta - 1} \tag{2}$$

α, β, = power-law fit parameters; dγ/dt = shear-rate; η = viscosity

Here, the non-isothermal setup conditions are not considered. In reality the cold polymer is fed into the printing nozzle and heated by convection starting at the interface between the melt towards its bulk, following a temperature gradient. Consequently, the viscosity equation can be split into a temperature-dependent Arrhenius term A(T) and the power-law function expressed with fit parameters, evaluated at the reference temperature T_0 (adapted from[68, 72, 76]):

$$\eta = A(T) \cdot \eta_{T_o} \cdot \left(\frac{d\gamma}{dt}\right) \; with \; A = e^{\frac{E_A}{R} \cdot \left(\frac{1}{T} - \frac{1}{T_O}\right)} \qquad (3)$$

E_A= activation energy; T = temperature; R = ideal gas constant; A(T) = 1 at T_0

To compensate the missing compliance of the simple power-law equation over the broad spectrum of different shear rates including asymptotic zero-shear conditions with viscosity η_0 according to $\lim_{\frac{d\gamma}{dt} \to 0} \eta = \eta_0$, the Carreau-Yasuda model can be applied and extended by the temperature function (adapted from [77, 78]) to:

$$\eta = \eta_\infty + (\eta_0 - \eta_\infty) \cdot \left[1 + \left[\lambda \cdot \left(\frac{d\gamma}{dt}\right)\right]^a\right]^{\frac{b-1}{a}} \cdot A(T) \qquad (4)$$

a, b = fit parameters dependent on polymer properties; λ = rheological parameter

Here, 1/λ describes a critical shear rate where η starts to decrease. The fit parameter a indicates the width between η_0 and the power-law region with the slope of b-1. For high shear rates, the viscosity turns into η_∞ with $\lim_{\frac{d\gamma}{dt} \to \infty} \eta = \eta_\infty$.

Potentially necessary yield stresses are neglected due to the missing relevance for the presented extrusion considerations. The viscosity behaviour of typical polymer melts at different shear rates is illustrated in Figure 10.

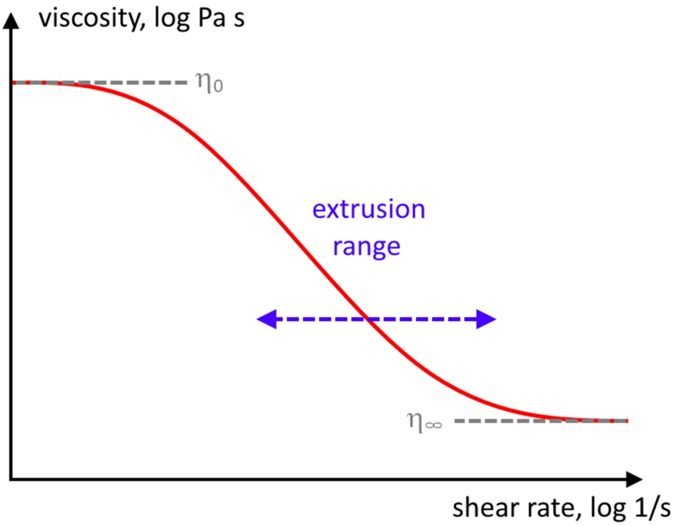

Figure 10: Schematic of the viscosity behaviour of polymers as a function of the shear rate. Most macromolecular melts show a distinct shear thinning behaviour. The resulting influence must be considered for extrusion AM approaches. Based on [79].

However, the lack of proper volume flow rates through small nozzles cannot be compensated by huge pressure gradients, even if such a shear-thinning polymer property can lead to a smaller viscosity at typical shear rates of $d\gamma/dt = 100 - 200\ s^{-1}$ [68] during extrusion AM. In order to understand the limitations of this, attention must be spend to the molecular scale. In their molten state, polymer chains exhibit a statistical orientation, or in other words the macromolecules are present in random coils.[80, 81] While pressed through a printing nozzle, such a melt is exposed to a certain mechanical stress resulting in shear and extensional flow and thus, a macromolecular deformation.[82] If this exceeds the counteracting diffusion relaxation, an alignment of the macromolecules results during the flow. The entropy of the melt decreases reversibly during alignment, a part of the mechanical force is stored by the elastic part due to the viscoelastic nature of polymers.[83] This behaviour can be expressed physically by the addition of Kelvin-Voigt with Maxwell elements, resulting in the so-called Burgers model or four parameter fluid:[84-86]

$$\varepsilon = \sigma_0 \cdot \left[\frac{1}{E_0} + \frac{1}{E_1} \cdot \left(1 - e^{-\frac{t}{\tau}}\right) + \frac{t}{\eta}\right] \qquad (5)$$

ε = strain; σ = stress; E_0, E_1 = Young's moduli; τ = retardation time

In the equation, three different parts act synergistically to describe polymer flow characteristics: an elastic, a viscous and a delayed elastic component as illustrated in Figure 11. While ideal viscous fluids undergo a deformation accompanied by energy dissipation when a certain mechanical stress is applied, the induced flow process stops immediately when the stress disappears. In contrast to this, ideal elastic solids undergo an immediate deformation process accompanied by energy storage when facing mechanical stresses. After disappearance of those, the elastic solid releases the stored energy completely by changing back to the initial state.[87] In case of polymeric materials, a combination of both characteristics can be observed influencing the extrusion and application performance conditions largely.

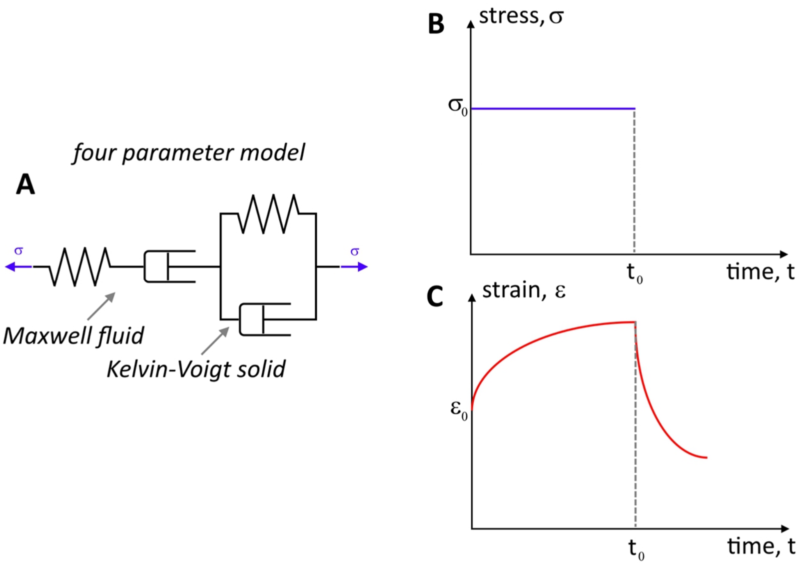

Figure 11: Schematic of the viscoelastic behaviour of polymer melts. A) The addition of Maxwell and Kelvin-Voigt elements yields in a four parameter fluid model. B) If a certain static mechanical stress is applied to a polymer melt, C) a deformation is induced that can relax partially afterwards. Based on [84].

When the polymer melt finally passes the nozzle and is no longer constrained, a relaxation process of the increasingly oriented macromolecules, termed die swelling, occurs driven by entropy and release of the elastically stored energy.[88, 89] This phenomenon can be caused by high feeding pressures (amongst other parameters) and leads to enlarged fibre diameters, as reflected in Figure 12. A further increase in extrusion rates by extreme feeding pressure gradients can cause melt fracture[90], an extrusion instability with plastically deformed polymer fibres as result, or damage the polymer melt on a molecular level. Similarly, a high temperature applied for a decreasing viscosity[68] can lead to thermal degradation and polymer chain scission.[91]

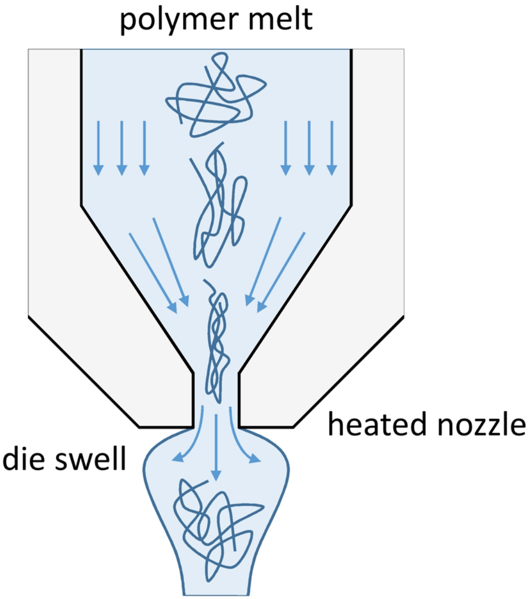

Figure 12: Schematic of die swelling during extrusion printing. The extruded polymer fibre exceeds the diameter of the printing nozzle due to molecular relaxation of polymer chains. Based on [68, 87].

While other measures as decrease of molecular weight, indeed leads to decreased melt viscosities as well, such polymers usually exhibit lower mechanical performance properties and are avoided as consequence.[92, 93] Thus, melt extrusion of polymers, for instance by PED or FDM, is eventually restricted regarding fibre diameters minimisation approaches.

2.2.2 Electrohydrodynamic fibre spinning

A proper way to overcome these boundaries of extrusion-based AM is the utilisation of an external electrical high voltage (HV) field. As already described 1600 by Gilbert William,[94] a water droplet can undergo a deformation and form a cone towards a rubbed amber moved close to it. This effect can be ascribed to an electrical or Coulomb interaction between charged materials and can be used for Electrospinning (ES) or electrohydrodynamic (EHD) processing of fibres with diameters ranging from micro- to nanometer scale.[95-99]

To generate such fibres technically, a polymer must be molten or solved and perfused by a pump, mechanical feeder or gas pressure through a spinneret towards an opposed collector. Here, an HV field must be applied between spinneret and collector as driving factor. Consequently, the charge carriers enter the surface of the liquid at the interface of the conductive spinneret and induce certain mechanical forces and thus, flow processes in the solution or melt by charge repulsion. This can be defined as stress or pressure p_e acting on the liquid surface:[100-102]

$$p_e = \frac{1}{2} \cdot \epsilon \cdot E_{el}^2 \qquad (6)$$

p_e = electrical pressure, ϵ = permittivity; E_{el} = electrical field strength

Hence, the pressure depends on the permittivity ϵ of the surrounding gas phase as well and the square of the electrical field strength E_{el}. In contrast, the capillary pressure p_c defined from the Laplace-Young equation is a function of the surface tension µ and the mean surface curvature r_s of the spinneret:[100-102]

$$p_c = 2 \cdot \frac{\mu}{r_s} \qquad (7)$$

p_c = capillary pressure, μ = surface tension; r_s = mean surface curvature

If the electrically induced pressure exceeds the capillary pressure ($p_e \geq p_c$), a so called *Taylor Cone* forms at the tip of the spinneret and a jet is accelerated towards the collector driven by electrical displacement forces and the acceleration in the HV field. As indicated by the name, this dependency was initially described by Taylor and defined as a critical acceleration voltage which must overcome the surface tension of a liquid (Figure 13):[103, 104]

$$U^2 = 4 \cdot \frac{h^2}{l^2} \cdot \left(ln \frac{2l}{r} - \frac{3}{2} \right) \cdot (0.117 \cdot \pi \cdot r \cdot \mu) \tag{8}$$

U = applied voltage in kV; h = spinning distance or distance between spinneret and collector; l = length of spinneret; r = inner radius of the spinneret

In the context of Coulomb interactions in the jet, the dependency of the electrical field $\vec{E}_{\mathrm{el}}$, the electrical potential φ and the electrical punctuate charge or charged particle q must be taken into considerations:[105, 106]

$$U_{12} = \varphi_1 - \varphi_2 = \int_{h_1}^{h_2} \vec{E}_{el}\, d\vec{h}\ with\ \vec{E}_{el} = \frac{\vec{F}_{el}}{q} = \frac{1}{4 \cdot \pi \cdot \epsilon_0} \cdot \frac{Q}{r_{el}^2} \tag{9}$$

U = applied voltage; ϕ = electrical potential; E = electrical field strength; h = spinning distance; ϵ_0 = permittivity of the vacuum; Q = single electrical charge; r_{el} = distance between charges

This dependency illustrates the resulting electrical force $\vec{F}_{el}$ as driving factor acting on the charged jet induced by the applied voltage U between spinneret and collector.

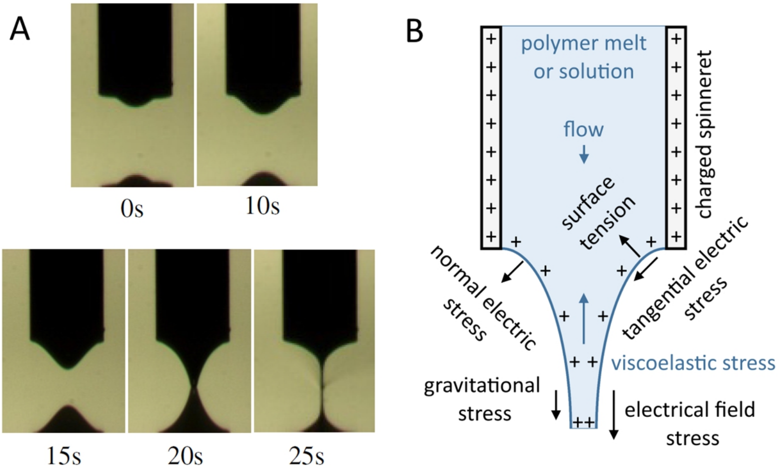

Figure 13: Formation of a Taylor Cone. A) The spherical shaped surface of the polymer melt becomes deformed conically by electrical interactions over time and finally ends in the formation of a jet and a polymeric fibre.[107] B) Several different stresses interact during EHD processing. Based on a modified version of Taylor-Mechler´s leaky dielectric model. [108, 109] (A: © IOP Publishing. Reproduced with permission. All rights reserved)

On the path to the collector, the jet undergoes a substantial reduction in diameter $2r_{Jet}$ and follows an asymptotic decay, described by a power-law function in case of poorly conductive Newton fluids:[110, 111]

$$r_{Jet} \sim z^{-\frac{1}{4}} \qquad (10)$$

r_{jet}= *jet radius; z = axial coordinate along the spinning distance*

This elucidates the tremendous stretching effect and hence, explains the small diameters of deposited fibres. By utilising solutions for ES, the jet follows a straight path at the beginning and usually undergoes a bending instability, termed whipping (Figure 14), afterwards. This chaotic motion is subject to Earnshaw's theorem of unstable systems exhibiting Coulomb interactions[112] between the charge carriers in the jet and is defined by a highly complex interaction between air friction, charge repulsion, viscoelastic material characteristics, solvent evaporation and more.[113, 114] During the thinning process of the jet, the charge density increases and overcomes the surface tension at a certain extend leading to whipping.[115] This phenomenon is believed as one of the most important for submicron fibre formation due to the vast increase in acceleration path[116, 117], but also leads to random fibre deposition or non-woven meshes.

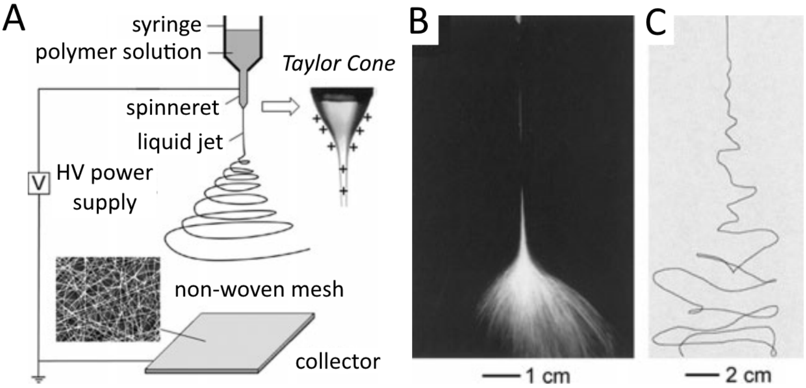

Figure 14: Common Solution ES.A) Schematic illustration of the experimental setup and the whipping instability of the jet. A non-woven mesh made of polyvinylpyrrolidone is presented.[95] B&C) Whipping instability of the jet during ES with an aqueous polyethylenoxide (PEO) solution. Capture time B) 1/250 s, C) 18 ns.[116]
(A: Copyright Wiley-VCH Verlag GmbH & Co. KGaA. Reproduced with permission, B&C: © 2001, with permission from Elsevier)

Several approaches are presented in literature trying to eliminate this random deposition structure. Among these are patterned collectors[118], fast rotating mandrels[119] and wire drums[120, 121], guidance of fibres between large collector gaps[122] or dynamic electrical fields[123] and lateral electrodes[124, 125]. However, none of these methods can be really considered as AM processes as they lack of a computer-controlled, accurately defined deposition setup.

In some other cases, the mechanical stress in the jet can be strong enough to overcome the entanglement of the macromolecules. This effect is termed Rayleigh instability and leads to droplet break-up driven by surface energy minimisation. While this is undesired for fibre spinning, it can nonetheless be utilised as electrospraying for manufacturing of micro- or nanometer sized beads. [126-128] However, such processing instabilities are undesired for AM fibre processing and not further discussed therefore.

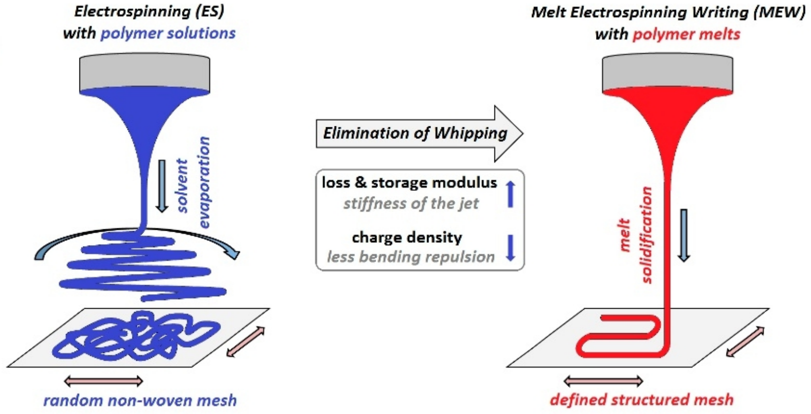

Figure 15: Illustration of solution versus melt ES. While whipping instabilities during solution ES are common, the utilisation of polymeric melts can lead to a linear jet path from the spinneret to the collector.[129]
(Published under Creative Commons licence CC BY 3.0)

In order to overcome whipping and Rayleigh instabilities, the utilisation of a polymer melt instead of a polymer solution can be beneficial. On one hand the use of often toxic solvents and their residues in the deposited fibres can be avoided and a technical challenging exhaust is not required.[130] On the other hand, melt ES necessitates thermoplastic polymers with a proper thermal degradation stability limiting the spectrum of suitable materials, while solution ES relies on solubility of polymers and the dielectric properties of resulting solutions.[131]

Comparing both, melt and solvent jets physically, the main differences can be found in the solidification process by cooling of melts (Figure 15). In addition, they exhibit increased viscosities[132] or resistances against the bending forces and lowered charge densities, as the formation and transport of ions is influenced by electrical conductivity determining the jet's break-up into droplets.[9, 102, 133] Thus, melt ES can throughout enable a straight jet path and serves as basis for a direct writing or AM approach.[1]

2.2.3 Melt Electrospinning Writing

In order to use EHD printing of polymer melts for so-called melt electrospinning writing (MEW) approach, a suitable experimental setup including a computer-controlled collector is required. While rotational and translational movements of cylindrical collectors are indeed utilisable, this work focuses on planar collectors moving in horizontal directions comparable to common extrusion AM devices (Figure 16). Here, it is important to note the outstanding decrease of fibre diameters compared to FDM or PED. While one of the thinnest fibre diameters for MEW using poly(ε-caprolactone) (PCL) reported by Wei et al. is about 5 µm [107], AM extruded fibres are at least one order of magnitude thicker and thus, exhibit a hundred times increased cross-sectional area or even more.

---

[1] Direct writing of polymer solutions is indeed feasible even if more inconvenient for processing of 3D constructs. Research has been conducted referred as near field electrospinning (NFES)[134], EHD jet printing[135] or direct write ES[125]. These methods are out of the scope and not further discussed in this work.

However, the fibre and construct dimensions are largely determined by the experimental setups in case of both, MEW or extrusion AM. For melt ES, a broad variation of such setups and different polymers, interesting for MEW applications, with different advantages and disadvantages have been used already. These are listed in a very comprehensive and descriptive review "*Melt electrospinning today: An opportune time for an emerging polymer process*" written by Brown et al.[102], and are not further discussed consequently.

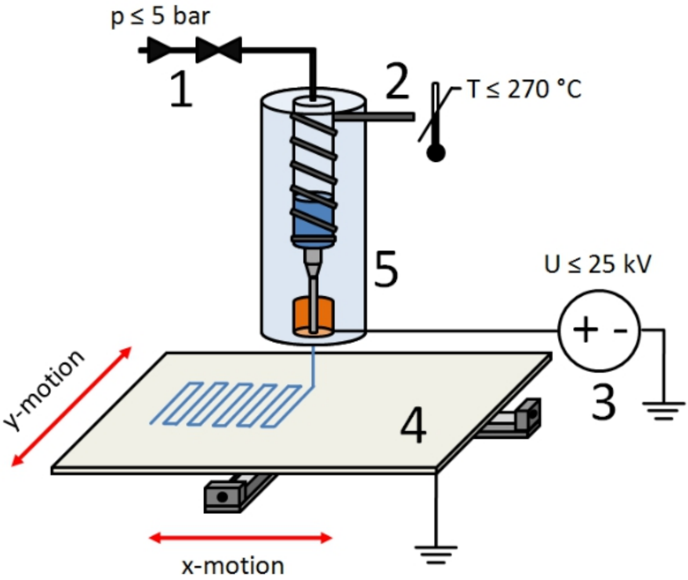

Figure 16: Schematic drawing of a typical state-of-the-art MEW device. 1) N_2 gas or pneumatic pressure assisted feeding system, sometimes replaced by a syringe pump 2) Electrical heater 3) HV source 4) computer-controlled collector plate translating by two orthogonal positioned ball-screw axes 5) Print head with implemented syringe including polymer melt as reservoir and a prepared needle tip as spinneret connected to a HV electrode.[136]
(Published under Creative Commons licence CC BY-NC-ND 3.0)

In order to directly write and linearly deposit fibres onto the collector surface, the collector speed s_c must match the final speed of the jet s_j when reaching the collector surface. This matching speed, with the boundary condition $s_c = s_j = CTS$, is termed critical translation speed (CTS)[137] and plays a key role in controlled fibre placement during MEW (Figure 17).

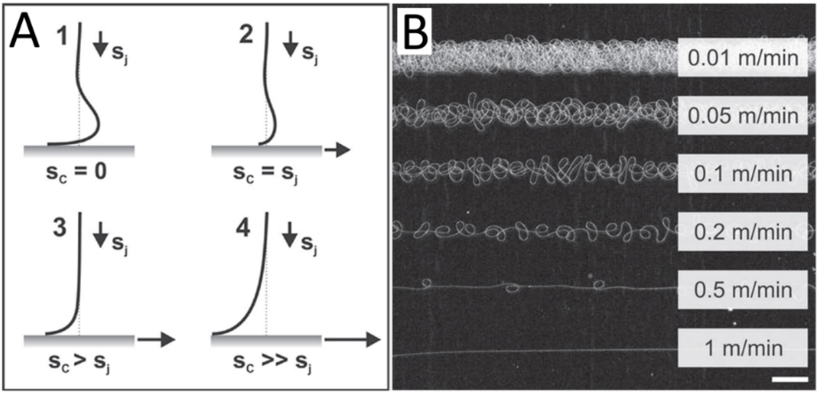

Figure 17: the influence of jet and collector speed during MEW.A) Illustration of the jet geometry reaching the collector surface. B) Deposited PCL fibre morphology with different collector speeds; 0.5 mmin^{-1} < CTS ≤ 1 mmin^{-1}.[137]
(Permission kindly provided by Wiley)

While printing at $s_c < CTS$ leads to a non-linear deposited fibre by buckling, $s_c > CTS$ further thins the diameter of the jet due to mechanical stretching.[107, 137]

2.2.3.1 Instrumental parameters

The described adjustment of the collector speeds is just one option to influence the fibre diameter, the main instrumental and material parameters: melt temperature, spinneret diameter, melt flow rate, polymer properties and the electrical field strength must be considered as well.

2.2.3.1.1 Melt temperature

Believed as one of the main factors for influencing fibre diameter in melt ES, a high temperature results in a low viscosity of the molten polymer, in particular slightly above the melting point.[138, 139] Nevertheless, this influence decreases at high temperatures far above the melting point since viscosity changes get more and more insignificant.[130] Considering the viscoelastic nature of polymer melts, high temperatures result in a high loss factor tan δ, the viscous part becomes more prevalent in contrast to the elastic part.[140] In addition to the decreased viscosity, an overall lowered resistance against the stretching process, driven by the HV field, can be observed. Hence, a high jet CTS results that influences the fibre diameter and necessitates to increase the collector speed s_c in order to enable direct writing.[137] Due to a potential adverse influence on the macromolecules, the temperature should be limited when processing thermal sensitive polymers. Aliphatic polyesters for instance, as most important polymer class for MEW, can degrade significantly in minutes or hours at relevant processing temperatures in the melt reservoir.[141-143]

2.2.3.1.2 Spinneret diameter

The spinneret diameter limits the melt flow rate substantially, in accordance with the boundaries of polymer rheology and extrusion limitations (as discussed, see page 18ff). Here, small sized spinnerets lead to small diameter fibres[107], albeit accompanied by decreased manufacturing throughput. Typical spinneret sizes range from 50 µm[107] to 500 µm[144] with resulting fibre diameters of 5 µm[107] to 50 µm, respectively[137, 144].

2.2.3.1.3 Melt flow rate

Another way to influence the fibre diameter is the adjustment of the melt flow rate by the feeding pressure or the accelerated polymer perfusion. As a result of high melt feed, large fibre diameters can be achieved. Common feeds are within several microliters per hour, Brown et al. has shown manufacturing of 10 µm to 30 µm PCL fibres using a melt flow of 5 μlh^{-1} to 50 μlh^{-1}.[137] Since the pressure limitations are not as restricted as the utilisation of temperature or voltage, the feed melt flow rate is an efficient way of controlling the fibre diameter. Nevertheless, instabilities can be observed at high pressures as well (partially provided on page 18ff). This phenomenon may strongly depend on the polymer properties like functional groups, molecular weight, molecular branching etc. and is barely understood so far.

2.2.3.1.4 Polymer properties

Since the molecular weight and the corresponding molecular distribution (polydispersity) determine the rheology largely, the length, configuration and constitution of the macromolecules are key factors to control fibre diameter, CTS of the jet, throughput and the construct properties itself. As already discussed for extrusion AM, a low molecular weight results in low viscosities and improved viscous deformability during EHD acceleration due to decreased polymer chain entanglement in the jet. Moreover, Lyons et al. observed that even a relatively strong HV field (1.5 $kVmm^{-1}$) is not capable of forming a *Taylor Cone* at all using polypropylene (PP) with a relatively high molecular weight (M_w = 580 $gmol^{-1}$ and M_n = 166 $kgmol^{-1}$).[99] If forming a stable jet, the linear increase in molecular weight of PP can lead to an exponential increasing fibre diameter. In particular proven by Lyons et al. at 1 $kVmm^{-1}$, atactic PP with M_w = 14 $kgmol^{-1}$ resulted in 28 µm and M_w = 19.6 $kgmol^{-1}$ in 53 µm fibre diameters. Accordingly, isotactic PP with M_w = 106 $kgmol^{-1}$ led to 41 µm and M_w = 190 $kgmol^{-1}$ to 130 µm fibre diameters. The corresponding tacticity also influences the resulting fibre diameter since atactic PP exhibits a random methyl-group orientation inhibiting crystallisation due to steric hindrance. On the contrary, isotactic PP can crystallise leading to molecular alignment and fibre shrinkage during solidification and thus, reduced fibre diameters.[99, 145]

2.2.3.1.5 Electrical field strength

As already shown in the chapter **Electrohydrodynamic fibre spinning** on page 23ff, the acceleration voltage is the driving force for EHD fibre manufacturing. Hence, an increasing field strength results in an increased stretching force and finally in thin and fast jets. [130] If this phenomenon manifests essentially during MEW remains a question of applied instrument parameters and the setup since also no significant influence of voltage with short spinning gaps on fibre diameters are reported in literate as well.[107] Nevertheless, it is believed that increased voltages per defined spinning distance or field strengths also lead to increased mass pull into the jet.[99, 138, 146] As shown earlier, molten polymers can require strong HV fields in order to form *Taylor Cones*[99]. With respect to this insight, it is important to understand that a certain field strength value (≈ 3 $kVmm^{-1}$ in air[147]) results in arcing along the spinning distance limiting the adjustable field strength range for technical use. In contrast to FDM where nozzle and collector are about only the extruded fibre diameter apart, MEW usually works at larger spinning gaps ranging from 170 µm[107] to 3 cm[137].

While a decreasing distance between spinneret and collector increases the electrical field analogously to an increasing voltage, further effects influencing the cooling behaviour of the jet need to be considered.

2.2.3.2 Solidification of the melt jet

During the acceleration from the *Taylor Cone* towards the collector surface, the molten jet undergoes quenching and a partial or full solidification process. While such small melt ES jets exhibit high specific surfaces anyway, further cooling due to EHD quenching can lead to substantially faster solidification (Figure 18). Since natural convection, with small Reynold numbers ≈ 1 or less at the *Taylor Cone*, and forced convection along high speed jets may dominate the heat transfer classically[148], an ionisation and acceleration of air molecules in the HV field takes place. This may be the result of a continuous corona discharge[149], especially when strong HV fields below to the electrical air gap breakdown limit (< 3 $kVmm^{-1}$) and above the corona onset, based on Peek's law[150], are utilised.

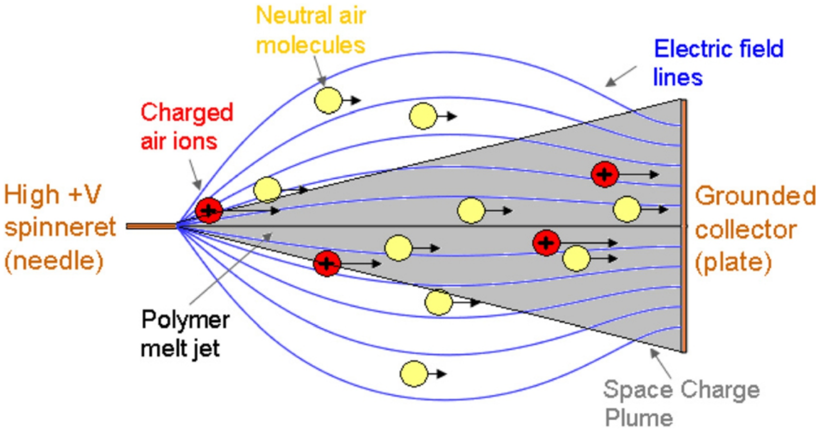

Figure 18: Illustration of EHD quenching. During EHD driven manufacturing via HV fields, gas molecules are ionised and accelerated towards the collector.[148]
(Reprint with the permission of AIP Publishing)

At the HV spinneret tip (ionisation zone) electrical charges can enter the surrounding gas phase, leading to ionisation and a field-driven acceleration of ions towards the collector (drifting zone) along the jet. On this path, ions collide with neutral air molecules and exchange physical momentum thereby. Hence, about 10-fold increased quenching rate for melt jets during melt ES have been observed.[148, 151-154] Additionally, the humidity of the surrounding air must be considered since it can further cool the melt jet. According to the literature, rates of 20 % changes in convection heat transfer are suggested[155, 156], necessitating an adjustment of the instrumental parameters for stable MEW processing. It seems to be obvious that this may also interfere with EHD quenching somehow, although no substantial investigation referring to this is published for MEW so far.

By spending attention to the highly anisotropic macromolecular flow processes, as in case of MEW, influences on the solidification process can be observed [157-159] according to Ziabicki's model of so called flow induced crystallisation.[160-162] Due to the very short in-flight residence time of the jet, common thermally induced processes can be neglected considering the crystallisation of polymer melts during MEW. Basically, the given influences on nucleation and crystallisation kinetics due to the (virtually uniaxial) aligned macromolecules alter the transition from liquid to solid phase into the polymer leading to a changed crystal morphology that also may influence the performance properties (mechanical behaviour etc.) of resulting fibrous constructs. For melt ES processing, Zhmayev et al. have refined and confirmed a novel model based on flow induced crystallisation, providing a profound insight into the solidification of semi-crystalline polymers using the example of polyamide (Nylon-6,6).[160]

In order to control the deposition and fusion behaviour of fibres during MEW, understanding the solidification process is elementary. Two requirements must be fulfilled to generate coherent and dimensionally stable constructs: First of all, deposited fibres need to withstand a suspension over relatively large gaps up to 1 mm[137], and second, a proper fusion between fibre-layers must be ensured. Thus, the optimum between completed crystallisation and the molten state must be found, mainly by optimising the spinning gap while taking other parameters like voltage and temperature into account.

2.2.3.3 Charge transport in fibres

Another consequence of the applied voltage and crystallisation can be observed by spending attention to the fibre`s residual charge. While conductive collectors are used to facilitate an electrical circuit from HV source or electrode to the earthed surface, the processed solid polymers are mainly dielectric materials.[102] Those exhibit a high ohmic resistance, with about ≥ 10^{-10} $\Omega^{-1}m^{-1}$ due to the filled valence band with its large gap > 2 eV to the empty conduction band[163], and are known for the ability to store electrical charge over long periods of time.[164]

While mechanisms involved in charge storage remain in discussion, several publications focusing on charge transport, charge location into polymers and charge dissipation help understanding the electro-physical processes during MEW. The polarity of functional groups in the polymer can provide a certain charge storage capacity and act as traps, depending on the electronegativity of involved (hetero)atoms and the molecular architecture of aromatic[165] molecules or carbonylic[166] functions for instance. The morphology of the polymers play an important role as well, it is believed that charges can accumulate at interfaces between the amorphous and crystalline phases[102] or at the centre of spherulites[167] of semi-crystalline polymers. Additionally to the three classified volume traps: 1) atomic sites, 2) functional groups and 3) differently crystalline regions, other factors like defects, impurities, additives, absorbed or degraded molecules and more may influence the charge behaviour significantly. Focusing on MEW performance, the charge transport or dissipation into the jets and fibres are important. Such processes depend on present activation barriers and molecule mobility or diffusion.[102] The extreme complexity due to the influence of temperature gradients, stretching and solidification processes and more effects during MEW makes it impossible to predict the charge behaviour of deposited fibres quantitatively and remains a question of trial and error.

Nevertheless, the discussed electric polymer characteristics can highly influence the construct structure since residual charges in or onto the fibres may not be fully dissipated during layer-by-layer fabrication. Already deposited and charged polymer fibres can repulse the impinging jet and lead to defects with increasing construct height. MEW experiments have shown a limit of PCL construct heights without significant structural imperfections ranging from 100 µm to 1 mm for instance.[137, 168]

2.2.3.4 Summarising thought on MEW

Albeit MEW is in a very early stage of development and lacks of high throughput, applicable materials and geometrical resolution so far, it is nonetheless a fascinating and promising method with unique advantages such as the combination of AM control and micron fibre size.

While less than 0.5 % of the summarised ES literature comprises the utilisation of melts[9] with not more than 150 publications[130] until 2016, only ≈ 24 of them focus on AM of molten polymers or scientific approaches based on corresponding constructs. A list consisting of these publications can be found in Table 2.

Table 2: Overview of primary research articles involving MEW as process. Review articles and book chapters are excluded. This table does not claim to be exhaustive.

Year	First author, *title*, journal
2008	Dalton et al., *Patterned melt electrospun substrates for tissue engineering*, Biomedical materials
2011	Brown et al., *Direct Writing By Way of Melt Electrospinning*, Advanced materials
2012	Dalton et al, *Melt electrospinning writing fibrous scaffolds for regenerative medicine*, Journal of Tissue Engineering and Regenerative Medicine
	Brown et al., *Melt electrospinning in a direct writing mode*, Journal of Tissue Engineering and Regenerative Medicine
	Brown et al., *Design and Fabrication of Tubular Scaffolds via Direct Writing in a Melt Electrospinning Mode*, Biointerphases
2013	Wei et al., *Direct fabrication of high-resolution three-dimensional polymeric scaffolds using electrohydrodynamic hot jet plotting*, Journal of Micromechanics and Microengineering
	Farrugia et al., *Dermal fibroblast infiltration of poly(ε-caprolactone) scaffolds fabricated by melt electrospinning in a direct writing mode*, Biofabrication
	Mota et al., *Melt electrospinning writing of three-dimensional star poly(ε-caprolactone) scaffolds*, Polymer International
2014	Powell et al., *Characterization of the Microarchitecture of Direct Writing Melt Electrospun Tissue Engineering Scaffolds Using Diffusion Tensor and Computed Tomography Microimaging*, 3D Printing and Additive Manufacturing
	Hochleitner et al., *High definition fibrous poly(2-ethyl-2-oxazoline) scaffolds through melt electrospinning writing*, Polymer
	Brown et al., *Melt electrospinning of poly(ε-caprolactone) scaffolds: Phenomenological observations associated with collection and direct writing*, Materials Science and Engineering C
2015	Ristovski et al., *Improved fabrication of melt electrospun tissue engineering scaffolds using direct writing and advanced electric field control*, Biointerphases
	Visser et al., *Reinforcement of hydrogels using three-dimensionally printed microfibers*, Nature Communications

Year	First author, ***title***, **journal**
2015	Ko et al., *Mathematical model for predicting topographical properties of poly(ε-caprolactone) melt electrospun scaffolds including the effects of temperature and linear transitional speed*, Journal of Micromechanics and Microengineering Hochleitner et al., *Additive manufacturing of scaffolds with sub-micron filaments via melt electrospinning writing*, Biofabrication Jungst et al., *Melt electrospinning onto cylinders: effects of rotational velocity and collector diameter on morphology of tubular structures*, Polymer International Bas et al., *Enhancing structural integrity of hydrogels by using highly organised melt electrospun fibre constructs*, European Polymer Journal
2016	Chen & Hochleitner et al., *Additive Manufacturing of a Photo-Cross-Linkable Polymer via Direct Melt Electrospinning Writing for Producing High Strength Structures*, Biomacromolecules Haigh et al., *Hierarchically Structured Porous Poly(2-oxazoline) Hydrogels*, Macromolecular Rapid Communications Hochleitner et al., *Fibre pulsing during Melt Electrospinning Writing*, Bionanomaterials Tourlomousis et al., *Towards Resolution Enhancement and Process Repeatability With a Melt Electrospinning Writing Process: Design and Protocol Considerations*, American Society of Mechanical Engineers Liao et al., *Effect of humidity on melt electrospun polycaprolactone scaffolds*, Bionanomaterials He et al., *Development of melt electrohydrodynamic 3D printing for complex microscale poly (ε-caprolactone) scaffolds*, Biofabrication

As a large part of the listed title indicates, Tissue Engineering is currently the most important research field for MEW-derived constructs or so-called scaffolds. There are several reasons for this, some examples are the cost-efficient setup for lab use, poly(ε-caprolactone) as established polymer for biomedical use and the opportunity to fabricate scaffolds with promising morphological conditions.

2.3 Scaffold based Tissue Engineering

While Tissue Engineering (TE) aims for restoring, maintaining or improving the function of defective tissue and organs in order to retain life's quality, many attempts rely on the use of scaffolds.[169-171] Here, the strategy purposes a highly combinatorial approach including disciplines like cell biology, chemistry, material and engineering science in order to understand cell-material interaction and to establish new medical therapies ultimately.

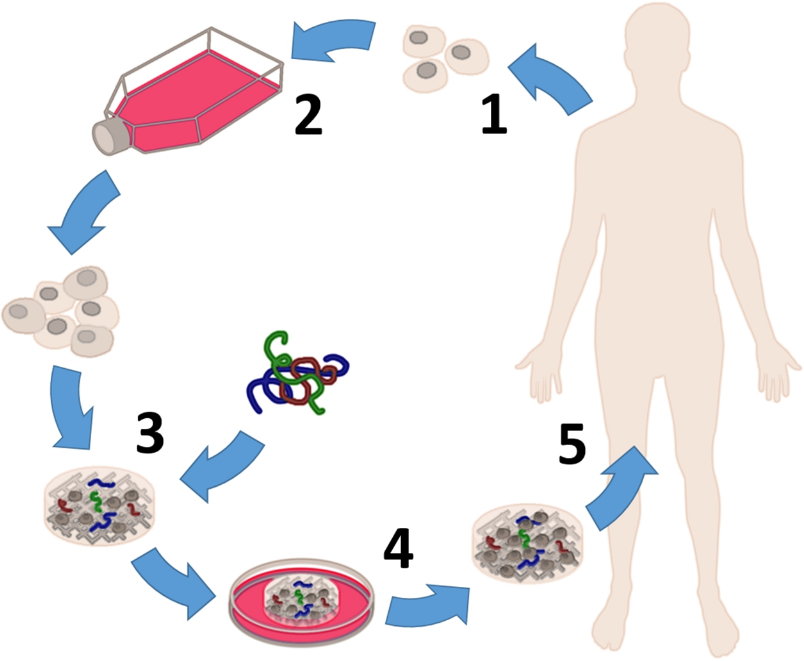

Figure 19: Illustration of the scaffold based TE principle. 1) Extraction of human cells 2) Culture of cells in vitro 3) Seeding cells onto or into a scaffold, optionally with addition of bio-functional molecules like growth factors etc. 4) Growing of a suitable TE construct and 5) Implantation into the host as medical therapy. Based on [172, 173].

As illustrated in Figure 19, the essential procedure consists of a human cell extraction, the cultivation of those in conjunction with a scaffold as supportive structure and an implantation back into the defective site of the host body. Thereby, damaged tissue without sufficient self-healing capacity is replaced. The TE construct is rebuilt or degraded afterwards and becomes substituted by mature and healthy tissue from the host again in the ideal case.

While there is no general law how to design a perfect scaffold, some basic requirements must be provided regardless of the tissue type to induce a proper biological response and to avoid adverse cell and tissue reactions.[174-176]

2.3.1 Biocompatibility

The used biomaterial needs to enable cell adhesion and viable cell functions such as proliferation or differentiation of stromal cells. Thus, the surface chemistry is an important factor as this may control protein absorption and determine the cell-material interaction and cell fate widely. Here, the material must be designed to assure a minimal immune or foreign body reaction.[177, 178]

2.3.2 Degradability

In many cases, scaffolds for TE are designed to undergo degradation during the healing process of the host, mainly by hydrolysis of ester groups or in an enzymatic way when contacting body fluid. Neither material, nor intermediates or end products may act here in a cytotoxic, carcinogenic or thrombogenic way.[179] With respect to this, the degradation rate and absorption kinetics must be tailored to assure optimal biomechanical conditions and tissue development. Healthy cells can start to express structural proteins gradually with the aim to model a new extracellular matrix substituting the scaffold functions by time. Here, an accelerated scaffold degradation could lead to tissue collapse and cell apoptosis or necrosis in the worst case.[180, 181]

2.3.3 Mechanical properties

During tissue formation, proper mechanical characteristics of the scaffolds can be very important. At least at the beginning, the material must withstand a certain stress and strain or may exhibit a sufficient young's modulus and toughness depending on the type or load of the host tissue. An oversized implant stiffness for instance can lead to so called stress shielding and tissue degeneration of cell types requiring mechanostimuli. Moreover, specific cell types require defined mechanical properties or mechanoinduction for viable tissue function or desired differentiation behaviour.[182-184]

2.3.4 Scaffold architecture

In case of 3D scaffolds, cells should be able to infiltrate and migrate into the structure. Thus, a sufficient supply with oxygen and nutrients as well as removal of metabolites must be ensured. Accordingly, blood vessels must be present in a range of 100 to 200 µm[185, 186] of surrounding cells to enable a proper mass transport. For the desired integration, growth and remodelling of the tissue, a highly porous and interconnecting design enabling sufficient vascularisation or angiogenesis must be applied. Moreover, it is believed that rough and porous structures can help for healing in a less fibrotic way, means the typical encapsulation reaction of the host body to foreign material is attenuated.[187-191] Beside this, the scaffold dimensions need to be adjusted to the defect size and shape of the patient too, necessitating proper manufacturing techniques to fulfil the presented criteria.[6, 192, 193] Therefore, MEW can be considered as promising method to fabricate tailored structures that match defect size and microarchitecture.

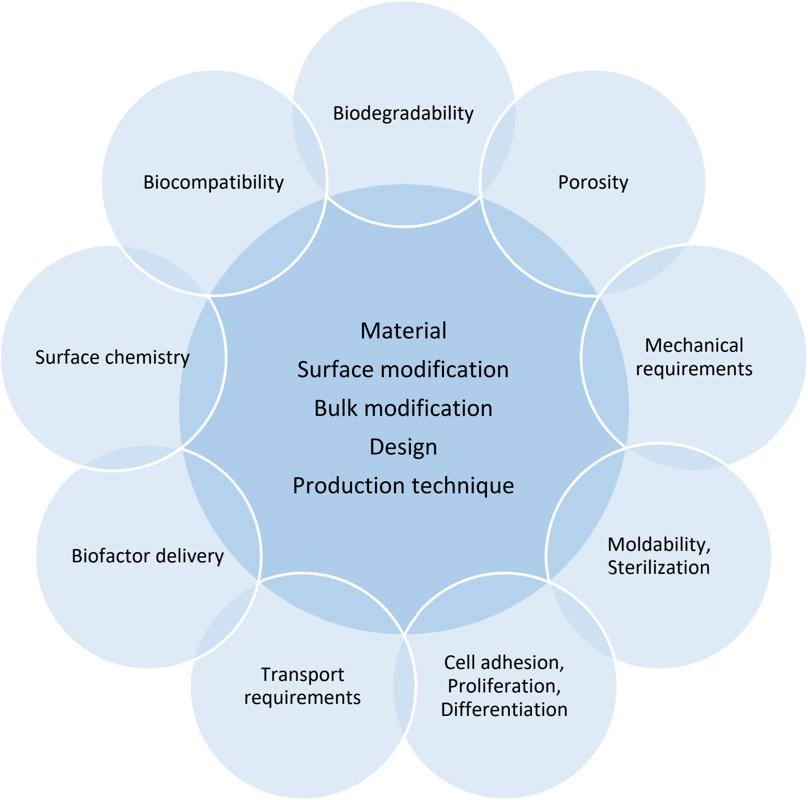

Figure 20: Illustration of the different scaffold properties for TE. While the chemical nature of the biomaterial influences the biofunctional response, physical properties such as scaffold design and the associated manufacturing methods are key factors for TE as well. Based on [65].

Although several methods like porogen leaching[194], gas forming[195], phase separation[196], freeze drying[197] and others[169] are in lab use for scaffold fabrication, none of them can achieve such reproducible and precisely defined scaffolds like AM processing. On the contrary, AM methods show usually a lack of proper structural resolution limits in the micrometre range. Rare exceptions to this, including two-photon-polymerisation (2PP)[198], are limited by the accessible biomaterial choice, low processing speed or extraordinary high device costs. Here, it must be mentioned that methods related to elevated temperatures are often not suitable for an incorporation of sensitive biomolecules for advanced cell stimulation into the scaffold's biomaterial.

The benefit of accurate structuring was proven to trigger biological functions. For instance, the vascular density could be maximised by designing scaffolds with 30-40 µm interconnecting pores. Interestingly, this result was obtained using different materials and *in vivo* implant sites.[191] It is hypothesized that macrophages, as part of the immune system, can be guided towards a specific phenotype which is important for the healing progress by structuring of the pore size.[191, 199] Furthermore, gradient structures have become an important subject of investigation recently and can be understood as remarkable opportunity to guide cell behaviour and act as appropriate tool to engineer complex tissue interfaces as consequence.[200-202] Accordingly, it must be clarified whether effects triggered by biomolecules can be (partially) substituted by superior design of scaffolds in order to minimise effort, material complexity and to maximise scaffold performance or to avoid more complicated approval procedures finally. However, MEW shows a very high potential according to the discussed physical design criteria (Figure 20) and should be able to comply with all necessary requirements for fabrication in the lab and for medical applications. Further, the synthetic polymers utilised by extrusion AM, are a reasonable option as biomaterials.

2.4 Synthetic polymers as biomaterials

In contrast to naturally based polymers for TE like collagen[203], chitosan[204], alginate[205], hyaluronic acid[206], glycosaminoglycans[207], elastin[208], fibrin[209] and others, synthetic polymers often exhibit lower performance regarding bio-functional interactions. Nevertheless, synthetic biopolymers are more reproducible, tuneable, available, cost-effective and more likely being approved as medical product by notified bodies.[210] Additionally, natural biopolymers may exhibit a lack of mechanical properties [191] and processability due to missing thermoplasticity as most of them are prone to denaturate when exposed to elevated temperatures.[211] Here, thermoplastic and aliphatic polyesters as biomaterials group can bridge the gap between TE and processing requirements.

The group of aliphatic polyesters contains a wide range of different hydrolytically biodegradable polymers that have been intensively studied over the last decades.[210] As some of the most important examples, polyglycolides (PGA), polylactids (PLA) and poly(ε-caprolactone) (PCL) can be synthesised via ring opening polymerisation (ROP), thermodynamically driven by the molecular ring strain of the monomers (Figure 21)[212]. Polycondensation as synthesis is indeed feasible, but to an expense of some drawbacks. Due to the “living” polymerisation via ROP, the control and production of higher molecular weights as well as a more narrow molecular distributions are more practicable for instance.[213]

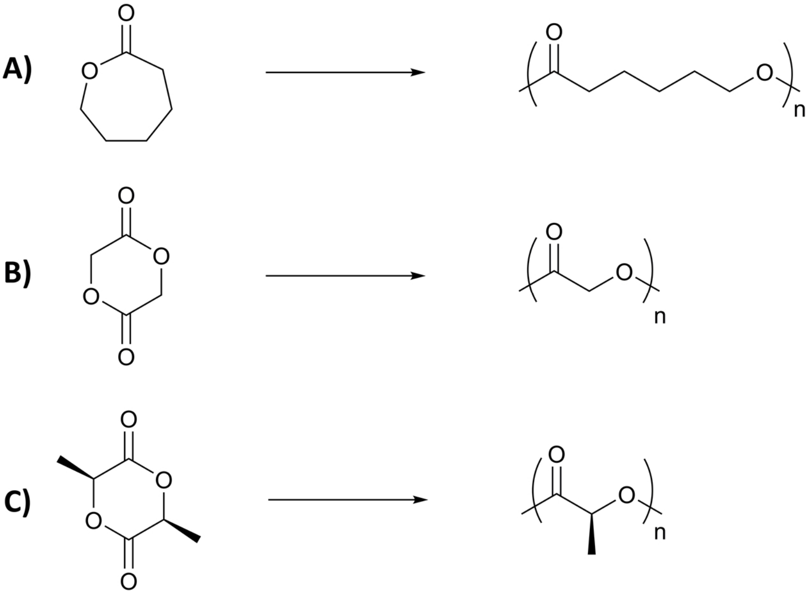

Figure 21: ROP of different homopolyesters. A) ε-caprolactone results in PCL, B) 1,4-Dioxane-2,5-dione results in PGA and C) 3,6-Dimethyl-1,4-dioxane-2,5-dione results in PLA. Based on [212].

While the degradation rate *in vitro* and *in vivo*, mainly controlled by hydrolysis, depends on the molecular weight, crystallinity, surface properties, stresses, residual monomers, site of implantation and more, the chemical composition is a predominant factor for the implant's lifetime.[210]

2.4.1 Polyglycolide

More than hundred years known now, polyglycolides (PGA) are composed of ester and methylene groups. Glycolic acid as degradation product of PGA is a natural metabolite[210] and can be enzymatically converted to glycine or pyruvate *in vivo*. Thus, it is available for protein synthesis, enters the tri-carboxylic acid cycle or is excreted by urine.[214, 215] This polymer can be seen as the simplest in the group of polyesters. As a result of the chemical architecture, PGA does not exhibit a specific tacticity and crystallises with a 46-50 % ratio.[210, 216] Even though, degradation rates *in vivo* can alter and be very high, ranging from 2-3 months in patients[217], about 12 weeks in cancellous bone of rabbits[218], to 4 or 5 months in sheep's femora[219] or require more than 9 months in rat's tibial cortices[220]. In all presented cases, the polymer degradation was followed by bone growth underlining a suitable TE performance. On the downside, the degradation progress follows a bulk erosion by water diffusion and chain scission in the polymer accompanied by a sudden loss of mechanical properties.[212] This is also followed by a decrease of the local pH value resulting in inflammation and damaged tissue in some cases.[210] Nevertheless, PGA has been widely used for medical applications like nerve guides[221], resorbable sutures[222] or postsurgical defect treatments[223]. However, the combination of the distinct sensitivity to hydrolytic degradation[210] with the relatively high melting point of 224-228 °C[216] makes (reproducible) processing via MEW challenging.

2.4.2 Polylactide

As one of the most extensively used medical polyesters, polylactides or poly(lactide acid) (PLA) can be present in three different isomeric forms: D(-), L(+) and as racemic mixture D,L.[210] Depending on this chirality of the monomers, the crystallinity of the resulting polymer can be tuned.[224] In contrast to PGA, PLA exhibits an additional methyl group in the repetition unit leading to increased hydrophobicity and thus, decreased hydrolysis rates.[225] While isotactic PLA melts at 185 °C in its α-form and at 175 °C in its β-form,[226] the melting temperature can even disappear for amorphous poly(D,L-lactide)s. As a result of this structural diversity, the *in vivo* degradation rate can drastically vary, ranging from several years in patients [227] or in between 12 months.[177, 228] As glycolic acid, lactide acid is a natural molecule present in the body and can be similarly metabolised, preferably in its L-isomeric form.[210] The morphological adjustability combined with suitable mechanical and bio-related properties indeed is favourable and has PLA brought the reputation as gold standard for orthopaedic surgery.[228] Some examples in medical use are screws, fixation grafts and resorbable reconstruction implants for soft and hard tissue.[228] Nonetheless, PLA is far from being a perfect biomaterial. During degradation, the polymer can face similar issues of bulk erosion as loss of mechanical integrity and accumulation of acidic reaction products with the potential to harm the host tissue.

2.4.3 Polycaprolactone

Some scientists have the opinion that poly(ε-caprolactone) (PCL) is overall the most widely studied of the polyester family.[210] PCL exhibits an excellent processability by extrusion AM explained by the low melting temperature of 59–64 °C and the relatively high stability to hydrolysis degradation, compared to PLA or PGA. In addition, it has been claimed that PCL crystallises up to 69 %[229] further promoting the high degradation stability. For example PCL had been used as contraceptive delivery implant degrading only to 50% in four years[217], whereas even nanofibre meshes with extremely high specific surfaces showed a molecular weight reduction of 27 % only after 90 days *in vivo,* conducted in rats.[230] Especially in the case of a predominant surface degradation, enzymatically chain scission can play an important role as well.[217] Indeed, PCL’s slow degradation rate may not be suitable for many short-term applications, but apart from this issue, PCL degrades mainly by surface erosion allowing a nearly zero-order release kinetic for incorporated drugs[225] and a more predictable mechanical behaviour in the host site over time.

2.4.4 Copolymers

Besides the discussed homopolymers, several other polyesters such as polydioxanone[231], poly-4-hydroxybutyrate[232], poly(propylene fumarate)[233] or poly(ortho esters)[234] have been used for TE approaches. However, the copolymerisation of different monomers can be a reasonable tool for tuning the polymers performance properties and synergising the benefits of different polymers. While copolymers such as poly(lactic-*co*-glycolic acid)[235] exhibit relatively high degradation rates and thus, have been widely used for fast resorbing implants, other copolymers based on lactid acid and ε-caprolactone can exhibit increased mechanical properties[236]. However, the complexity of TE and clinical applications allow no general guideline, the fine tuning and balancing of polymer properties remains a question of processing feasibility, application requirements and financial aspects in the end.

3 Fibre pulsing during MEW

Parts of this chapter have already been published in the following two articles:

Gernot Hochleitner, Almoatazbellah Youssef, Andrei Hrynevich, Jodie N. Haigh, Tomasz Jungst, Jürgen Groll and Paul D. Dalton

“Fibre pulsing during melt electrospinning writing”

Bionanomaterials 2016, DOI: 10.1515/bnm-2015-0022

Gernot Hochleitner, Julia Franziska Hümmer, Robert Luxenhofer, Jürgen Groll

„High definition fibrous poly(2-ethyl-2-oxazoline) scaffolds through melt electrospinning writing”

Polymer 2014, DOI: 10.1016/j.polymer.2014.08.024

Presented experiments, data evaluations and writing were accomplished independently in this chapter, if not clearly stated otherwise.

3.1 Introduction

In order to use MEW as manufacturing method for TE scaffolds efficiently, a controlled high quality process must be established at first. So far, MEW is indeed barely investigated, but especially no profound approaches focusing on printing fidelity or processing instabilities have been presented in literature yet.

Therefore, the analysis of one of the most important MEW instabilities, a periodical fluctuation of the printed fibre diameter, were conducted. Due to the visible nature of the fibre's morphological changes, the terms *pulsing* for common cases and *long beading* for the extreme cases of this instability have been chosen. In this chapter, a hypothesis concerning the physical origin and a systematic investigation addressing the influence of the instrumental parameters is given. Further, a discussion and guideline was introduced to quantify and avoid or at least minimise *pulsing* or *long beading*.

The presented study was conducted using both, PCL as standard biofabrication polymer and only available MEW material until now, and Poly(2-ethyl-2-oxazoline) (PEtOx). The latter was processed with MEW for the first time and chosen as second material to prove and analyse the influence of *pulsing* and *long beading* comprehensively.

The polymer group of Poly(2-oxazolines) (POx), as very promising materials for TE research and application, has been intensively studied over the last ten years.[237-242] Reasons for this are numerous, particularly the utilisation of the living, cationic ROP offers the opportunity to directly tailor the performance properties easily by tuning the side groups of the 2-oxazoline monomers.[239, 243] Here, for instance the hydrophobic/hydrophilic characteristic of the macromolecules can be adjusted leading to a sharp and exactly defined lower critical solution temperature (LCST) in water.[237] This resulting thermo-sensitivity makes POx a highly interesting polymer for pharmaceutical or drug delivery applications.[244, 245] Consequently, this polymer group has been compared to and discussed as an alternative for the “gold standard” PEO[246], a hydrophilic biopolymer. In this context, POx was studied regarding the so-called “stealth properties” to immune reactions[247], the biocompatibility[248], the outstanding capacity of drug or protein storage[249, 250], as antimicrobial or non-fouling material[251] and more.

The beneficial tuneability of the polymer’s chemical structure also leads the adjustability of the physical processing properties. This circumstance, in addition to the thermoplasticity and the very low electrical conductivity, highlights POx as considerable polymers for MEW application. Further, PEtOx is considered as amorphous, water-soluble and a relatively thermal stable polymer[2] allowing both, a thermoplastic processability and a clearly different set of application properties compared to PCL. Thus, investigation and optimisation of PEtOx processing via MEW not only helps to deepen the understanding concerning stable printing, but also broadens the versatility of MEW as tool box for TE approaches.

---

[2] Physical properties have been assessed by the supplier Sigma-Aldrich Co. LLC, 07.10.2016; http://www.sigmaaldrich.com/catalog/product/aldrich/372846?lang=de&region=DE

3.2 Experimental section

3.2.1 Polymer

PCL, as a good manufacturing practice (GMP) grade material, was purchased from Corbion Inc. (CAS# 24980-41-4, PURASORB PC 12, Lot# 1412000249, 03/2015, Gorinchem, Netherlands) and PEtOx from Sigma-Aldrich Co. LLC. (CAS# 25805-17-8, St. Louis, USA). Both polymers were used as received.

3.2.2 MEW devices

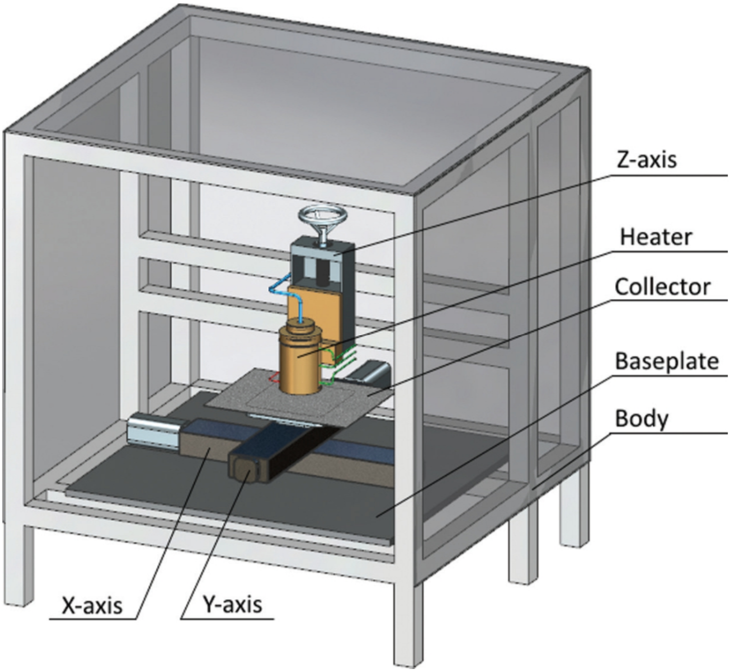

Figure 22: Schematic of a MEW device. A thermoplastic polymer is filled into a syringe and molten by an electrical heater. The melt is fed through a spinneret connected to a HV electrode. After leaving the spinneret, the polymer melt forms fibres by EHD principles which are deposited in a controlled way using a collector and computer controlled axes system.[252]
(Image by Andrei Hrynevich, published under Creative Commons licence CC BY-NC-ND 3.0)

Two custom-made MEW devices with different technical performance characteristics were developed and used in the presented study. Both are based on commercially available Computer Numerical Control (CNC) technology and assembled using an aluminium framework housing with polycarbonate windows. A schematic of a MEW device is presented in Figure 22.

3.2.2.1 High-temperature device

In order to process polymers at elevated temperatures, an electrical heating spiral was mounted into a custom-made polyetheretherketon housing and equipped with glass syringes with metal Luer-Lock from Poulten & Graf GmbH (FORTUNA OPTIMA®, 3 ml, Wertheim, Germany) as melt reservoir. The heat control was conducted via proportional-integral-derivative-regulator (PID) (TR400, Delta-t, Bielefeld, Germany). Driven by nitrogen gas (N_2) pressure using a manual proportional regulator from Festo GmbH (Berkheim, Germany), the melt was fed through prepared metal cannulas (UNIMED, Lausanne, Switzerland), connected to a tailor-made brass HV electrode and HV source (DX250R, EMCO, Hallein, Austria). The voltage measurement and control was performed via custom-made electronical divider and a multimeter (Digit Multimeter 2100, Keithley, Cleveland, USA). The collector-plate made of aluminium was moved by two orthogonally assembled ball-screw axes (XSlide, Velmex, New York, USA) in planar directions. Connected to a computer, G-code programming (MACH 3 CNC software, ARTSOFT, Livermore Falls, USA) was conducted for motion sequencing.

3.2.2.2 Low-temperature device

In contrast to the *high-temperature device*, the *low-temperature device* was designed to process PCL only. Here, additional features for a process optimisation were implemented. These included a bi-zonal electrical heater from Bach

Resistor Ceramics GmbH (custom-made components, Seefeld, Germany) controlled by two PIDs (dTron 316, JUMO GmbH & Co. KG, Fulda, Germany) to melt PCL in polymeric syringes (fluid dispensing system, Optimum® 3cc, Nordson EFD Deutschland GmbH, Pforzheim, Germany). Further, pre-machined and thus, reproducible spinnerets (Precision Tips, Nordson EFD Deutschland GmbH, Pforzheim, Germany) were utilised. In order to merge peripheral components, programmable logical controllers with a software solution (Bosch Rexroth AG, Lohr am Main, Germany) were used including a pneumatic control (Bosch Rexroth AG, Lohr am Main, Germany). Additionally, HV sources (LNC 10000-5 positive and negative, Heinzinger Electronic GmbH, Rosenheim, Germany) were utilised analogously and in order to apply HV at the electrode and the collector plate to generate a versatile electrical field gradient.

3.2.3 Manufacturing conditions

As already known from literature and discussed in the chapter **Instrumental parameters** on page 32ff, different instrumental parameters impact MEW processing of PCL. Here, the interaction between CTS and the diameter of the jet or the fibre respectively were investigated specifically. Therefore, the parameters acceleration voltage U at a fixed spinning distance h and spinneret size (with an inner diameter IØ) as well as the feeding pressure p were investigated concerning stable processing as presented in Table 3. The remaining parameters (e.g. temperature T) were kept constant, if not otherwise stated in the results and discussion section.

Table 3: Instrumental parameters for stable printing investigations of PCL. The collector was charged with U = -1.5 kV, presented values are the absolute potential difference. During p variation U was kept constant and vice versa. Standard parameters are printed in bold.[252]

IØ in G (= µm)	**T in °C**	**p in bar**	**U in kV**	**h in mm**
22 (= 413)	73	0.2	4.50	4.0
		0.5	5.25	
		1.0	**6.00**	
		2.0		

In contrast to PCL, the processability of PEtOx was analysed fundamentally including a systematic study on spinning temperature, feeding pressure, spinning distance, spinneret sizes at proper collector speeds matching CTS between 200 and 400 mm·min^{-1}. Hence, a conclusion on stable printing physics could be drawn and compared to PCL from a phenomenological point of view. The instrumental parameter matrix is provided in Table 4.

Table 4: Instrumental parameters for processability investigation of PEtOx. During variation of the different instrumental parameters, others were kept constant at the middle of the range, indicated by bold type.[136]

IØ in G (= µm)	**T in °C**	**p in bar**	**U in kV**	**h in mm**
30 (= 160)	200	1.0	3.0	3.0
27 (= 210)	205	1.5	4.0	4.0
25 (= 260)	**210**	**2.0**	**5.0**	**5.0**
23 (= 337)	215	2.5	6.0	6.0
	220	3.0	7.0	7.0

Between single instrumental parameter changes, at least t = 10 min of stabilisation time was implemented. The investigations were conducted at room temperature 21 ± 2 °C and 35 ± 15 % r.h. Measured values contain the standard deviation of a sample (SD) defined as:[253]

$$SD = \sqrt{\frac{1}{n-1} \cdot \sum_{i=1}^{n} (y_i - \bar{y})^2} \tag{11}$$

y_i = ith value of the set; $\bar{y}$ = sample mean; n = sample size

3.2.4 G-code programming

In order to investigate the processability and stable regimes of MEW printing, simple G-codes were used. Thus, grid structures and line arrays were programmed for regular fibre deposition to enable a practical optical analysis. Presented grids are composed of square shaped boxes, printed by 0° and 90° layer alternation.

Example G-codes using the MACH3 software for PEtOx printing are provided in the supplementary information chapter **PEtOx fibre scaffolds** on page xxvii f.

3.2.5 Optical Imaging

Different optical methods were performed for visualisation and fibre diameter quantification. Presented Imaging of the jet was conducted using an AxioCam 105 colour digital camera (Carl Zeiss AG, Oberkochen, Germany) including a 75 – 300 mm lens (Kenko Tokina Co., Ltd., Tokyo, Japan). For fibre diameter measurement and imaging, a stereomicroscope (Discovery V20, Carl Zeiss AG, Oberkochen, Germany) and the scanning electron microscopes (SEM) Crossbeam 340 SEM and Ultra Plus with an e-Beam column (Carl Zeiss AG, Oberkochen, Germany) were used. To avoid excessive charging of the fibres and radiation based damage resulting in inaccurate analysis, the imaging was performed with 1 – 3 kV at 4 – 7 mm distance. Beforehand grid samples were coated using gold and platinum sputtering with a thickness up to 5 nm to minimise charge artefacts. The line arrays made of PCL were analysed without surface treatment. For a proper quantification analysis n = 20 fibres were chosen for each parameter combination, if not otherwise stated in the description.

3.3 Results and discussion

3.3.1 Considerations on MEW

In the first instance, involved masses and corresponding mass flows for MEW must be considered. It is assumed that no mass loss of the polymers occur during manufacturing, coherently a basic conservation of masses can be outlined:

$$m_1 + m_2 + m_3 = constant$$

Herein, m_1 is the melt in spinneret and reservoir (syringe), m_2 is the mass of the *Taylor Cone* including jet and m_3 is the mass of the deposited material, with their related mass flows dm_1/dt, dm_2/dt and dm_3/dt as schematically presented in Figure 23.

To enable analysis of stable versus unstable printing conditions, the mass flow dm_1/dt was kept constant during every single experiment with $d^2m_1/dt = 0$. Further, printed fibre mass flows dm_3/dt were analysed regarding constancy or oscillation behaviour necessitating constant collector speeds during each single experiment consequently. By utilising this approach in combination with constant jet spinning excluding *Rayleigh* instabilities, conclusions could be drawn about the time-dependent dm_2/dt of the molten jet.

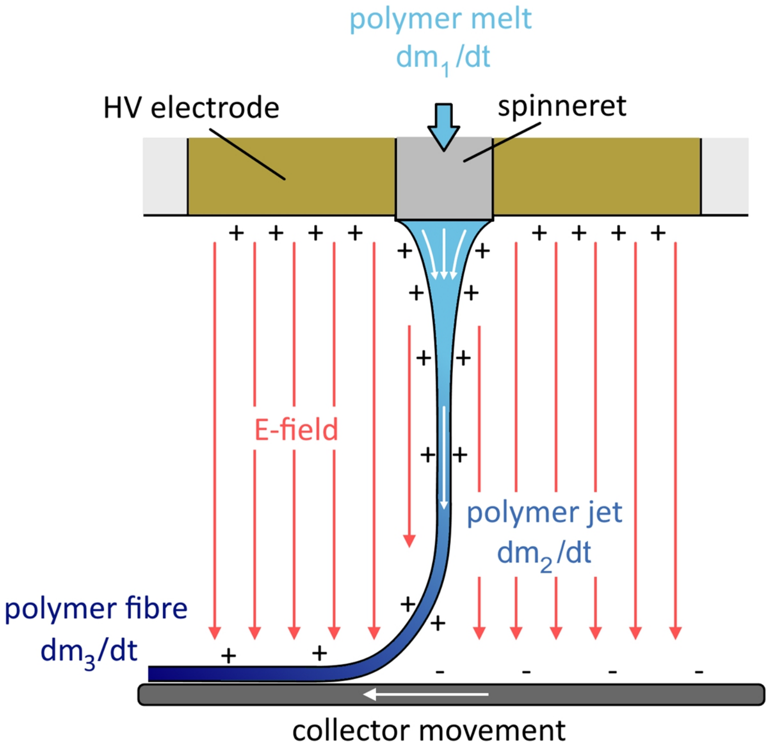

Figure 23: Schematic explanation of MEW printing and involved mass flows. The polymer melt was fed through the spinneret with dm_1/dt. Subsequently a polymer jet had been formed and became accelerated with dm_2/dt towards the collector surface. Finally fibres were deposited with dm_3/dt. [252]
(Published under Creative Commons licence CC BY-NC-ND 3.0)

3.3.2 MEW processing investigation with PCL

3.3.2.1 Influences on deposition characteristics

As presented in Figure 24 A-C, collector speeds increased above CTS mechanically stretch the jet and thin the resulting fibre diameter further to the HV field. While a collector speed s_c matching 1.0 x CTS led to fØ = 58 µm fibre diameters, s_c = 2.0 x CTS led to thinner fibres with fØ = 42 µm.

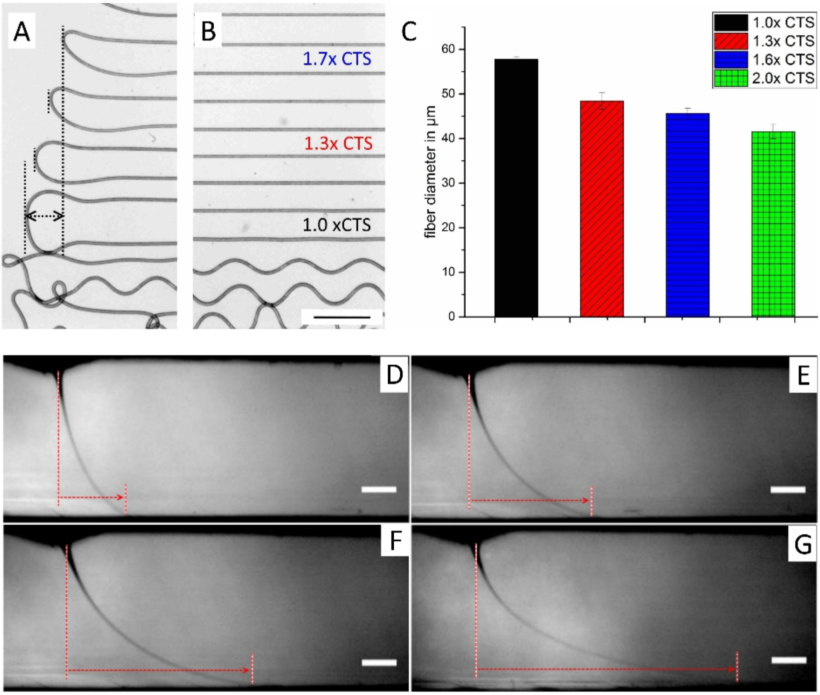

Figure 24: Influence of high collector speeds on jet, fibre and deposition behaviour. A-C) At collector speeds s_c > CTS mechanical stretching with jet lags occurred influencing the deposition accuracy and the resulting fibre diameter. 1.0 x CTS: fØ = 57.7 ± 0.6 µm, 1.3 x CTS: fØ = 48.4 ± 1.8 µm, 1.6 x CTS: fØ = 45.6 ± 1.2 µm, 2.0 x CTS: fØ = 41.6 ± 1.6 µm. Experiments were performed with a 23 G spinneret, 5.7 kV acceleration voltage, 4.4 mm spinning distance, 3.0 bar feeding pressure at 82 °C spinning temperature. D-G) Imaging of the increasing jet lag with increasing collector speeds s_c as indicated by the red arrows. D) 500 mm·min^{-1} (1.8 x CTS), E) 1000 mm·min^{-1} (3.6 x CTS), F) 2000 mm·min^{-1} (7.1 x CTS) G) 8000 mm·min^{-1} (28.6 x CTS). Experiments were performed with a 22 G spinneret and 6.5 kV, 6 mm, 1.0 bar at 73 °C. All scale bars are 1 mm; CTS = 280 ± 10 mm·min^{-1}.[252]
(D-G: Image by Andrei Hrynevich, published under Creative Commons licence CC BY-NC-ND 3.0)

In case of FDM deposition, significantly increased collector speeds may lead to detachment of the deposited polymer strand reducing the usability of increased collector speeds as thinning approach. However, utilising this mechanical stretching with MEW performs superiorly due to the electrostatic attraction between jet and collector surface. While this effect was principally known [107, 137], this observation is nevertheless of major interest in order to assess further effects on printing and deposition control.

At increased ratios of s_c/CTS, so called jet lags could increasingly be observed as presented in Figure 24 D-G. This determined the shift of the first contact point of the jet on the collector in contrast to the position of the spinneret. A huge lag largely leads to a loss of fibre deposition control generally. While a linear deposited fibre by translational collector movement is not affected in placement, such lags are visible at turning points and influence fibre diameter and deposition due to changes in the mechanical drawing conditions.

In addition to this, the jet diameter, determined by the melt feed dm_1/dt amongst others, influences the fibre diameter and CTS clearly. This behaviour is shown in Figure 25, $p = 0.5$ bar led to fØ = 7.7 ± 0.8 µm and CTS = 675 $mm\cdot min^{-1}$, $p = 1.0$ bar to fØ = 8.8 ± 0.5 µm and CTS = 375 $mm\cdot min^{-1}$, $p = 2.0$ bar fØ = 10.7 ± 0.8 µm and CTS = 225 $mm\cdot min^{-1}$and $p = 3.0$ bar to fØ = 14.8 ± 2.0 µm and CTS = 200 $mm\cdot min^{-1}$ finally.

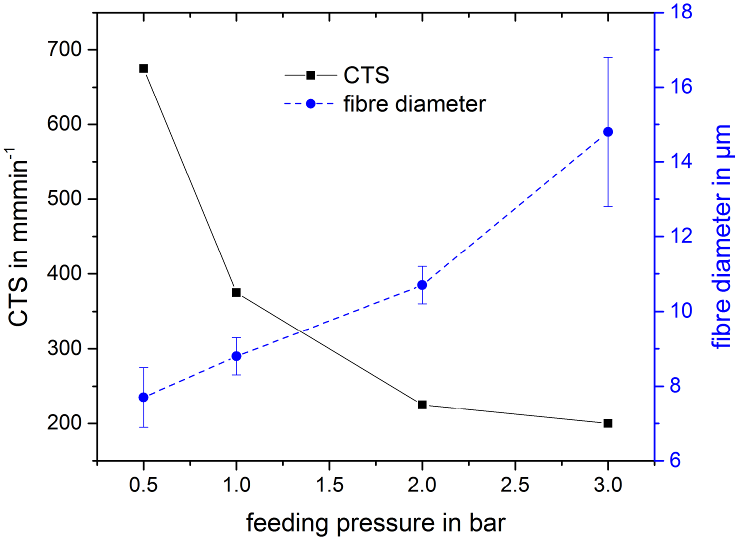

Figure 25: Changes of fibre diameter and CTS as function of the feeding pressure. While an increased feeding pressure led to increased fibre diameters, an accompanying decrease of the jet's CTS could be observed. Experiments were performed with a 30 G spinneret, 2.5 kV acceleration voltage, 1.0 mm spinning distance at 90 °C spinning temperature. n = 10 fibre lines of n = 5 different samples each.

Here, the full spectrum of complex parameter interactions on MEW processing including (EHD) cooling, viscoelastic stretching effects etc. cannot be assessed in detail, nevertheless, a qualitative consideration is provided trying to understand the reciprocal dependency of the jet cross-section and the CTS.

Firstly, a sufficient charge injection by the HV source at the spinneret-polymer interface and a constant surface charge density on the PCL jet must be assumed. Taking the very poor electrical conductivity of the GMP grade PCL into account, a very low charge density can be expected in the bulk of the melt. The extent of polarisation effects and resulting properties or behaviour of the PCL in the HV field is unknown and requires further investigation. Basically, jet stretching forces face counteracting forces in the jet. With a decrease in CTS, a decreasing sum stress vector (resulting force/area) onto the collector can be concluded caused by higher feeding pressures or higher dm_1/dt respectively. This indicates an over-proportionally increase of counteracting stress by viscoelasticity or flow resistance and surface tension compared to the dominating EHD-driven stretching stress. This might be attributed to the jet cross-section area (counteracting stress) proportional to r_{jet}^2 compared to the jet cross-section charged surface (stretching stress) proportional to r_{jet}. However, the CTS dependency with accompanying changes in jet geometry during processing must be considered to assess and avoid unstable printing conditions.

3.3.2.2 Temporary fibre diameter fluctuation

While different types of time-dependent fibre diameter fluctuations can be distinguished, the *temporary pulsing* can be ascribed to a temporal disequilibrium of forces acting on the jet. Hereby, the impression of a dampened oscillation at the fibre array's edges emerge. The reason for this behaviour can be clarified by spending attention to the discussed dependency between jet geometry and the jet speed as shown in Figure 26. While thin jets exhibited a higher speed than thick jets, an oscillating variable lag accompanies an oscillating jet diameter. This observation requires printing at collector speeds always above CTS and clearly visible at the edges of fibre arrays. This phenomenon has affected the quality of printed scaffolds dramatically and can be explained by immediate changes in processing conditions or instrumental parameters shifting the forces balance to another equilibrium level. Incidentally, dm_2/dt and dm_3/dt start to oscillate ($d^2m_2/dt \neq 0$ and $d^2m_3/dt \neq 0$) as a consequence at an always constant dm_1/dt

($d^2m_1/dt = 0$). This temporary affected dynamic balance stabilises usually after several minutes again during MEW printing.

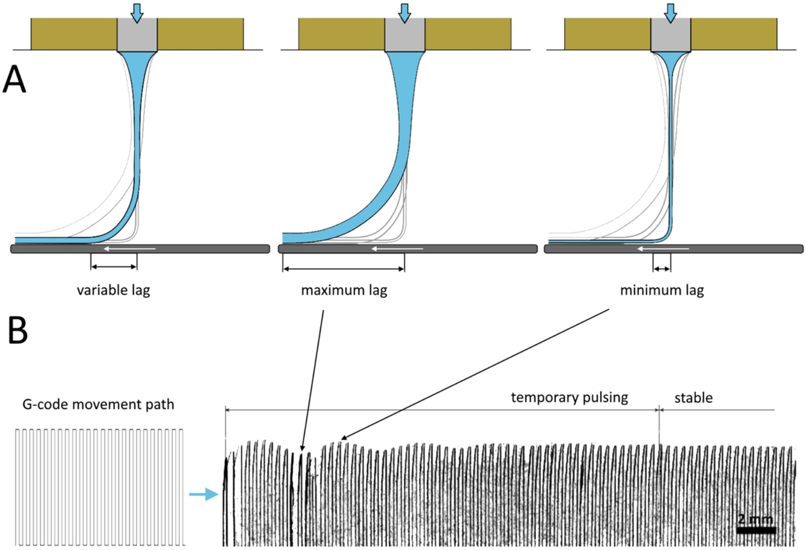

Figure 26: Influence of pulsing on the lag of the jet. A) Schematic of pulsing and illustration of the interaction between jet diameter and the jet lag. During pulsing, the jet diameter oscillates between thick and thin and vice versa leading to a direct change in CTS. This is expressed by a direct oscillation of the variable lag at constant collector speeds. B) Utilising regular G-code movement and collector speeds always above CTS, the pulsing phenomenon can be easily observed at the turning edges of a fibre array in form of a wave-like structure. In case of temporary pulsing, initially unstable printing can be observed merging into stable conditions with a clearly linear edge of the fibre array. Microscopy was conducted using dark field, the image was black/white inverted afterwards for improved visibility.[252]
(B: Image by Andrei Hrynevich, published under Creative Commons licence CC BY-NC-ND 3.0)

This processing instability led to poor manufacturing quality scaffolds and must be taken into account during processing. Hence, instrumental parameters like feeding pressure or acceleration voltage must be adjusted and controlled carefully, similar to *continuous pulsing*.

3.3.2.3 Permanent fibre diameter fluctuation

While *temporary pulsing* by definition disappears over time, *continuous pulsing* and *long beading*, as extreme case, can be defined as permanently occurring fibre diameter fluctuations. As shown in Figure 27, such instabilities can be appropriately enforced by excessive polymer melt flow dm_1/dt via widely adjustable high feeding pressures (0.2 to 2.0 bar in this study).

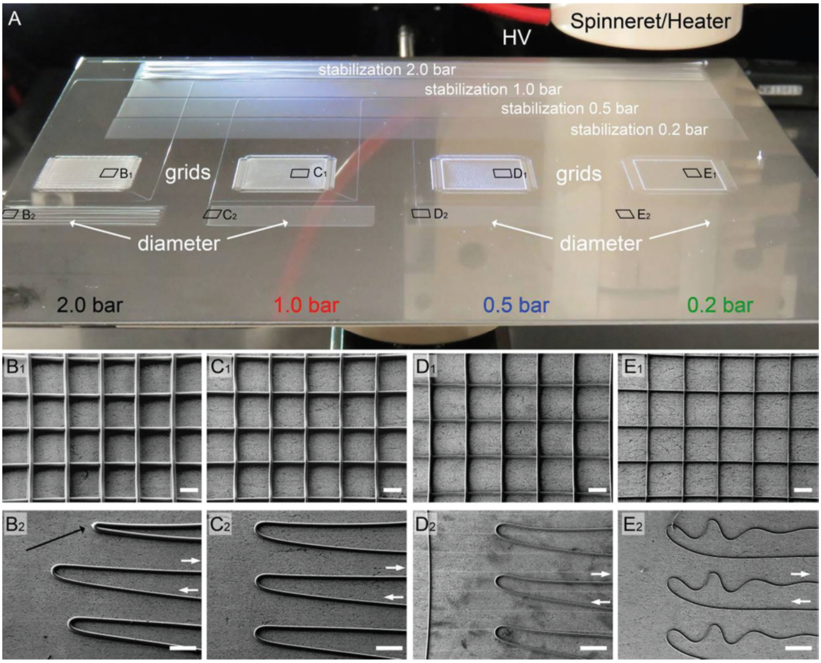

Figure 27: MEW deposition using different feeding pressures. A) Photographical image of the MEW collector. To assure constant printing conditions, stabilisation arrays were printed prior to the presented line arrays and grid structures for diameter analysis. While p was varied from B) 2.0 bar, C) 0.5 bar, D) 1.0 bar E) to 2.0 bar, other parameters were kept constant. Long beading (2.0 bar) occurred at high pressures, low pressures led to stable printing conditions. B-E) white arrows indicate the printing direction, the black arrow significant changes in fibre diameter. Scale bars = 100 µm.[252]
(A: Image by Almoatazbellah Youssef, B-E: Image by Jodie N. Haigh, published under Creative Commons licence CC BY-NC-ND 3.0)

At this point it must be stated that none of the chosen parameter combinations led to dye swell or additional processing instabilities. As proof, common extrusion experiments with the used MEW setup at intensified conditions with p = 4.0 bar have been conducted showing no extrudate swelling after leaving the 22 G spinneret.

While a relatively small melt feed dm_1/dt with p = 0.2 bar, 0.5 bar and 1.0 bar led to stable printing conditions with homogeneous fibres ($d^2m_3/dt \approx 0$) and thin diameters with fØ = 7.36 ± 0.35 µm; 11.04 ± 0.41 µm and 15.40 ± 0.60 µm (Average ± SD), an excessive pressures led to unstable printing conditions. Here, the high melt feed dm_1/dt with p = 2.0 bar led to *long beading* with huge fibre diameter fluctuation indicated by fØ = 19.41 ± 8.16 µm. Under these practical terms, the MEW printed PCL fibre diameter can be indeed adjusted, but towards thicker fibre diameters increasing the feeding pressure is limited consequently.

In contrast to the feeding pressure, changes in the acceleration voltage or electrical field strength (due to fixed spinning distances) do not influence the melt feed or throughput dm_1/dt as such, but rather the jet mass flow dm_2/dt directly. As presented in Figure 28 high acceleration voltages U = 6.00 kV were required for avoiding instabilities with fØ = 15.56 ± 0.46 µm, whereas average voltages U = 5.25 kV led to *continuous pulsing* with fØ = 15.50 ± 1.16 µm or even *long beading* at low voltages U = 4.50 kV with fØ = 8.21 ± 5.61 µm. Indeed the workable range for the minimum voltage (*Taylor Cone* formation) to the maximum voltage (arcing discharge) is more limited than the feeding pressure, nevertheless, the influence of the electrical field is fundamental.

Summarising the observations regarding the pressure and voltage influence on printing stability, a hypothesis can be formulated. While both, high pressures and low voltages led to fibre diameter fluctuations with $d^2m_3/dt \neq 0$ necessitating jet fluctuations $d^2m_2/dt \neq 0$, the melt mass flows dm_1/dt and jet mass flow dm_2/dt must be balanced by involved force equilibrium.

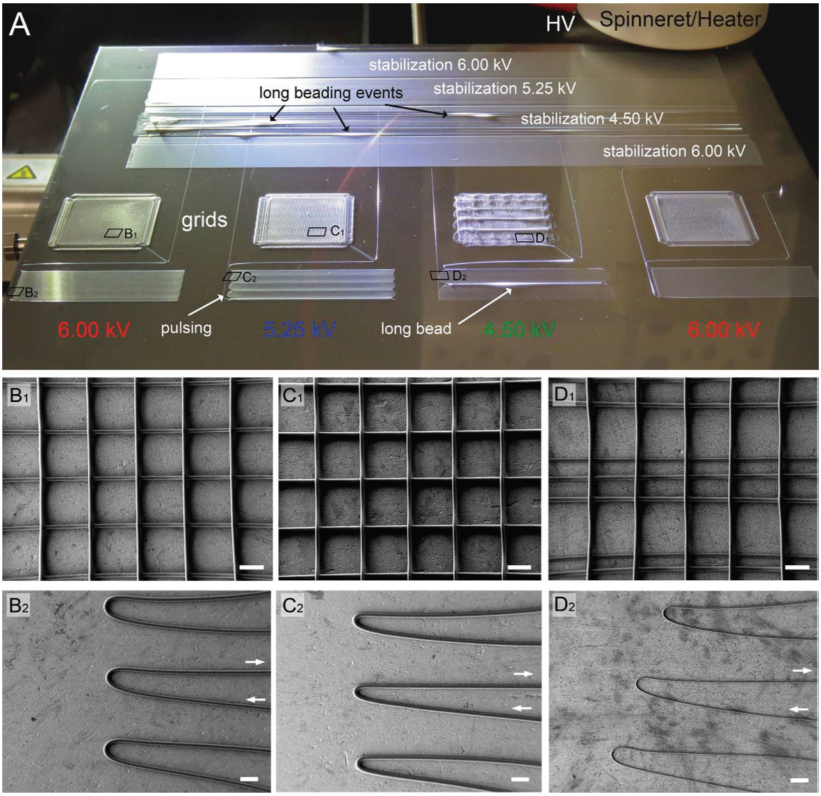

Figure 28: MEW deposition using different acceleration voltages. A) Photographical image of the MEW collector. To assure constant printing conditions, stabilisation arrays were printed prior to the presented line arrays and grid structures for diameter analysis. While U was varied from B) 6.00 kV, C) 5.25 kV to D) 4.50 kV, other parameters were kept constant. Stable printing was possible at high voltages (6.00 kV), continuous pulsing occurred at average voltages (5.25 kV) as well as long beading at low voltages (4.50 kV). B-D) white arrows indicate the printing direction. Scale bars = 100 µm.[252]
(A: Image by Almoatazbellah Youssef, B-E) Image by Jodie N. Haigh, published under Creative Commons licence CC BY-NC-ND 3.0)

Here, a strong electrical field may have induced high stretching forces leading to increased material pull and thus a homogenous and constant fast jet with $dm_1/dt = dm_2/dt = \text{constant}$. High pressures in contrast lead to excessive material extrusion overcoming the mass flow capability of the electrical field. As result during MEW printing, a jet with progressively increasing diameter can be observed. In addition, polymer mass accumulates at the spinneret tip over time due to the excessive melt flow (temporary: $dm_1/dt > dm_2/dt$). This is accompanied by a progressively decreasing CTS or increasing jet lag. At this point the delay time of the polymer increases further while the mechanical drawing by the constant collector movement becomes more and more prominent (analogously to Figure 26 A). As a result, the accumulated polymer melt becomes stretched, removed from the spinneret tip and abruptly deposited on the collector surface (temporary: $dm_1/dt < dm_2/dt$). This instability phenomenon occurs frequently and regularly over time. Considering very long manufacturing times, the basic condition with average values: $\lim_{t\to\infty} \frac{dm_1}{dt} = \frac{dm_2}{dt} = \frac{dm_3}{dt}$ is valid.

The presented hypothesis is supported by the fibre diameter quantification as a function of time allowing to assess dm_3/dt. As presented in Figure 29, the degree of instability manifestation and visible appearance determines the classification into *pulsing* or *long beading*. While *continuous pulsing* occurs as sinusoidal fibre diameter oscillation with a relatively high frequency, single extremely thick segments are followed by much thinner fibres for longer delay times during *long beading*. Here, further analysis of the collected data can be helpful to assess the degrees of arising instabilities.

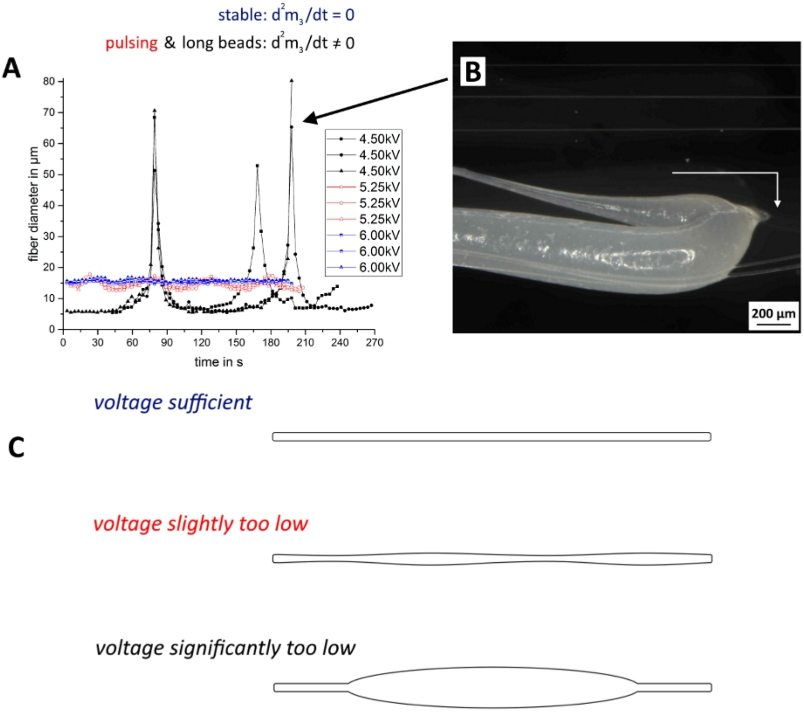

Figure 29: Fibre geometry over time using different acceleration voltages. A) While processing at an acceleration voltage of U = 6.00 kV resulted in homogeneous fibre diameters (blue), U = 5.25 kV led to continuous pulsing with a sinusoidal oscillation diameter-time dependency (red). In the most extreme case with U = 4.50 kV, long beading with clear peaks was observed. Other parameters were kept constant during voltage changes. B) Photographical image of an example long bead at a turning point due to insufficient acceleration voltage. The white arrow indicates the printing direction. C) Morphological illustration of homogeneous, pulsed and beaded fibres.[252]
(Published under Creative Commons licence CC BY-NC-ND 3.0)

3.3.2.4 Analysis of printing instabilities

A sufficient high number of measured fibre lines (n = 60) was crucial to evaluate the data at hand. The fibre quantification is summarised in Table 5. Homogeneously printed fibres exhibited a small coefficient of variation (CV) below 5 % in case of high acceleration voltages U = 6.00 kV in combination with small feeding pressures p = 0.2, 0.5 and 1.0 bar. Conversely, *pulsed* fibres processed at U = 5.25 kV and p = 1.0 bar revealed a CV = 7.5 % whereas *beaded* fibres spun at U = 6.00 kV and p = 2.0 bar led to CV = 42 % or at U = 4.50 kV and p = 1.0 bar even to CV = 68 %.

Table 5: Fibre geometry as a function of the feeding pressure and the acceleration voltage.[252]

	Feeding pressure, bar (at 6.00 kV)				**Acceleration voltage, kV (at 1.0 bar)**		
	2.0	**1.0**	**0.5**	**0.2**	**4.50**	**5.25**	**6.00**
Average, µm	19.41	15.40	11.04	7.36	8.21	15.50	15.56
Median, µm	16.73	15.30	11.04	7.27	6.18	15.54	15.48
SD, µm	8.16	0.60	0.41	0.35	5.61	1.16	0.46
Ratio M/A	0.862	0.993	0.999	0.988	0.753	1.002	0.995
CV, %	42	3.8	3.7	4.8	68	7.5	3.0

Furthermore, the ratio between Median and Average (M/A) value was helpful to investigate the degree of fibre diameter instability. Thus, in case of homogenous or *pulsed* fibres M/A close to 1.00 indicated a fibre diameter distribution similar to a Gaussian curve. In both cases of *long beading* at U = 6.00 kV and p = 2.0 bar and at U = 4.50 kV and p = 1.0 bar, the ratios were clearly shifted with M/A = 0.86 and M/A = 0.75 towards non-symmetric distribution function. Regarding this, a graphical illustration of the sorted fibre diameter function given in Figure 30 can help for data evaluation as well.

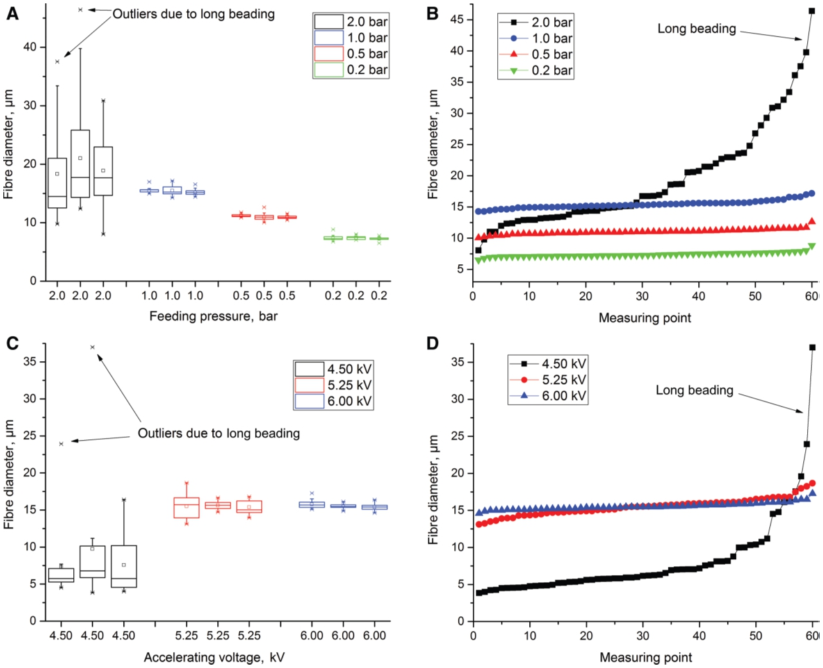

Figure 30: Graphical presentation of fibre diameters using different feeding pressures and acceleration voltages. A&B) The fibre diameters increased clearly at raising feeding pressures. Long beading occurred at high pressures with p = 2.0 bar. C&D) At decreasing acceleration voltages fibre diameter fluctuation became prominent. At U = 5.25 kV pulsing and at U = 4.50 kV long beading occurred. Long beading defects can be classified according to their non-symmetric distribution function and the high gap between minimum and maximum fibre diameters.[252] (Published under Creative Commons licence CC BY-NC-ND 3.0)

3.3.2.5 Comparison to instabilities during melt spinning

While several different manufacturing instabilities[254] like melt fracture or draw resonance are known and described for the widely used polymer melt spinning (MS) technique, its working principle and the experimental setups are nevertheless very different compared to MEW devices. In case of MS, polymer melts are pressed through spinnerets and stretched only by utilisation of mechanical take-up wheels often combined with cooling baths or quench air blowers for enforced solidification.[255-257] For assessing MS instabilities, it is crucial to understand the so called draw down ratio, that is the fibre uptake speed at the wheels divided by the fibre extrusion speed when passing the spinnerets. If a critical draw down ratio is exceeded, the draw resonance instability occurs resulting in fibre diameter oscillation and breakage ultimately.[257-260] Here, it must be stated that a second stable working regime at high draw down ratio has been observed as well, depending on spinning distance between the spinneret and the wheel.[254, 261-264] Nonetheless, the draw resonance phenomenon cannot be compared to MEW processing instabilities due to several reasons. First of all, increasing the acceleration voltage and therefore the draw down ratio during MEW led to homogeneous and not oscillating fibre diameters and second, the instrumental conditions differ vastly: While higher feed rates lead to dye swell and are used for thick fibre processing during MS, the MEW processing feeds and the setup including spinning distances etc. are significantly smaller. Additionally, EHD-driven processing including EHD quenching etc. is based on a different working principle than mechanical fibre spinning, the exact forces distribution and flow characteristics of a MEW jet remain unclear. Hence, a comparison and conclusion between MS and MEW is highly speculative and was therefore avoided in this study.

3.3.2.6 Stable printing of PCL scaffolds

In order to manufacture reproducible scaffolds within small tolerance limits, *long beading* and *pulsing* must be avoided. Significant temporal jet lags accompanying the jet geometry fluctuation during printing direction changes at edges, corners, loops and more complex designs can inhibit precise AM fibre deposition. Different grid scaffolds with ten fibre layers in both planar directions orthogonally to each other (2x10 layers) are presented in Figure 31. In case of instrumental parameter combinations enforcing *long beading* instabilities (U = 6.00 kV with p = 2.0 bar and U = 4.50 kV with p = 1.0 bar), substantial structural defects were observed. Indeed, scaffold samples exhibiting *continuous pulsing* defects (U = 5.25 kV, p = 1.0 bar) do not lack of deposition precision at the first glance, nevertheless, an adverse influence on performance properties may occur. As discussed in the chapter **Melt Electrospinning Writing** on page 29ff, the oscillation of the diameters may result in changed degree or alignment of crystallinity, could further influence the mechanical characteristics or vary the degradation kinetics from fibre to fibre, change the specific surface and more. According to this, only narrow fibre distributions help to design scaffolds with reliable performance properties finally.

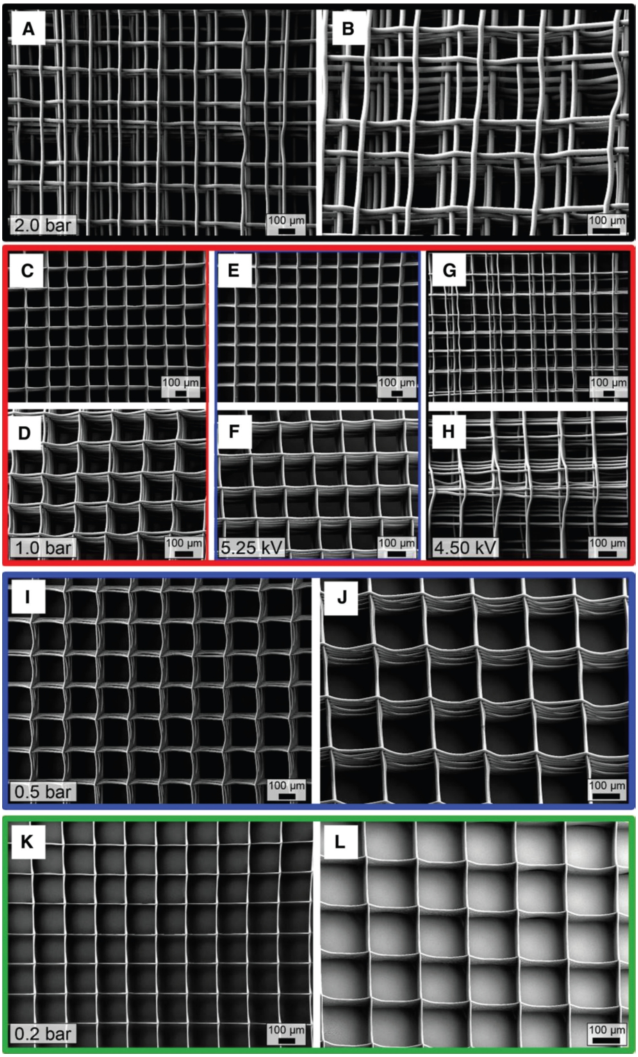

Figure 31: SEM images of MEW printed PCL scaffolds. Scaffolds exhibited 2x10 grid layers, each group contains perpendicular and tilted SEM images. A&B) U = 6.00 kV, p = 2.0 bar, long beaded. C&D) U = 6.00 kV, p = 1.00 bar, stable. E&F) U = 5.25 kV, p = 1.0 bar, pulsed. G&H) U = 4.50 kV, p = 1.0 bar, long beaded. I&J) U = 6.00 kV, p = 0.5 bar, stable. K&L) U = 6.00 kV, p = 0.2 bar, stable.[252]
(Image by Jodie N. Haigh, published under Creative Commons licence CC BY-NC-ND 3.0)

3.3.3 Processability of PEtOx

While PCL as only MEW material has been investigated regarding processability and the affecting instrumental parameters, POx has not been used so far for ES approaches using polymer melts. According to the manufacturer's provided data, PEtOx exhibits a glass transition temperature of T_g = 69-71 °C, a softening point of T_s = 110-120 °C (Vicat, ASTM D 1525-82), a mass average molar mass $M_w \approx 50$ kgmol^{-1} and a polydispersity of $Đ \approx 3\text{-}4$. Such characteristics may be a guideline for polymer processing, however, they can neither be used to predict the processability in general, nor suitable processing temperatures or melt jet behaviour in an external HV field. As presented in Table 4, heating temperatures of T = 200 °C and more were utilised in order to enable a proper *Taylor Cone* formation and suitable jet flow characteristics. Figure 32 illustrates a defective structure as outcome for non-optimised process parameters.

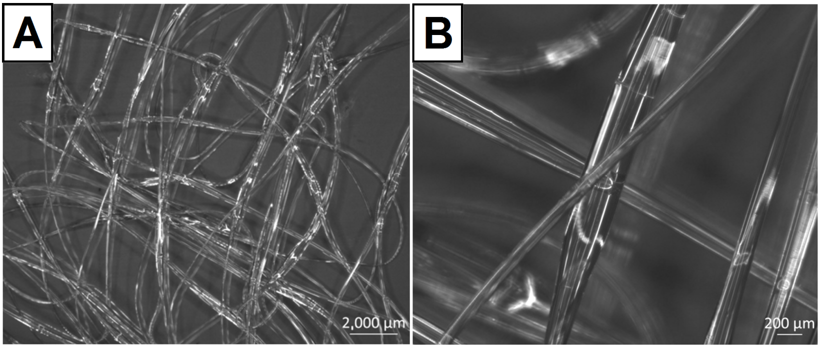

Figure 32: Microscopy images of a non-regular PEtOx deposition. A) Overview image and B) Close-up view. The scaffold exhibited highly non-regular diameters and a highly defective structure although square grids have been chosen for collector movement. T = 210 °C, p = 3.0 bar, U = 5.0 kV, h = 5.0 mm, 23 G spinneret, s_c = 200 mm·min^{-1}.[136]
(Published under Creative Commons licence CC BY-NC-ND 3.0)

While several different instrumental parameter combinations led to poor deposition qualities, a completely different deposition behaviour of PEtOx compared to PCL could be observed. Here, the polymer jet did not tend to stack up on top of already deposited fibres at all, indicating a strong Coulomb repulsion of residual charges onto or in the material.

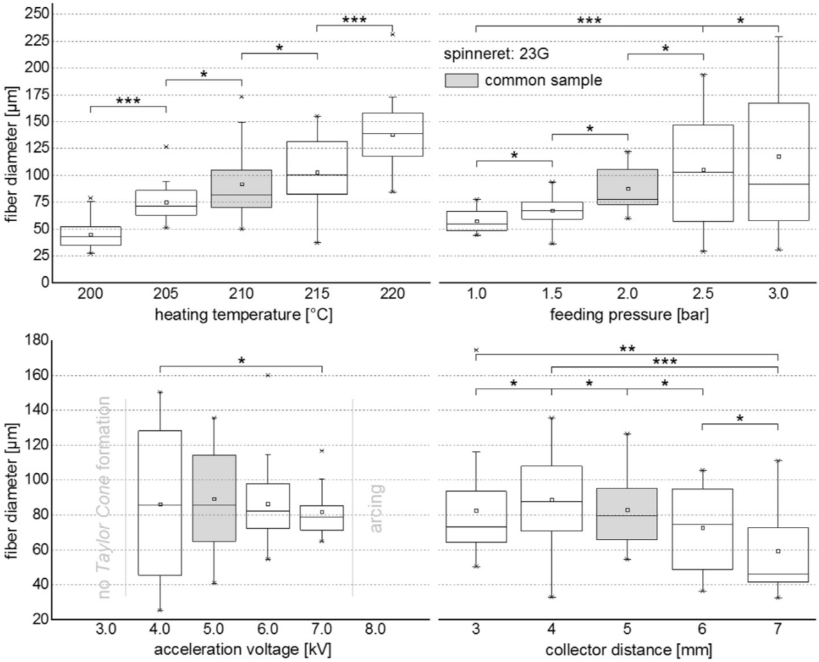

*Figure 33: Fibre diameters of PEtOx as function of different instrumental parameters A 23 G spinneret was utilised. While an increasing heating temperature and feeding pressure clearly led to thicker fibre diameters, a low acceleration voltage led to pulsed and beaded fibres at constant average values. In contrast to this, the fibre diameter decreased at steady average values at increasing distances between spinneret and collector surface. A 23 G spinneret was utilised. * non-significant / ** p < 0.05 / *** p < 0.01 according to analysis of variance.[136] (Published under Creative Commons licence CC BY-NC-ND 3.0)*

Further, *pulsing* and *long beading* seemed to influence the MEW manufacturing of PEtOx, reflected by the observed oscillation of the fibre diameters during printing at high feeding pressures and low acceleration voltages. Here, the largest errors were observed using a 23 G spinneret providing the largest inner diameter for the presented MEW experiments (Figure 33).

The most prominent change in the average fibre diameter from fØ = 45 ± 14 µm to fØ = 138 ± 33 µm was observed by changing the heating temperature from T = 200 °C to T = 220 °C. This can be ascribed to the decreasing viscosity at higher temperatures and the resulting material flow through the spinneret at constant feeding pressures assessed by to the Hagen-Poiseuille equation *(1)* presented and discussed on page 18. Here, a standard rheological investigation is not applicable due to the inappropriate testing conditions. For a deepened understanding of MEW, an HV charged fibre rheometer should be constructed and utilised for future work. Based on the observed solidification of the polymeric jet before the deposition on the collector, a round fibre profile can be assumed. Hence, the fibre cross-section increases about one order of magnitude potentially accompany huge changes in performance properties of resulting scaffolds.

Indeed, an increasing feeding pressure from p = 1.0 bar to p = 3.0 bar raised the polymer mass flow dm_1/dt and the fibre diameter significantly from fØ = 55 ± 10 µm to fØ = 118 ± 83 µm, nevertheless, the change in SD is even more remarkable. Taking the acceleration voltage's influence on fibre homogeneity with U = 4.0 kV resulting in fØ = 86 ± 42 µm and U = 7.0 kV leading to fØ = 82 ± 14 µm at similar CTS values into account, *pulsing* and *long beading* instabilities analogously to PCL can be inferred. This conclusion seems to be consistent with collected imaging data and visible observations during MEW printing.

Further, the spinning distance was investigated as additional instrument parameter determining the electrical field strength and the acceleration path of the jet. Although no significant changes could be observed by changing the distance from h = 3.0 mm to h = 5.0 mm with corresponding fibre diameters of fØ = 83 ± 28 µm to fØ = 82 ± 22 µm, significant fibre diameter reductions resulted at h = 7.0 mm with fØ = 60 ± 27 µm.

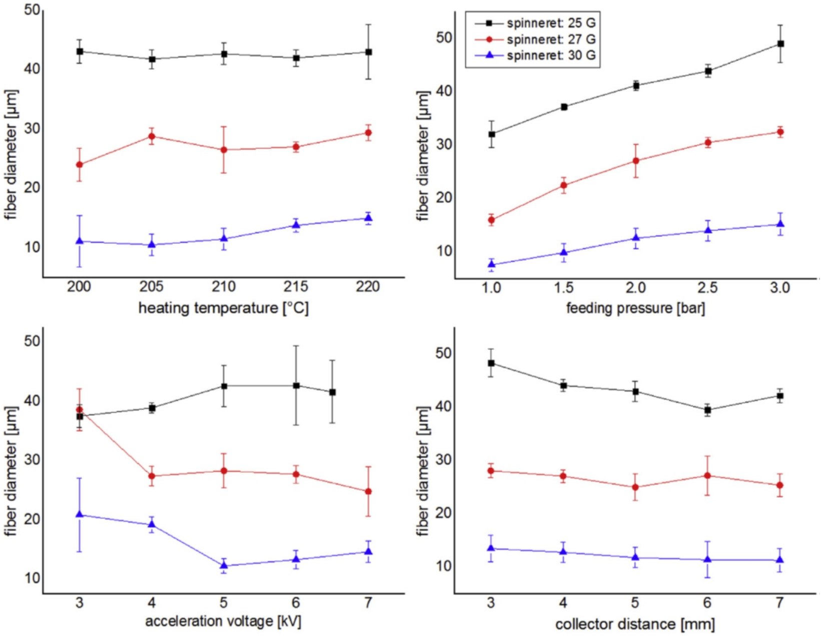

Figure 34: Fibre diameters of PEtOx as function of different instrumental parameters. 25 G, 27 G and 30 G spinnerets were utilised. With increasing heating temperatures and feeding pressures, resulting fibre diameters decreased tendentially. While the influence of acceleration voltage did not result in a clear trend, an increasing distance between spinneret and collector led to reduced fibre diameters.[136]
(Published under Creative Commons licence CC BY-NC-ND 3.0)

Even though, the electrical field strength diminishes dramatically from $E = 1.7\ \mathrm{kVmm}^{-1}$ at h = 3.0 mm to $E = 0.7\ \mathrm{kVmm}^{-1}$ at h = 7.0 mm, the acceleration path of the jet from the spinneret to the collector was apparently more essential for stretching and flowing processes in the electrified polymer melt under chosen conditions.

As reflected by the correlation functions in Figure 34, observed dependencies between instrumental parameters and the average fibre diameter for a 23 G spinneret can be confirmed using 25 G, 27 G and 30 G spinnerets. However, some of the functions show inconclusive trends indicating an unstable and complex, time-dependent behaviour. Especially for the acceleration voltage alternation, stabilisation times seemed to be very important as t = 10 min was not enough time for dynamic balancing between two single printing arrays for fibre diameter quantification. Here, the pressure was the most suitable and reliable tool to influence the fibre diameter quickly during MEW printing in a broadly adjustable range.

In total, vastly different PEtOx fibre diameters were deposited using suitable printing conditions to avoid at least *long beading* ranging from fØ = 8 ± 1 µm (*stable*) with a 30 G spinneret at p = 1.0 bar and T = 210 °C to a fibre diameter of fØ = 138 ± 33 µm (*pulsed*) utilising a 23 G spinneret at p = 2.0 bar and T = 220 °C. By transferring the gathered insights about stable processing into scaffold manufacturing, highly porous and almost regular structures can be printed (Figure 35). Nevertheless, not even a single fibre stack could be observed. This phenomenon took place during every single PEtOx processing experiment and seems to be independent from utilised instrumental parameters at the first glance. In order to assess material based charging and storage behaviour during MEW, further experiments need to be conducted.

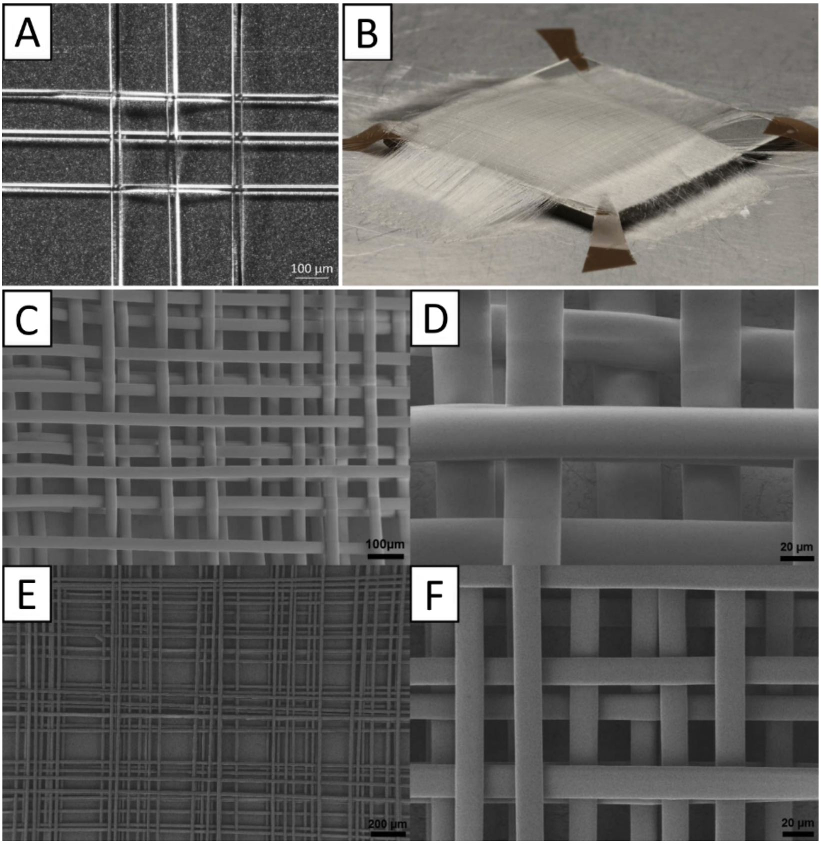

Figure 35: Images of PEtOx scaffolds.A) Microscopy image of deposited fibres using stable printing conditions at $T = 210$ °C, $p = 1.5$ bar, $U = 3.0$ kV, $h = 4.0$ mm, 27 G spinneret, $s_c = 400$ mm·min^{-1}. B) Photographical image of a square scaffold with 180 fibre layers, 2 mm thickness and 10 mm edge length. Printed at $T = 210$ °C, $p = 2.0$ bar, $U = 4.0$ kV, $h = 5.0$ mm, 30 G spinneret and $s_c = 400$ mm·min^{-1}. C-F) SEM images of scaffolds printed at $T = 210$ °C, $p = 2.0$ bar, $U = 4.0$ kV, $h = 5.0$ mm, $s_c = 400$ mm·min^{-1}. C&D) 27 G spinneret, E&F) 30 G spinneret. Even under stable printing conditions with programmed square grid structures, no fibre stacking could be observed.[136]
(C-F: Image by Dr. Vladimir Stepanenko, published under Creative Commons licence CC BY-NC-ND 3.0)

Furthermore, PEtOx seemed to fully solidify on the way to the collector or at least exhibited immobilised macromolecules due to quenching since the fibres lacked of adhesion between the deposited layers leading to delamination. A suitable way to overcome this issue for lab handling was to use the present humidity in air in combination with the hygroscopic material properties of PEtOx at room temperature or below LCST in detail. Consequently, the increasing water content plastified the amorphous material easily and mobilised molecular chains. As a result, fibre fusion occurred driven by gravity, surface area minimisation and randomised molecular entanglement. This enables the application of thermosensitive and water-soluble biocompatible polymers as sacrificial template with tailorable fibre and pores sizes.

3.4 Conclusion

Understanding the MEW processing behaviour including the influencing instrumental parameters is essential in order to deposit molten polymeric jets to precisely defined and reproducible scaffolds. In the presented chapter PCL and PEtOx were investigated regarding stable printing conditions including fibre diameters and placement quality on the collector surface.

Both polymers exhibited the same processing characteristics regarding *pulsing* and *long beading*, two fibre diameter instabilities leading to defectively printed structures. In this context, *long beading* can be understood as exaggerated manifestation of *pulsing*, a periodical oscillation of the fibre diameter accompanied by changes in CTS. A hypothesis was introduced explaining the origin by spending attention to the involved mass flows during processing. This further helps to overcome these printing issues by balancing the instrumental parameters for resulting force or momentum equilibria resulting in stable jet behaviour.

Thereby, limiting the applied feeding pressure in combination with a high acceleration voltage below the breakdown limit turned out as an efficient way for manufacturing high quality structures. Furthermore, several parameter combinations at a fixed spinneret size led to a broadly adjustable fibre diameter spectrum enabling a very high design freedom during AM. This can be understood as an essential step towards successful processing of gradient and zonal structures. Nor the AM process FDM, neither the EHD technique ES exhibit an equivalent performance, making MEW a reasonable choice to manufacture complex fibre constructs.

Nevertheless, MEW is barely investigated from a physical and technical point of view, necessitating studies regarding charge storage and dissipation of the melt jet and fibres for an optimised stacking and processing behaviour for instance. Furthermore, advanced electro-rheological characterisation techniques could help to identify proper MEW materials and allow to estimate the resulting flow behaviour in the HV field.

4 Ultrafine fibres

Parts of this chapter have already been published in the following article:

Gernot Hochleitner, Tomasz Jüngst, Toby D. Brown, Kathrin Hahn, Claus Moseke, Franz Jakob, Paul D. Dalton and Jürgen Groll

„Additive manufacturing of scaffolds with sub-micron filaments via melt electrospinning writing"

Biofabrication 2015, DOI:10.1088/1758-5090/7/3/035002

Presented experiments, data evaluations and writing were accomplished independently if not clearly stated otherwise.

4.1 Introduction

Although MEW is a promising method for scaffold fabrication, printed structures shown in literature lack of a suitable resolution so far. While the common ES technology enables spinning of non-woven meshes with PCL fibre diameters mainly in submicron- to microscale[265-268], thinnest PCL fibres processed via MEW have not been smaller than 5 µm until now.[107] Besides several applications including catalysts[269], micro-electro-mechanical systems[270], sensors[271], energy storage and conversion[272], filters[273] or membranes[274], also TE can benefit from AM printed structures at high resolutions with high specific surfaces and high aspect ratios[275].

To achieve such desired small fibre diameters by MEW, processing parameters were adjusted purposefully. This approach contains the combination of the three key parameters: a high electrical field strength, a low flow rate and a small spinneret size. Considering the gathered processing knowledge about stable printing in chapter **Fibre pulsing during MEW**, submicron fibres with fØ = 817 ± 165 nm were printed successfully to accurate square grid scaffolds with mesh widths of L = 100.6 ± 5.1 µm and a total of 100 layers that stacked precisely on top of each other.

In order to analyse resulting fibre and scaffold morphologies, different analytical methods have been used. In addition to SEM measurements for optical structure evaluation, x-ray diffraction (XRD) and differential scanning calorimetry (DSC) were performed to investigate the resulting crystalline structure of the fibrous PCL. Furthermore, topographical analysis was conducted using scanning force microscopy (SFM) revealing a molecular alignment induced by stretching and quenching effects during MEW manufacturing.

To understand the resulting thermodynamical state of the printed fibres, scaffolds samples were analysed directly after MEW processing and additionally after a subsequent thermal aging process below the melting point at T = 55 °C. The results indicated an incomplete crystallisation exhibiting a certain re-crystallisation potential that could change the performance properties of fabricated scaffolds during application.

The printed submicron fibre scaffolds revealed a low mechanical stability and therefore, an insufficient lab usability. To overcome this issues, a MEW printing approach directly on glass slides coated with a reactive surface based on star-shaped polyethylenoxide-*stat*-polypropylenoxide macromers with water-cross-linkable isocyanate end groups [NCO-sP(EO-*stat*-PO)] was used. In addition, this system enabled a super-hydrophilisation of the slide surface acting as cell repellent substrate via suppression of non-specific protein adsorption[276]. The deposited PCL fibres adhered well to the modified glass slides and the sensitive scaffold structure could be maintained thereby. No structural changes were observed even after washing steps and media changes of 10 days *in vitro*. These experiments were conducted utilising human mesenchymal stem cell (hMSC) seeding revealing proper cell adhesion on the fibres and between the fibre walls.

4.2 Experimental section

4.2.1 Polymer

PCL was purchased from Sigma-Aldrich Co. LLC. (CAS# 24980-41-4, St. Louis, USA) and used as received. The molecular weight and polydispersity of the raw material was investigated by Björn Schulte from the Department of Macro-molecular Chemistry, RWTH Aachen University via size exclusion chromate-graphy (SEC, detector: Jasco, RI 2031 plus) using trichloromethane as eluate.

Further, the viscoelastic properties of PCL were analysed by oscillation rheometry (MCR 301, Anton Paar, Ostfildern-Scharnhausen, Germany) with a plate diameter of 20 mm, plate-to-plate distance of 1 mm at deformations of 20 % and 10 rads^{-1} ranging from 80 to 130 °C with an increasing temperature rate of 0.025 °Cs^{-1}.

4.2.2 MEW device

For MEW printing a custom-built MEW device was used analogously as already introduced in **High-temperature device** shown on page 55f.

4.2.3 Manufacturing conditions

A systematic adjustment of the instrumental parameters was conducted similar to chapter **Fibre pulsing during MEW** on page 51ff. Thereby, fibre diameter and printing instabilities were taken into account. For fibre diameter minimisation and an optimised structural resolution, the temperature was varied from a heating temperature of $T = 80$ °C to $T = 120$ °C, the feeding pressure from $p = 0.5$ bar to $p = 4.0$ bar, the acceleration voltage from $U = 2.0$ kV to $U = 10.0$ kV, the spinning distance from $h = 1$ to 10 mm using 23 G, 25 G, 27 G, 30 G and 33 G spinnerets and collector speeds between $s_c = 1000$ and 9000 mm·min^{-1}.

The optimum results are presented in the discussion following the systematical trends as provided in chapter **MEW processing investigation with PCL** on page 60ff and the literature as reflected in the **State-of-the-art** chapter in the **Instrumental parameters** section on page 32ff.

The presented investigations were conducted at room temperature 21 ± 2 °C and an environmental humidity of 35 ± 15 % r.h. Measured values contain the standard deviation of a sample (SD), as already introduced on page 58.

4.2.4 G-code programming

Common square grid shaped scaffolds with L = 100 µm mesh width were programmed containing 50 layers in 0° and 50 layers in 90° direction, hence a total of 100 fibre layers. Used square scaffolds in this study exhibited an edge length of 15 mm, the corresponding G-code is presented in the supplementary information on page xxix.

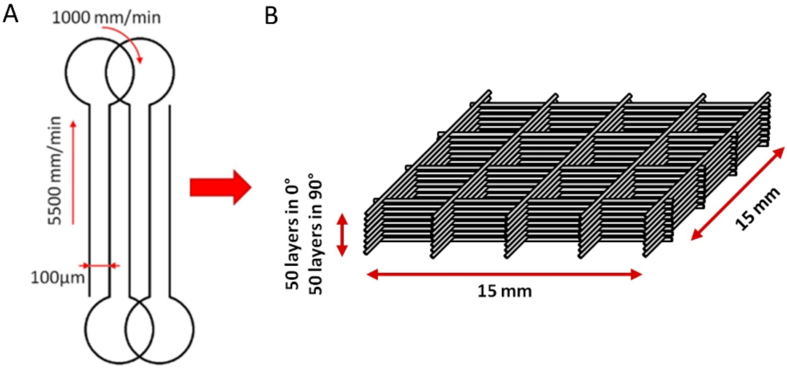

Figure 36: Schematic of the programmed G-code deposition path. A) Turning loops at the scaffold edges for optimisation of the printing quality. B) Illustration of the printing geometry.[129] (Published under Creative Commons licence CC BY 3.0)

To optimise the fibre deposition behaviour, the turning loops at the scaffold edges were implemented as presented in Figure 36. Here, the axes speed of s_c = 1000 mm·min^{-1} helped to avoid excessive material stacking and resulting additional structural defects.

Uniaxial fibre samples were manufactured for morphological investigations using similar processing conditions as the presented ones except the difference of aligned deposition direction (0° only, no 90° fibres). In addition, random coiled fibre scaffolds were fabricated by reduction of the collector speed to

s_c = 800 mm·min^{-1} as reference structures. Single layer structures were printed for SFM measurements.

4.2.5 Instrumental analysis of scaffolds

Fibre diameter and scaffold mesh width quantification was performed using a SEM (Supra 25, Carl Zeiss AG, Oberkochen, Germany) at a distance of 15 mm and an acceleration voltage of 5 kV. The samples were sputtered-coated using gold. In order to get significant high numbers, n = 50 fibre diameters in 0° and 90° direction were measured as well as n = 100 mesh widths correspondingly.

For submicron fibre topography analysis SFM (FlexAFM, Nanosurf, Langen, Germany) was performed using n = 5 line surface roughness of 5 µm distances on uncoated single fibres.

To determine the crystalline fibre morphology, XRD (D5005, Siemens, Berlin, Germany) measurements were conducted via Bragg-Brentano geometry and Cu–Kα radiation (λ = 0.15418 nm) at a voltage of 40 kV and a tube current of 40 mA at grid scaffolds, uniaxial aligned samples, randomised meshes and molten films (aged at T = 85 °C for t = 30 min) derived from investigated scaffolds for comparison. A scan rate of t = 8 s per Θ = 0.02° step was executed in the 2Θ range between 10° and 60° (total time of a single measurement t = 5.6 h). Furthermore, uniaxial samples were irradiated at tilted angles of 0°, 30° and 60° in planar directions to investigate a potential molecule alignment along the fibre axes. To assure methodical reliability and result constancy one uniaxial aligned sample was investigated three times.

Characterisation of the glass transition temperature T_g, the melting point T_m and the specific thermal energy ω was performed by DSC (204 F1 Phoenix, Netzsch, Selb, Germany), thereby granulated raw material with m = 6.13 mg was compared to a scaffold sample with m = 6.26 mg. Heat flow scans were conducted using a rate of 10 $Kmin^{-1}$ or respectively -10 $Kmin^{-1}$. The samples were heated and cooled twice from T = -120 °C up to T = 90 °C. Furthermore, a slow DSC measurement with 2 $Kmin^{-1}$ heating rate was performed for comparison.

Additional experiments of heat-treated PCL scaffolds (at T = 55 °C below the melting temperature onset for t = 18 h) were executed with AFM and XRD to investigate the difference in the morphology of the samples directly after MEW deposition and under thermally aged conditions.

4.2.6 Substrate coating

The following surface coating of the glass slides (Starfrost®, Waldemar Knittel Glasbearbeitungs GmbH, Braunschweig, Germany) was performed based on [277] and following a standard operation procedure (SOP, provided in the supplementary information on page xxxii as german text) available at the Department for functional materials in medicine and dentistry, University Hospital of Würzburg.

In brief, glass slides were cleaned via ultrasonic bath (with acetone, H_2O and isopropanol, each t = 10 min), etched using a mixture of H_2O_2:H_2SO_4 at 1:2 volume ratio and cleaned again (ultrapure H_2O, specific electrical resistance $\rho_{el} \geq 17$ MΩcm and a total organic content TOC ≤ 9 ppb at RT). Afterwards 3-Aminopropyl-trimethoxysilan was evaporated via vacuum in a desiccator, physically deposited on the glass slides thereby and covalently bound via hydrolysis-condensation reaction using humidity of the surrounding air finally. As last step, six-armed (M = 2 $kgmol^{-1}$ each arm) NCO-sP(EO-*stat*-PO) macromeres with 80 mol.% EO and 20 mol.% PO were solved in tetrahydrofuran and water, THF:H_2O at 1:9 volume ratio and deposited on the pretreated glass slides via spin coater (WS-650MZ-23NPP, Laurell Technologies Corporation, North Wales, USA). As result of reaction processes with amines from the surface and cross-linking between the star-macromeres via water, nanometer-sized coatings remained on the glass slides with super-hydrophilic wetting properties (Figure 37).

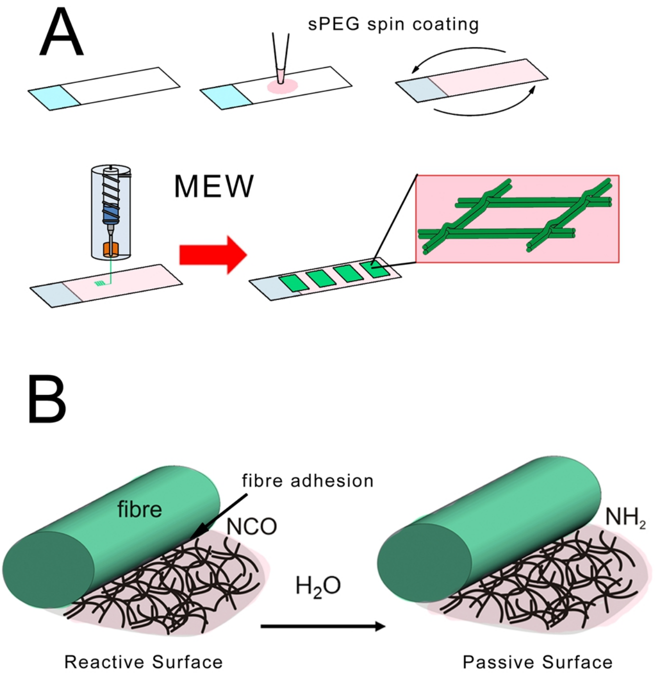

Figure 37: Illustration of spin-coating and MEW processing onto glass slide collectors. A) A solution of NCO-sP(EO-stat-PO) in THF and water was deposited onto the glass slide and homogenously distributed via rotational spin coating. Directly afterwards, MEW printing was performed onto the coated slides. B) The active NCO-groups cross-linked with aid of water and formed a super-hydrophilic surface.[129]
(Image by Prof. Dr. Paul D. Dalton, published under Creative Commons licence CC BY 3.0)

The MEW printing of submicron fibre scaffolds onto the coated glass slides was performed directly after preparation of the coating.

4.2.7 Cell adhesion experiments

The presented biological experiments were conducted by Kathrin Hahn, however, the preparation and results are presented in this chapter in order to maintain integrity of the study.

To investigate the adhesion behaviour, hMSCs were derived from the trabecular bone isolated from a femoral head of a patient who underwent total hip arthroplasty.[278] For cell cultivation DMEM/Ham's F-12 with GlutaMAX™-I medium added with 10 vol.% fetal calf serum, 100 Uml^{-1} penicillin, 100 mgml^{-1} streptomycin (all purchased from Gibco® Life Technologies, Thermo Fisher Scientific Inc., Massachusetts, USA) and 50 µgml^{-1} L-ascorbic acid 2-phosphate (Sigma-Aldrich, St. Louis, USA) were used. A cell seeding density of 3.1×10^4 cm^{-2} was utilised and samples were incubated at T = 37 °C / 98 % r.h. with 5% CO_2 for 10 days *in vitro* (DIV). Scaffolds with mesh widths of 90 µm and 150 µm were deposited onto the introduced glass slides coatings with cell repellent properties [276, 279] and sterilised using UV light (t = 30 min each side, at 254 nm with 1 mWcm^{-2}). Resulting cell constructs were fixed utilising 4 wt.% paraformaldehyde, permeabilised with 0.2 vol.% triton-X 100 and stained afterwards with phalloidin, tetramethylrhodamine B isothiocyanate (Sigma-Aldrich, St. Louis, USA) and Hoechst 33342, trihydrochloride trihydrate (Molecular Probes, Life Technologies GmbH, Darmstadt, Germany) according to given instructions.

For optical evaluation, inverse fluorescence microscopy (Axio Observer.Z1 with ApoTome.2, Carl Zeiss AG, Oberkochen, Germany) with z-stack function was conducted with the Zeiss software ZEN pro 2012. Images were prepared using ImageJ (version 1.49k, open source, NIH).

4.3 Results and discussion

4.3.1 Materials properties

The used PCL, composed of linear macromolecules, exhibited a relatively small molecular weight M_w = 83 kgmol^{-1} with a broad polydispersity Đ = 2.4 leading to suitable flow characteristics. As shown via oscillation rheometry in Figure 38, the loss factor tanδ increased vastly with an increasing temperature. Even at lower melt temperatures of measured T = 84 °C (analogously to MEW heating temperature T = 109 °C in this chapter) the loss modulus G'' = 1.1 x 10^4 Pa dominated the storage modulus G' = 9.6 x 10^2 Pa leading to a loss factor of tanδ = 11.4.

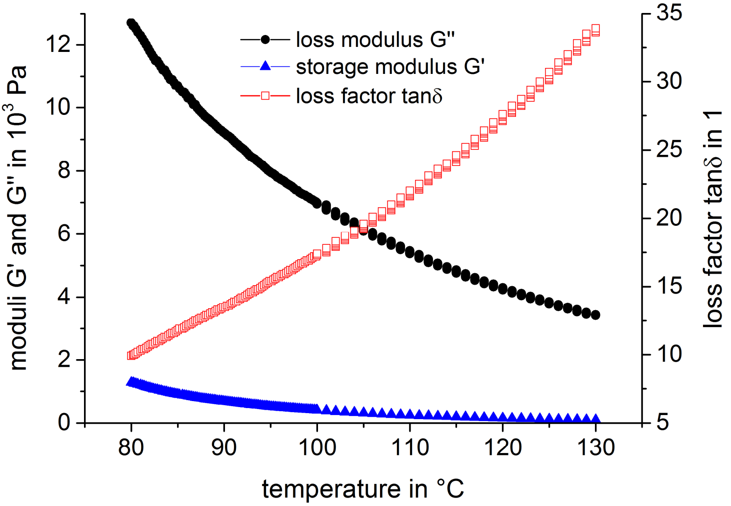

Figure 38: Viscoelasticity of the PCL melt as function of the temperature. The loss and storage modulus decreased significantly at increasing temperatures from T = 80 to 130 °C, accompanied by a raising loss factor.[129]
(Published under Creative Commons licence CC BY 3.0)

As result, the viscous behaviour was more prominent than elastic characteristics indicating proper plasticity for melt jet acceleration and stretching processes. However, neither a quantitative conclusion, nor a clear physical prediction for resulting fibres could be inferred from this collected data and the published studies so far.

4.3.2 MEW printing of small structures

Similarly to studies on PURASORB PC12 provided in the previous chapter, the MEW process of the used PCL from Sigma-Aldrich Co. LLC in this study led to defectively printed structures at several different instrumental parameter combinations in the investigated range ($T = 80$ to 120 °C, $p = 0.5$ to 4.0 bar, $U = 2.0$ to 10.0 kV, $h = 1$ to 10 mm using 23 G, 25 G, 27 G, 30 G and 33 G spinnerets at $s_c = 1000$ to 9000 mm·min^{-1}), as shown by Figure 39.

Observed *pulsing* or *long beading* phenomena did last for several seconds or minutes with fibre diameter oscillation frequencies of 0.1 to 0.01 Hz. While these instabilities are undesired as explained in chapter **Fibre pulsing during MEW** on page 51ff, the printed structures revealed fibre diameters in the nanometer range $f\varnothing \leq 100$ nm as well, confirming the general opportunity to fabricate PCL nano-fibres by MEW.

As presented in Figure 39 C&D, the resulting scaffold height is locally different due to elevated fibre stacking at intersections and fibre sagging in between. In some cases, progressively growing structural defects near to the intersections could be observed. Such broken fibres that led to gaps in the fibre walls can be ascribed to an interaction of different circumstances. First of all, the deposited fibres are exposed to gravitationally and electrostatically induced pulling forces at and between the elevated intersection bearings. Thereby, the bending momentum increased incrementally with stacking height and bearing distance owing to basic mechanical considerations[280]. These underlying geometrical conditions shall result in increasing tensile stresses into the printed fibres with increasing sagging consequently.

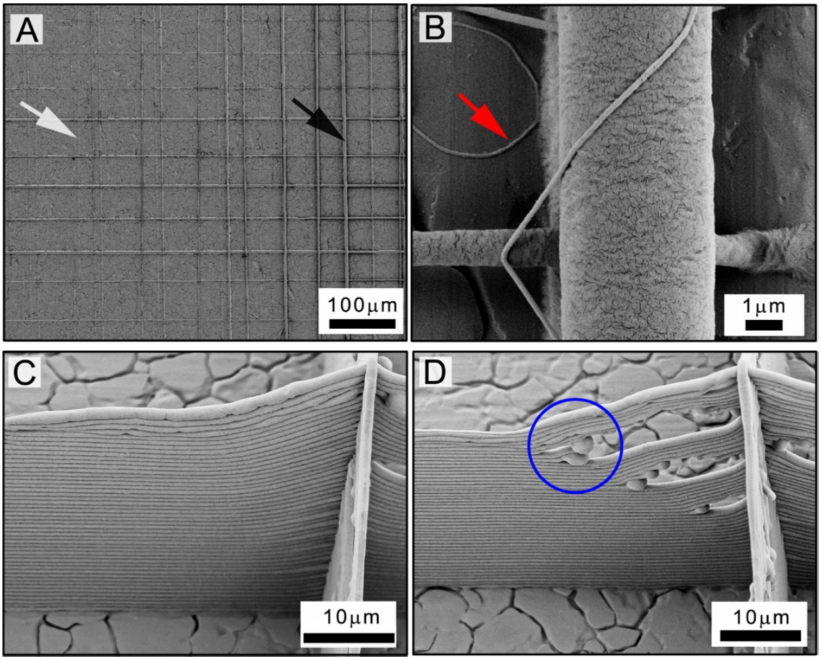

Figure 39: SEM images of a defective sample. A&B) Long beaded fibres, the white arrow points at a thin, the black arrow at a thick fibre. The red arrow elucidates the contrast between low diameter fibres in the nanometer range that exceeded CTS and the relatively high diameter fibre in the micrometer range. C&D) Several instrumental parameter combinations led to defective scaffold structures. Due to the stacking at fibre intersections and fibre sagging between, resulting scaffolds have shown locally different heights. In some cases, broken fibres in almost regular distances occurred, leading to gaps in the structure.[129]
(Image by Dr. Claus Moseke, published under Creative Commons licence CC BY 3.0)

In Figure 39 D, the macromolecules of the partially solidified fibres seemed to be mobile enough for flow processes driven by mechanical stress relaxation enabled by the thermal conditions. This assumption is supported by the spherical ending of broken fibres as result of a partially molten polymer state. Indeed, flow induced crystallization may occur in the MEW jets in general leading to quick solidification. However, thermal aging of deposited fibres could also lead to increased molecular mobility and flow processes in the scaffolds facilitated by internal mechanical stresses ultimately.

At instrumental parameters of: heating temperature T = 109 °C (corresponds with melt temperature T = 84 °C), feeding pressure p = 2.8 bar, acceleration voltage U = 2.9 kV, spinning distance h = 1.5 mm, 33 G spinneret size and collector speed s_c = 5500 mm·min^{-1}; optimised printing conditions were observed. Resulting scaffold structures are reflected in Figure 40. Shown scaffolds exhibited submicron sized fibres with fØ = 817 ± 165 nm and mesh width with 100.6 ± 5.1 µm at 100 layers, 50 in both 0° and 90° direction. As visible in Figure 40 A, the scaffold structure varied significantly in different zones. At the turning edges the collector movement slowed down necessarily due to changes in printing direction. Here, coiling was observed as result of $s_c \ll$ CTS.

After the turning procedure, the axes started to accelerate again with finally $s_c \geq$ CTS and accurately deposited linear fibre walls in the middle of the scaffold. However, during acceleration of the collector the fibres were printed to poorly stacked and non-linear structures forming an opaque zone. Directly afterwards, a transition zone from a hazy structure towards linear fibres with laterally shifted fibre walls was observed. The shown structural defects are a result of technical limitations (acceleration ≈ 1 ms^{-2}), the utilisation of axes with strongly increased acceleration capacities would most probably reduce the area of hazy zone significantly.

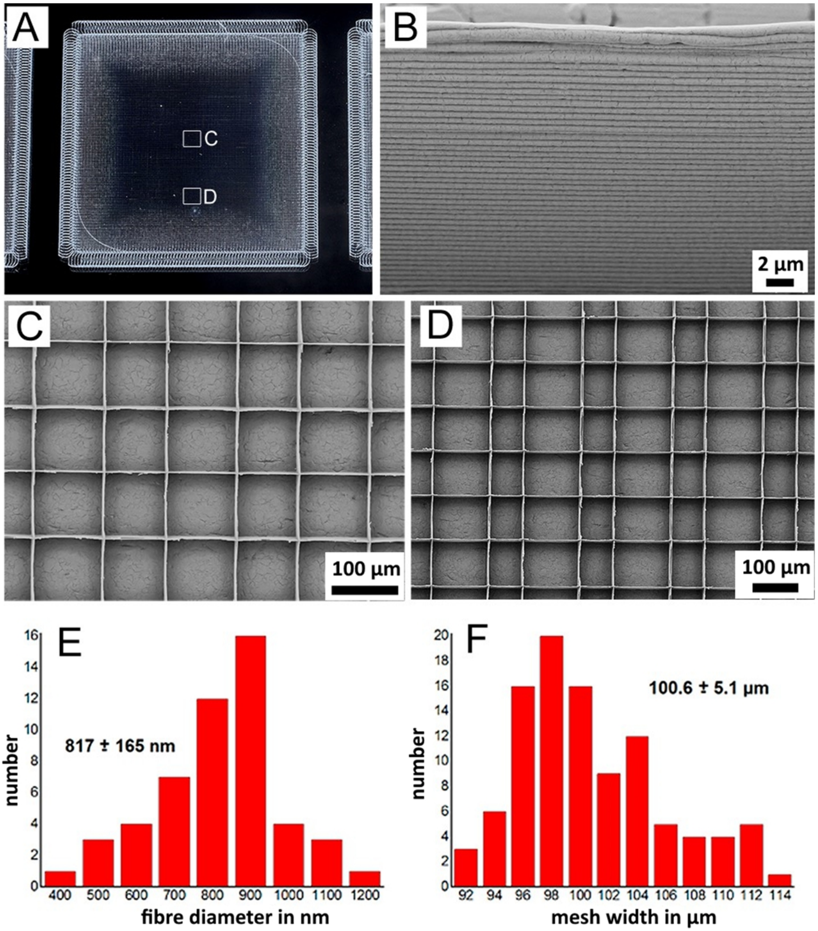

Figure 40: Scaffolds with submicron sized fibre diameters at optimised instrumental parameter conditions. A) Photographical overview image of a scaffold exhibiting different zones. The hazy structure at the turning edges became more and more defined towards the middle zone with high quality resolution. B) SEM image of an accurately stacked 50 layers fibre wall. C) SEM image of the high quality structure of the scaffold's middle zone. D) Closer to the turning loops, laterally shifted fibre walls can be observed leading to irregular mesh widths. E&F) fibre diameter and mesh width quantification via SEM.[129]
(B-D: Image by Dr. Claus Moseke, published under Creative Commons licence CC BY 3.0)

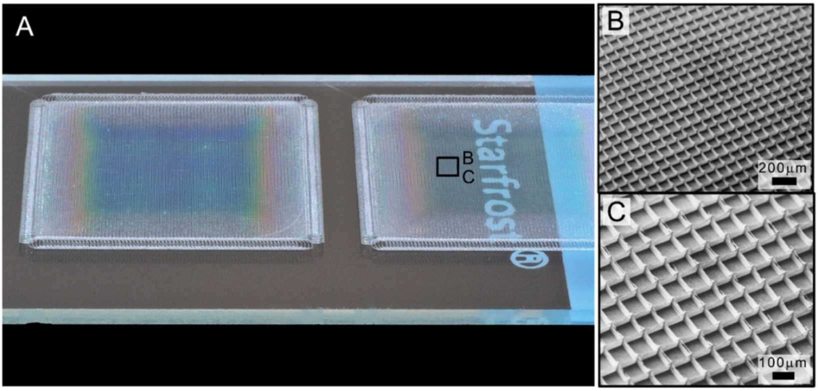

Figure 41: Images of submicron sized fibre scaffolds presented at tilted angles. A) Photographical overview picture shows the interaction between the fibres of the box structure and the incident light. While the middle zone exhibited a homogeneous colouring, the transition zone appeared from red to yellow or green. The hazy zone near the edges in contrast, was whitish in consequence of prominent scattering effects at the poorly defined structure. B&C) SEM images of the regular middle zone at 30° tilted camera angle.[129]
(Published under Creative Commons licence CC BY 3.0)

The homogeneity of the box structured scaffolds printed at optimised conditions is clearly visible at tilted angles as presented in Figure 41. While the poorly structured hazy zone near the edges appears to be whitish, the transition zone appears from red to yellow and green. The homogeneous middle zone of the scaffold is regularly blue in contrast. The colouring may be the result of a specific interaction between the PCL fibres with the incident light, however, the optical uniformity indicates regular fibre deposition in the large middle zone and therefore helps to assess the printing quality at the first glance.

4.3.3 Morphological analysis of printed structures

By taking into account the known molecular alignment effects during common MS[281, 282] or ES[283, 284] of linear thermoplastic polymers, similar macromolecular alignment processes can be expected during MEW as well. Due to the vast EHD-driven jet acceleration and quenching, PCL molecules may orient along the jet rotation axis and crystallise anisotropically.

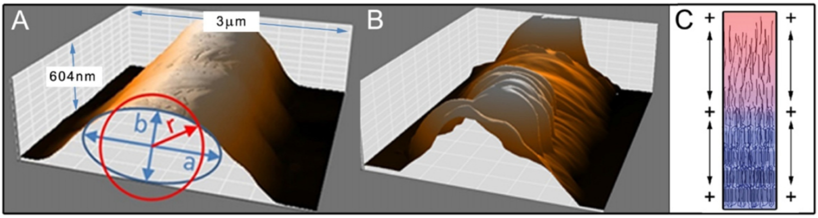

Figure 42: SFM characterisation of printed mono-layers. A) Fibres exhibited a smooth surface after MEW processing. B) Induced by thermal aging below the melting temperature onset, crystalline lamellas formed perpendicularly aligned along the fibre direction. C) Schematic of molecular alignment and solidification in the jet during MEW.[129]
(C: Image by Prof. Dr. Paul D. Dalton, published under Creative Commons licence CC BY 3.0)

Figure 42 shows the change of SFM characterised fibres before and after a thermal aging treatment below the melting temperature onset at T = 55 °C for t = 18 h. Directly after deposition, the resulting surface was smooth, as the presented SEM pictures indicate. Here, the fibres exhibited an average surface roughness of $R_a = 23 \pm 3$ nm and a root mean square roughness of $R_q = 28 \pm 4$ nm.

After thermal treatment, lamellas formed perpendicular to the printing direction with $R_a = 134 \pm 36$ nm or $R_q = 153 \pm 31$ nm respectively. This SFM measurement confirmed the assumption of aligned macromolecules during MEW printing under chosen conditions on the one hand. On the other hand the analysis proved the submicron sized fibre diameters. A roughly elliptic cross-sectional fit with the half-axes a = 0.5 x 1.3 µm and b = 0.5 x 0.6 µm was necessary to estimate the shape and area ($A = 0.7\ \mu m^2$). Due to PCL flow processes of remaining molten material content or amorphous regions in fibres after deposition, no circular shape could be observed. In addition, the inability of the

SFM needle to measure space underneath deposited structures or overhangs could not be taken into account. However, the fibre diameter and cross-section complied with a circular profile of approximately fØ = 0.9 µm.

Further, the comparison of the non-treated fibres with the thermally aged ones revealed the high potential for plastic deformation after MEW processing. If such morphological changes occur kinetically fast during TE applications at T ≈ 37 °C is unclear and must be investigated, however, changes in mechanical properties and cell-response due to scaffold deformation should be considered.

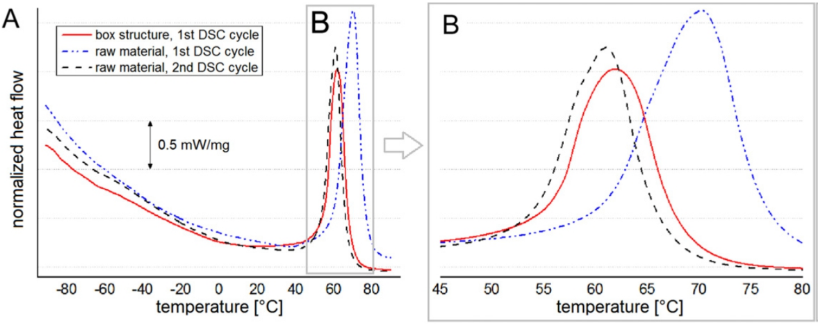

Figure 43: DSC plot of PCL box structure scaffolds and raw material. A) Melting peaks as comparison between the submicron sized fibrous scaffold and the corresponding granulated raw material. The box structured scaffolds exhibited a lower melting temperature and a lower amount of specific thermal energy for melting, however, the second heating cycle of the raw material was relatively similar to the first cycle of the box scaffolds. B) Close-up view of the melting peaks.[129]
(Published under Creative Commons licence CC BY 3.0)

In order to compare the melting temperature and specific thermal energy stored in the crystalline regions of the PCL fibres from box structured scaffolds, a comparison via DSC with cut raw material granules was conducted (Figure 43). Here, the integration of the heat flow at increasing temperatures revealed a specific thermal energy of ω_{box} = 125 Jg^{-1} compared to the approximately 30 %

increased one of the raw material with ω_{raw} = 171 Jg^{-1}. While the raw material exhibited a relatively low specific surface and a different thermodynamic state, the prominent quenching effect of the PCL fibres during MEW could be observed. As revealed by SFM and SEM measurements, the crystal size of the fibres must be obviously smaller than the corresponding submicron fibre diameter. As known from literature, materials exhibiting a high number of small crystals show reduced melting temperatures and peak integrals compared to materials with few large crystals.[285]

The reason for this behaviour can be found by spending attention to the ratio between the surface and the bulk energy level of crystalline structures. If the radius of a (simplified spherical) crystal r_{cry} overcomes a critical value and further grows, the volume free energy decreases proportional to r_{cry}^3 while the counteracting surface energy increases proportional to r_{cry}^2 only.[286] Hence, it can be assumed that the raw PCL exhibited large crystalline regions, while the submicron fibre diameter acted as a boundary for crystalline growth. Further to the specific thermal energy, the melting onset temperature T_{mo} = 60.6 °C and melting peak temperature T_{mp} = 70.2 °C of the raw material were significantly higher compared to the box structure scaffolds with T_{mo} = 55.5 °C and T_{mp} = 62.0 °C. This may be the result of an extremely high specific jet and fibre surface enabling a high quenching rate.

However, tested raw material and scaffold samples showed relatively similar thermal properties in the second heating cycle defined by a fixed cooling rate of -10 Kmin^{-1}. Here, the crystalline structure may not be fully developed since the raw material’s specific thermal energy level of the first cycle was significantly higher.

In order to prove the influence of the heating rate, additional investigations with 2 Kmin^{-1} have been conducted. Here, with a melting onset temperature of T_{mo} = 59.8 °C for raw material and T_{mo} = 56.1 °C for box scaffolds, the differences were reduced but still considerable. The comparison of the specific heating energy yielded similar results, the peak integral of the raw material was slightly increased (15 %) with ω_{raw} = 175 Jg^{-1} in contrast to the of the box scaffold with ω_{box} = 148 Jg^{-1}.

Further, the glass transition temperature indicated thermodynamic differences in the material state as well. While the results of the raw material's first heating cycle T_g = -64.1 °C corresponded with the second heating cycle of the raw material T_g = -64.6 °C and the molten box structures T_g = -64.6 °C, the first heating cycle of the box scaffolds was shifted to elevated temperatures T_g = -60.7 °C. This also indicated a different morphology of the box scaffolds since the shift in glass transition temperature may be the result of aligned and constrained molecules due to stretching, quenching and oriented solidification.

If comparing the XRD pattern of a box structured scaffold to the molten sheet as presented in Figure 44, several differences turn out. On one side the integral of the (110)-plane peak of the scaffold exhibited just 60 % of the corresponding integral from the sheet indicating a reduced crystallinity or reduced crystal size of the scaffold's PCL. On the other hand, the (200)-plane peak stayed in position considering both, samples with $2\Theta = 23.70°$ for the PCL sheet and with $2\Theta = 23.71°$ for the scaffolds while the peak of the (110)-plane of the scaffold was significantly shifted to $2\Theta = 21.37°$ compared to the sheet with $2\Theta = 21.43°$. This result indicated an anisotropic deformation of the crystalline morphology induced by the stretching, quenching and oriented solidification under mechanical forces during MEW.

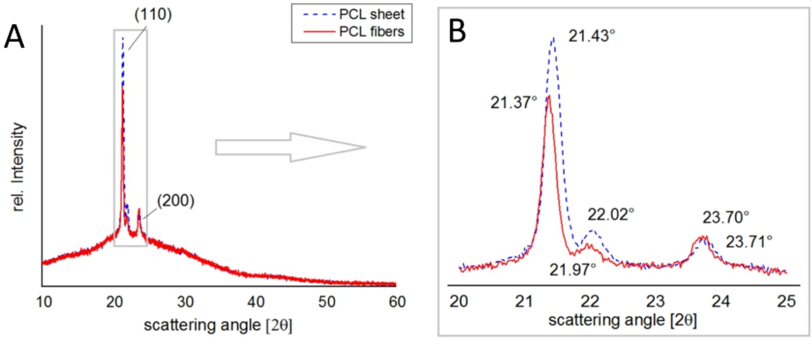

Figure 44: XRD patterns of a PCL box structure scaffold and sheet. A) PCL box structure scaffolds were analysed, molten afterwards and analysed again. The (110)-plane peak of the scaffolds was significantly shifted whereas the (200)-plane peak remained in position. This indicated an anisotropic crystallisation under external mechanical forces. B) Section of peak (110) and (200).[129]
(Published under Creative Commons licence CC BY 3.0)

Here, the measurement of the scaffold and the sheet showed neither differences in the background signal intensity, nor differences were observed investigating randomly deposited fibre scaffolds. Thus, no significant influence of the macroscopic fibre scaffold geometry could be revealed for the XRD character-isation. Furthermore, no alteration of the crystalline peaks could be measured by repetition analysis on the same sample three times.

Additional trials to prove the oriented semi-crystalline morphology of the uni-axial aligned PCL submicron fibres were conducted under different planar angles as shown in Figure 45. The highest peak intensity with i = 1900 cps was observed scanning along the fibre printing direction in comparison with XRD analysis at 30° and 60° showing only i = 1200 cps and i = 1500 cps. By thermal aging treatments below the melting onset temperature T = 55 °C, slightly increased (110)-plane peaks were achieved due to secondary crystallisation and most crystal growing processes.

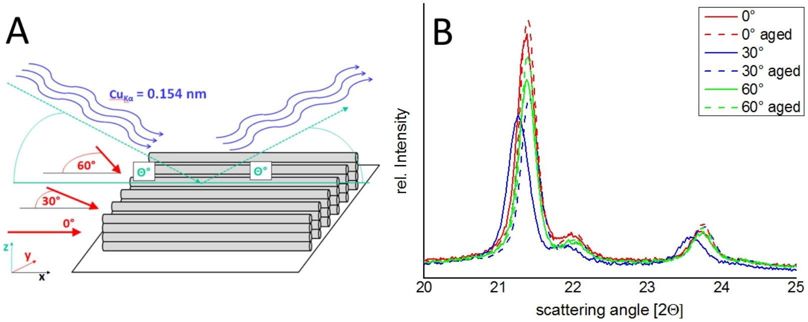

Figure 45: XRD patterns of uniaxial aligned fibre scaffolds at different planar angles. A) Illustration of the measurement procedure, XRD patterns have been plotted along the fibres with 0° and at 30° and 60° tilted in planar directions to the fibres. B) Resulting XRD patterns revealed an angle-dependency of the aligned fibres indicating an isotropic crystal morphology. Further thermal aging close to but below the melting temperature onset of PCL led to secondary crystallisation due to observed slightly increased peaks.[129]
(Published under Creative Commons licence CC BY 3.0)

Taking the SFM, DSC and XRD measurements into account, information about the thermodynamical state of the submicron PCL fibres could be gathered. The macromolecular alignment in stretching direction with plastically deformed and oriented crystalline could be confirmed. Nevertheless, an amorphisation or forming of preferred small crystalline structures seemed to occur due to the high quenching of the MEW jet. Further, thermal aging below the melting temperature led to significantly increased secondary crystallisation indicating an incomplete crystallisation of fibres during processing or at least a high re-crystallisation potential of fibres.

How this may influence performance properties of resulting scaffolds remains unclear and must be further investigated. However, it is known that strengthening effects of oriented crystal structures along the testing directions can occur via defined processing, cooling and stretching of samples.[287, 288]

4.3.4 Cell adhesion of submicron fibre scaffolds

The cell tests and fluorescence microscopy were conducted by Kathrin Hahn.

While the submicron fibre scaffolds could not be detached from the common aluminium collector plate without influencing the structure, MEW deposition onto surface coated glass slides as cell repellent substrate was successful. As the experiments revealed, PCL scaffolds tended to detach from collector surfaces when immersed in water- or ethanol based solutions. In contrast, utilising NCOsP(EO-*stat*-PO)-coatings led to a suitable adhesion between substrate and scaffold. Even after several treatment steps including immersion in culture medium and medium changes (Figure 46) no detachment could be observed after 10 DIV.

Moreover, hMSCs did not adhere to the substrate glass slides at all, enabling the conclusion of full adherence to the scaffolds. Even though, the cells started to migrate into the scaffold structure indicating the usability of such PCL submicron scaffolds for further TE approaches. While the hMSCs tend to span more over 90 µm meshes and formed cell clusters on top of the scaffold after 4 DIV, an increased migration into the structure and between the fibre walls was observed in case of 150 µm mesh width scaffolds already after 4 DIV.

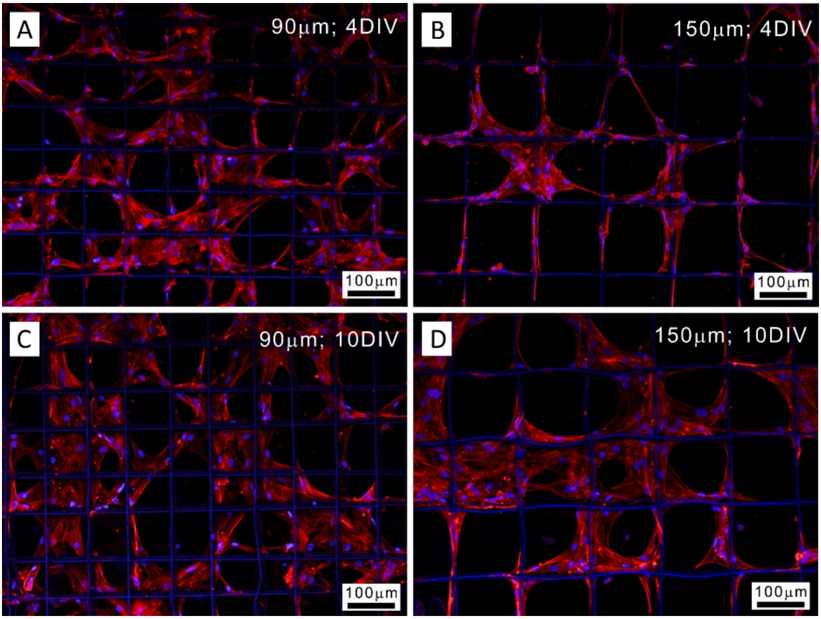

Figure 46: hMSC adhesion experiment on submicron fibre scaffolds. A&B) box structured scaffolds with 90 µm and 150 µm mesh width containing 100 layers after 4 DIV. C&D) Results after 10 DIV. The cells adhered properly on top of the scaffold and started to migrate into the boxes between the fibre walls. The scaffolds were deposited on NCO-sP(EO-stat-PO)-coated glass slides, only cell adhesion on the scaffolds was observed.[129]
(Image by Kathrin Hahn, published under Creative Commons licence CC BY 3.0)

Furthermore, the cells started to form interconnected structures with circular shapes, preferably in the scaffold with 150 µm mesh width and after 10 DIV accompanied by deformation of the fibre walls. Interestingly, the submicron sized fibres were also stained distinctly by the blue Hoechst medium as the cell's nuclei enabling a desirable imaging process by fluorescence microscopy.

4.4 Conclusion

In the presented study, uniform submicron sized PCL fibres (fØ = 817 ± 165 nm) could be accurately deposited with 100.6 ± 5.1 µm mesh width to 100 layer box structured scaffolds for the first time. Even if initiated for TE purposes, several high end applications could benefit from accurately defined construct structures with high specific surfaces.

Here, it is key to understand morphological evolution of the macromolecular structure during MEW processing to assess or influence resulting performance properties of printed scaffolds. Conducted material investigations additionally revealed an oriented crystallinity of the fibres in combination with amorphous or small-sized crystals by quenching effects. A rational explanation was found by considering the high acceleration rates of the polymer melt jet during manufacturing inducing macromolecular stretching, alignment and oriented solidification.

In order to use fragile submicron sized fibre scaffolds for cell culture studies, a proper surface coating approach for improved adhesion to the underlying substrates has been introduced. Additionally, subsequent cell experiments yielded a proper cell adhesion and migration behaviour proving the potential of submicron scaffolds for further TE studies.

In conclusion, the first step towards understanding resulting fibre properties was examined. However, a variety of questions remain. In this context, it would be important to further analyse the impact of MEW processing conditions on resulting mechanical, chemical and biological characteristics of printed scaffolds.

5 Printing below CTS

Parts of this chapter have already been published in the following article:

Gernot Hochleitner, Almoatazbellah Youssef, Andrei Hrynevich, Jodie N. Haigh, Tomasz Jungst, Jürgen Groll and Paul D. Dalton

“*Fibre pulsing during melt electrospinning writing*”;

Bionanomaterials 2016, DOI: 10.1515/bnm-2015-0022

Presented experiments, data evaluations and writing were accomplished independently if not clearly stated otherwise.

5.1 Introduction

Utilising MEW for printing of highly defined scaffolds usually necessitates an exact control over the jet speed. All reported cases in literature[3] show defined scaffolds manufactured using collector speeds matching or exceeding CTS. Nevertheless, other non-linear structures may be processed at collector speeds below CTS additionally, as already indicated by Brown et al.[137] and presented in Figure 17 on page 31. In fact, these prints neither exhibited highly ordered nor distinct reproducible structure elements, however, proper systematic studies aiming for defined fibre deposition control with MEW are missing so far.

In contrast to this, investigations focussing on viscous buckling of liquid ropes impacting solid, moving surfaces have been widely studied in the field of applied physics. In this case, the use of suitable fluid mechanical sewing machines (FMSM)[289] or similar devices is crucial (Figure 47 A&B). Usually honey[290], syrup[291] or silicone oil[292], which are considered as pure viscous fluid, are pumped through a nozzle, fall by gravity and are collected by a moving belt similarly to MEW. Indeed, no HV field is applied using FMSMs unlike to EHD-driven deposition methods. Nevertheless, studies on viscous buckling exhibit interesting insights as the similarities may prevail the contraries between both techniques. For instance, sinusoidal meanders or other regular patterns can be deposited using simple FMSMs as reflected in Figure 47 C&D. Further, these structures are highly reproducible and predictable as available numerical models come close to experimental outcomes.[291-294]

---

[3] A list of primary research articles focusing on MEW is presented in Table 2 on page 39f.

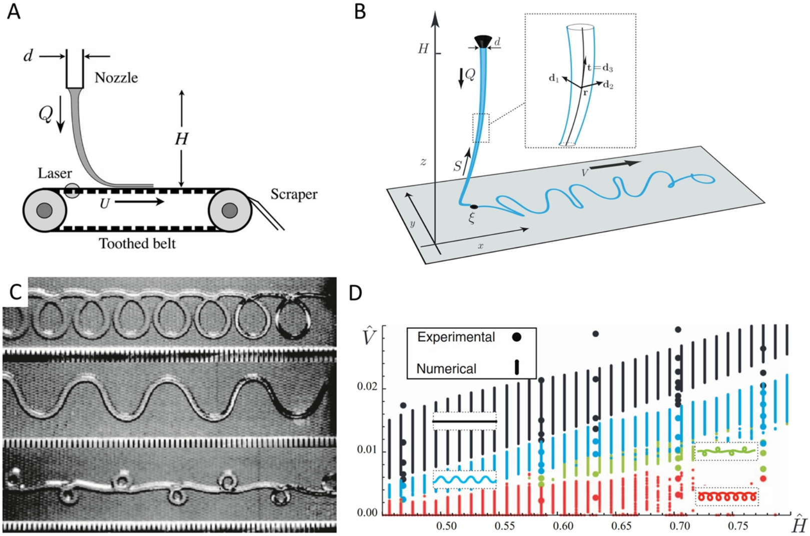

Figure 47: Illustration of buckling of viscous ropes falling on moving surfaces. A) Schematic drawing of a FMSM. The viscous fluid passes the nozzle and falls onto a moving collector belt. The belt speed can be controlled using a laser-based sensor, a scraper removes the deposited fluid for continuous use.[292] B) Schematic of buckling of a viscous rope impacting a solid surface.[291] C) Photographs of different viscous buckling patterns deposited below CTS.[291] D) Dependency of pattern morphology as function of the falling height $\hat{H}$ *and the belt collector speed* $\hat{V}$*. At CTS straight lines can be observed whereas sinusoidal meanders, sidekicks and translated coiling for instance can occur at gradually decreasing collector belt speeds.[291]*
(A: Reprint, Copyright © 2017 by the American Physical Society, B-D: Reprint, with the permission of AIP Publishing)

However, investigations made focussed on the viscous buckling effect only and not on performance properties of printed structures. In case of basic viscous fluids, no usable constructs can be attained due to missing dimension stability. If the knowledge about buckling phenomena can at least be partially applied to MEW processing, novel beneficial design strategies for scaffolds may emerge.

5.2 Experimental section

5.2.1 Polymer

For the present study, PCL as standard polymer was used since it provided the most suitable printing conditions. The utilised PCL, a GMP grade material, was purchased from Corbion Inc. (CAS# 24980-41-4, PURASORB PC 12, Gorinchem, Netherlands). The polymer was used as received.

5.2.2 MEW device

In this study, the **High-temperature device** as already introduced on page 55, was used for systematic pattern and scaffold printing. Further, another MEW device was built for precise manufacturing control.

5.2.2.1 High-precision MEW device

The setup of this MEW device was built with a focus on advanced deposition accuracy ≤ 2.0 µm and repeatability ≤ 1.0 µm utilising ball-screw axis (PRO115-05mm-0150-TTM-5V-NC-DMS, Aerotech GmbH, Nuremberg, Germany) driven by rotation motors (BMS35-A-D25-E10000ASH, Aerotech GmbH, Nuremberg, Germany) and with HALAR function calibration orthogonally aligned (x- and y- axes) and mounted on a stone table (custom-made, flatness = 5 µm, Johann Fischer Aschaffenburg Präzisionswerke GmbH & Co. KG, Aschaffenburg, Germany) with air buffers. The setup contained a portal construction with additional z-axis (ATS03005-M-5-BMS-NC-9DU, Aerotech GmbH, Nuremberg, Germany) for accurate spinning distance control. Similar to the other MEW devices, a polyetheretherketon housing was custom-built for a bi-zonal heater based on an electrical coil heater and a custom-made HV electrode with an integrated electrical heater controlled by a PID (cTRON, JUMO GmbH & Co. KG, Fulda, Germany). The HV electrode was opposed to a polished aluminium plate as collector surface. Glass syringes with metal Luer-Locks (FORTUNA OPTIMA®, 3ml, Poulten & Graf GmbH Wertheim, Germany) were used as melt reservoir with N_2 gas pressure (precision pressure, control valve, FESTO, Berkheim, Germany) as infeed system. To generate a proper electrical field, an HV source (HCP14-20K, FuG Elektronik GmbH, Schechen, Germany) was connected. All three axes were driven by the Aerotech motion sequencing software (A3200 motion composer, Aerotech, Nuremberg, Germany).

5.2.3 Manufacturing conditions

In order to deposit defined regular and reproducible patterns below CTS, instrumental parameters without resulting *pulsing* or *long beading* conditions were chosen. Further, MEW printing was conducted using glass slides (uncoated, 26 x 76 mm^2, VWR LLC, Radnor, USA) as collector surfaces to enable a suitable visualisation via light microscopy.

To ensure stable printing for pattern analysis in a broad range of feeding pressures $p = 0.5$, 1.0, 2.0 and 3.0 bar, a 30 G spinneret (≈ 160 µm IØ) was utilised. As shown **Fibre pulsing during MEW** on page 51ff, the feeding pressure is the most suitable parameter to influence the resulting fibre diameter and the CTS of the jet. Therefore, p was chosen as instrumental variable. For proper printing stability, an acceleration voltage of $U = 2.5$ kV at a spinning distance of $h = 1.0$ mm was applied. The heating temperature was constantly set to $T = 90$ °C.

In order to investigate the resulting mechanical tensile behaviour, scaffolds were printed at $s_c = 100$ % CTS, 90 % CTS, 80 % CTS and 70 % CTS. Here, the instrumental parameters were tuned for proper scaffold processing. Hence, an acceleration voltage of $U = 4.8$ kV at a spinning distance of $h = 3$ mm, a feeding pressure of p = 0.2 bar, a heating temperature of T = 76° C and a spinneret with 24 G (≈ 310 µm) were utilised.

Further, different scaffolds were manufactured under different instrumental conditions. These were processed as proof of feasibility using the results of pattern investigation below CTS. Applied MEW conditions are mentioned in the related figure captions.

All investigations were performed at room temperature 21 ± 2 °C and an environmental humidity of 35 ± 15 % r.h. Measured values contain the standard deviation of a sample (SD), as already introduced on page 58.

5.2.4 G-code programming

For systematic fibre collection below CTS, line arrays, consisting of n = 10 reproduced lines, were programmed and investigated using n = 5 sample spots for sufficient analysis conditions. Beginning at $s_c = 50\ \mathrm{mm \cdot min^{-1}}$, the collector speed was incrementally raised with steps of $\Delta s_c = 25\ \mathrm{mm \cdot min^{-1}}$ until CTS was exceeded. Due to this approach, a (semi) quantitative analysis of pattern prints with corresponding accuracy could be examined.

Scaffolds for mechanical testing were manufactured with 10 layers in total, 5 layers in 0° direction and 5 layers in 90° direction. The distance between the programmed fibres was set to 300 µm. The collector speed was adjusted in order to match the 100 % CTS, 90 % CTS, 80 % CTS and 70 % CTS of the jet. Conveniently, the resulting scaffolds are named according to the manufacturing speed. G-codes for line arrays and scaffold printing are provided in the supplementary information, chapter **Printing below CTS** on page xxx f.

5.2.5 Optical analysis

To visualise the fibre patterns, a microscopy study (Discovery V20, Carl Zeiss AG, Oberkochen, Germany) was conducted. For geometrical analysis $n = 5$ fibres were measured $n = 5$ times (total of $n = 25$). In case of the peak-to-peak value of the sinusoids, the measurements were performed from the minimum to the maximum orthogonally to the printing direction. The wavelength of the sinusoidal meanders was determined parallel to the printing direction. All measurements started and ended always at central lines of fibres. Using this approach, a straight line would have no peak-to-peak value and an infinite wavelength.

Further, images were taken via SEM (Crossbeam 340 and Ultra Plus with GEMINI e-Beam column, Carl Zeiss AG Oberkochen, Germany) at 1 – 2 kV acceleration voltage and 3 – 5 mm distance. Beforehand, scaffolds were coated using a sputtering device with platinum up to a thickness of 5 nm if not otherwise stated.

5.2.6 Mechanical testing

The tensile characteristics: Young's modulus E, maximum tensile strength σ_{max}, ultimate tensile strength σ_u, ultimate tensile strain ε_u, and the specific work of fracture W_f of the four different scaffold types (100 % CTS, 90 % CTS, 80 % CTS and70 % CTS) were determined.

For evaluation, the following technical equation was applied[84]:

$$\sigma = \frac{F_t}{A_0} = E \cdot \varepsilon \qquad (12)$$

σ = tensile stress; F_t = tensile force; A_0 = initial cross-section;

E = Young's modulus; ε = tensile strain

Testing considerations were applied based on the ASTM D 882 – 02, the standard test method for tensile properties of thin plastic sheetings. This includes the reference to the initial cross-section area A_0 during elongation and does not comprise the true strain correction, due to the missing information about the lateral contraction or Poisson's ratio of MEW derived PCL fibres. However, the specific work of fracture was calculated considering the following equation[295]:

$$W_f = \int_0^{\varepsilon_u} \sigma_u \, d\varepsilon \qquad (13)$$

W_f = specific work of fracture; σ_u = ultimate tensile stress;
ε = tensile strain; ε_u = ultimate tensile strain

In order to determine the resulting stress in the fibres during tensile testing, A_0 of the scaffolds was quantified by SEM. For each single sample type, $n = 20$ measurements of fibre diameters were conducted. Further, the numbers of single fibres were counted using microscopy. The resulting cross-section A_0 was calculated using the arithmetic average of fibre diameters and multiplied with the total number of fibres along the tensile direction. The Young's moduli E were defined as slopes at infinitesimal elongations ranging from $\varepsilon_1 = 0$ to $\varepsilon_2 = 0.005$ (≈ 0 to 0.5 % tensile strain). Further, the (virtually) linear regions of the scaffolds were characterised by the secant modulus E_s fitted between $\varepsilon_1 = 0.01$ to $\varepsilon_2 = 0.03$ (≈ 1 to 3 % tensile strain).

In total, $n = 4$ scaffolds of the four different types with an initial length of $\varepsilon_0 = 50$ mm and a width of 10 mm were tested along the fibre axes at 24 ± 1 °C temperature. Therefore, a static mechanical testing device (Z010, Zwick Roell AG, Ulm-Einsingen, Germany) with a 200 N load cell was used at 12.5 mm$\cdot$min^{-1} testing speed. The mechanical tester stopped until fracture occurred, defined as sudden loss of the tensile force with $\Delta F_t \geq 40$ %.

5.3 Results and discussion

5.3.1 MEW printed patterns below CTS

As already discussed in **Fibre pulsing during MEW** on page 51, the CTS of the PCL jets decrease with increasing feeding pressures or fibre diameters, respectively. However, reducing the collector speed below CTS led to printing of sinusoidal meanders as reflected in Figure 48.

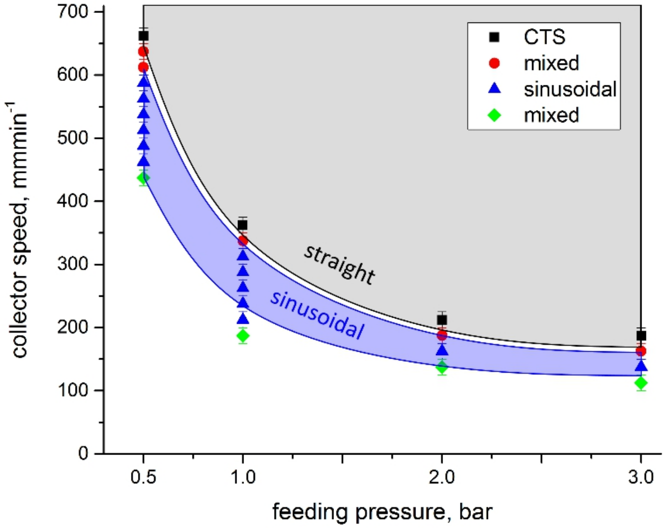

Figure 48: Geometry of printed fibres below CTS. As the collector speed fell below CTS, straight or catenary structure turned into sinusoidal meanders reproducibly. Further reducing collector speeds led to mixed structures consisting double sinusoids, sidekicks, translated coiling, figures of eight and undefined elements. Sinusoidal structures were defined as > 90 % of prints exhibited clearly shaped sinusoids. Unlike p =2.0 bar and p = 3.0 bar, the sinusoidal regime in case of p = 0.5 bar and p = 1.0 bar exhibited sinusoidal meanders with a bimodal peak-to-peak distribution additionally.

Interestingly, all investigated pressures (p = 0.5; 1.0; 2.0 and 3.0 bar) exhibited distinct sinusoidal regimes (defined as > 90 % of fibres are sinusoidal), at the same s_c/CTS ratio at a collector speed of 81 ± 8 % CTS $\geq s_c \geq$ 65 ± 7 % CTS. Moreover, the results showed clearly, that no other patterns occurred between CTS and the sinusoidal regime. Nevertheless, a mixture of both structures occurred at 100 % CTS $> s_c >$ 81 ± 8 % CTS. This transition regime can be attributed to small changes in jet speeds due to natural statistic errors. However, processing at $s_c <$ 65 ± 7 % CTS independent to the feeding pressure, resulted in different other deposition patterns finally. Here, another transition regime, comprised of sinusoidal meanders and sidekicks, was observed.

The correlated pattern functions of feeding pressure (jet speed/thickness) and collector speed via MEW printing resembled the buckling phenomenon of falling viscous threads using FMSMs particularly (comparison of Figure 47 D and Figure 48). Here, the same explanation stands to reason, the underlying fluid kinematics including considerations of inertia, surface tension, flow processes, etc. combined with further bending and twisting may have validity.[296] In Figure 49, fibre arrays are presented, elucidating the high MEW reproducibility.

However, even if printed fibres conformed to the coalescence viscous prints at the first glance, a clear difference could be observed in the accelerating forces acting on the jets. Unlike FMSMs, the gravity influences are subsidiary during MEW processing, the electrical field is prior. Thus, the interaction of the electrically charged MEW jet and the deposited fibres can only be neglected in monolayer structures, but not in case of multi-layered scaffolds. Such resulting constructs and their mechanical characteristics are further discussed in the subsequent chapter **Mechanical testing** on page 123ff.

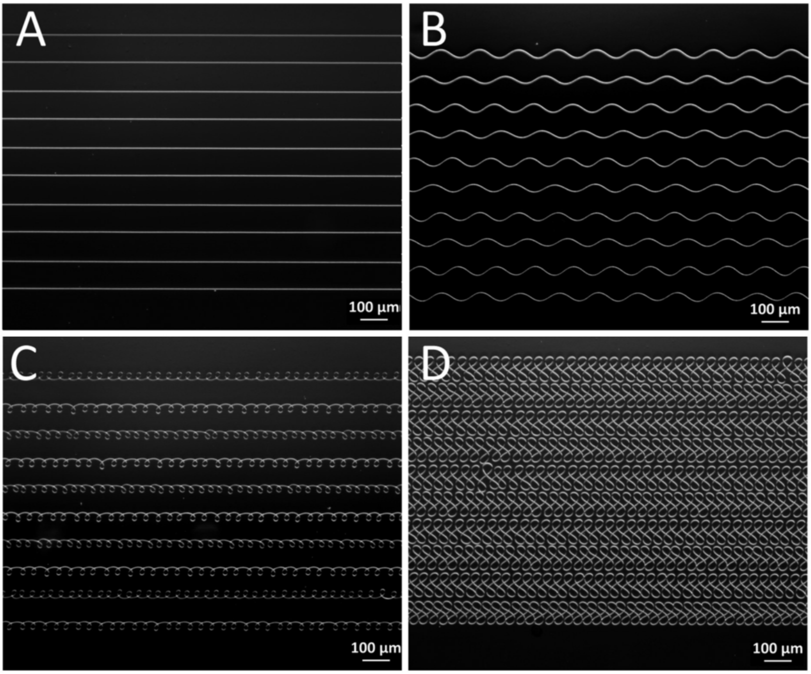

Figure 49: Microscopy images of different reproducible fibre patterns at CTS and below. Presented samples were printed in arrays with n = 10 fibres. The uniformity of the lines indicated a highly stable CTS and hence proofed the opportunity for reliable MEW processing. Based on this, homogenous non-linear polymer patterns, similar to those of viscous fluids produced by FMSMs, were feasible for subsequent investigations. A) 100 – 110 % CTS, straight lines. B) 75 – 80 % CTS, sinusoidal meanders. C) 30 – 35 % CTS, translated coiling. D) 10 – 15 % CTS, figures of eight. Samples were printed at p = 1.0 bar, other parameters as introduced.[252]
(Published under Creative Commons licence CC BY-NC-ND 3.0)

The evolution of the fibre pattern printed using the example of p = 0.5 bar is presented in Figure 50. As indicated by the microscopy images, the shape of the sinusoidal meanders varied at different collector speeds and also exhibited so called double meanders in some cases. In the represented distinct sinusoidal regime at $550\ \text{mm}\cdot\text{min}^{-1} \geq s_c > 450\ \text{mm}\cdot\text{min}^{-1}$ a systematic change in peak-to-peak value and wavelength could be observed.

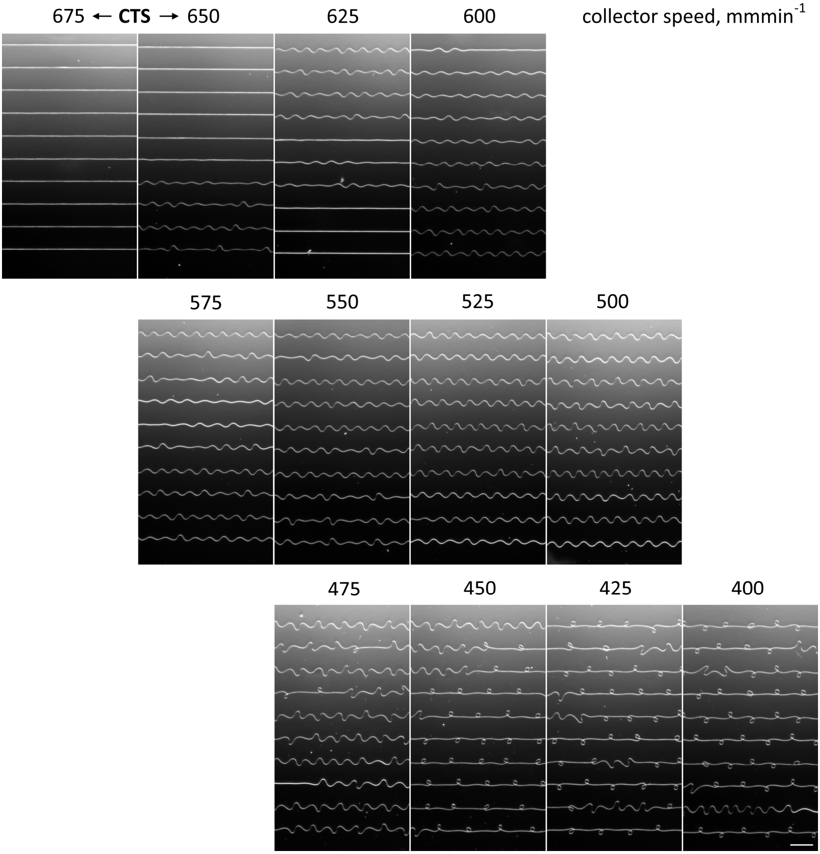

Figure 50: Microscopy images of incrementally changed fibre patterns at CTS and below. A feeding pressure of p = 0.5 bar was utilised, the collector speed is provided in the figure. Sinusoidal shaped fibres were deposited at $s_c \leq 650$ mm·min^{-1} < CTS. As s_c decreased further, the peak-to-peak value of the sinusoids increased while the corresponding wavelength decreased. At sc < 475 mm·min^{-1} sidekicks occurred additionally. Scale bar = 100 µm.

The corresponding quantification of sinusoid shapes as function of the collector speed for the four investigated feeding pressures can be found in Figure 51.

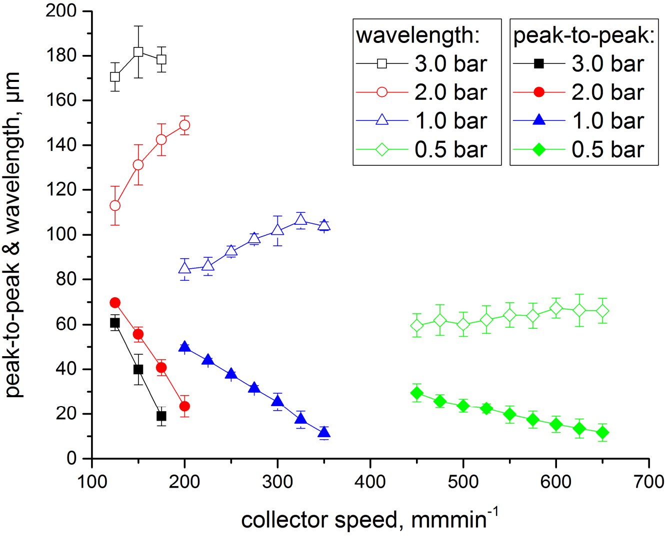

Figure 51: Quantified geometry of sinusoidal structure elements as function of pressure and collector speed. A clear trend was observed, larger fibres printed at higher pressures exhibited higher peak-to-peak values and wavelengths. Additionally, reducing the collector speed led to significantly decreased wavelengths and increased peak-to-peak values.

When printing in a sinusoidal regime, a reduction of the collector speed led to decreased wavelengths and increased peak-to-peak values, independent of the feeding pressure. Nevertheless, higher feeding pressures exhibited sinusoids with higher peak-to-peak values and wavelengths in general. Taking basic mechanical consideration into account, this can be attributed to the increased fibre diameter size necessitating a higher bending force for printing meandering patterns with small radii.[84] Hence, a higher lateral distraction of the jet occurred leading to increased sinusoid peak-to-peak values which must accompany increased wavelengths considering a constant fibre density and constant cross-section. However, this observed structural variation of the sinusoidal meanders as function of pressure and collector speed provides the potential for tailoring fibre morphology.

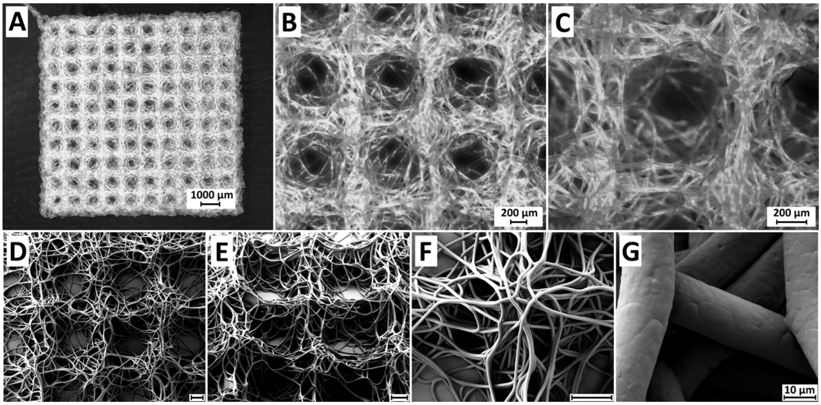

Figure 52: Microscopy and SEM Images of a proof example scaffold processed below CTS. MEW printing below CTS resulted in a semi-structured scaffold with multimodal pore sizes. Here, the G-code design was identical with prior presented accurate box structure scaffolds. The mesh width was set to 1000 µm, instead of precisely defined fibre walls, disordered and highly porous wall structures occurred. A-C) Microscopy images as an overview, D-G) SEM images of the fibre structure. Scale bar = 200 µm. Instrumental parameters: 22 G spinneret, T = 76 °C, U = 6.5 kV, p = 0.3 bar, h = -4.5 mm, s_c = 30 mm·min^{-1} < 20 % CTS with 15 x 2 layers.
(D-G: Image by Dr. Claus Moseke and Judith Friedlein)

When printing whole scaffolds below CTS, a semi-ordered structure was observed (Figure 52). Here, the EHD driven deposition behaviour led to semi-controlled fibre coiling and piling as the MEW jet was attracted by closely deposited PCL fibres. Therefore, disordered but highly porous fibre bands were formed instead of accurately stacked fibre walls. Nevertheless, the mesh widths between the semi-ordered fibre bands can be basically adjusted using G-code programming and thus, utilised for scaffolds with bi- or multimodal pore distributions. To investigate the resulting mechanical characteristics of those semi-ordered structures, a systematic study was performed.

5.3.2 Mechanical testing

To compare the tensile behaviour of ordered and semi-ordered scaffolds, four different types were MEW printed, termed as 100 % CTS, 90 % CTS, 80 % CTS and 70 % CTS according to used relative collector speed. While 100 % CTS can be seen as reference scaffold, the other three scaffolds were printed in the sinusoidal fibre deposition regime. All fibre diameters were stably deposited (excluding *pulsing* and *long beading*, CV ≤ 5.0 %) and almost identical, as presented in Table 6.

Table 6: Fibre diameter quantification of four different scaffolds: 100 % CTS, 90 % CTS, 80 % CTS and 70 % CTS. The fibres were neither pulsed, nor long beaded. Further, the fibre diameters of the different scaffolds are almost identical.

	100 % CTS	**90 % CTS**	**80 % CTS**	**70 % CTS**
Average, µm	21.3	21.2	21.7	20.4
SD, µm	1.0	0.4	0.7	0.2
CV, %	4.7	1.9	3.2	1.0

Although scaffolds printed at reduced collector speeds must consist of more mass and fibre length (reference: 100 % CTS with box structure), the total cross section after tensile orientation must be similar as all scaffolds exhibited a similar fibre diameter, test strip geometry and amount of fibre layers. Here, theoretically, the total strain until rupture of the scaffolds with more fibre material should be increased. However, the semi-ordered deposition pattern comprise further changes in scaffold design. As shown in Figure 53, the position and number of fibre contact points was significantly different between 90 % CTS, 80 % CTS and 70 % CTS. Furthermore, the utilisation of lower collector speeds led to non-linear fibre patterns and therefore less ordered fibre alignment.

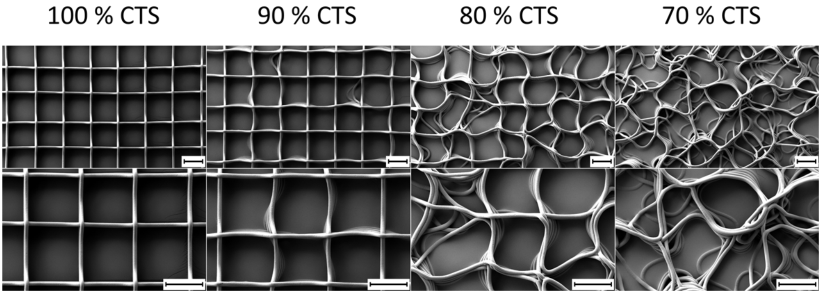

Figure 53: SEM images of four different scaffolds: 100 % CTS, 90 % CTS, 80 % CTS and 70 % CTS. The scaffold structure became more and more disoriented at decreased collector speeds falling below CTS. Scale bar = 200 µm.
(Image by Dr. Claus Moseke and Judith Friedlein)

Semi-crystalline thermoplastics including PCL usually exhibit at least two phases determining the resulting physical properties of the material: a crystalline and an amorphous phase. At the very beginning of the deformation process, at only a few percentage of strain, a linear-elastic region could be observed (Figure 54). Here, the amorphous phase (at $T > T_g = -60$ °C[297]) between crystalline regions became partially aligned, with the potential to fully relax with ceasing external forces.[298]

At higher strains and deformations, semi-crystalline polymers usually show a linear viscoelastic, followed by a non-linear viscoelastic, region via shifting and rearrangement of lamella positions. This mechanical behaviour was observed for 100 % and 90 % CTS at approximately 5 to 15 % of strain (reflected in Figure 54 B). After even more tensile strain, lateral contraction and stationery plastic deformation occurs, accompanied by breaking crystalline structures and strong orientation of the macromolecules along the external force[298], which was observed for 100 % and 90 % CTS at about > 25 % of strain.

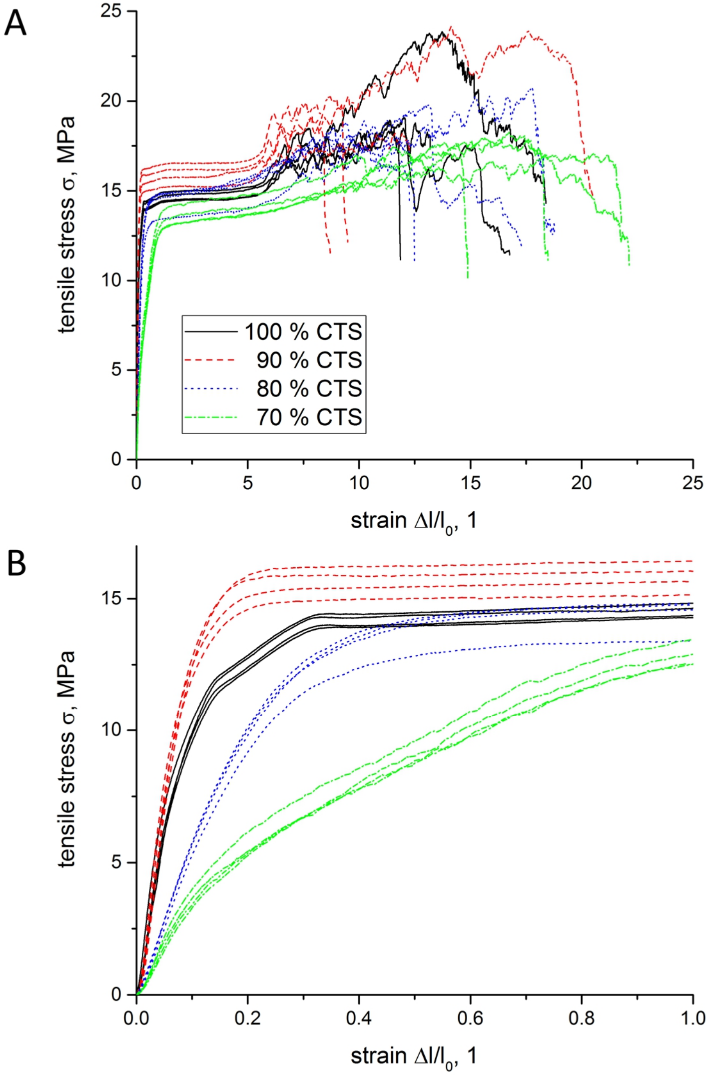

Figure 54: Tensile stress-strain curves of four different scaffolds: 100 % CTS, 90 % CTS, 80 % CTS and 70 % CTS. A) Full stress-strain function until rupture. B) Close-up-view of the initial region ranging to ε = 1.0 or 100 % elongation respectively. Scaffolds with more disordered structures exhibited lowered Young's moduli, especially at the small deformations.

As known from literature, PCL can have a very high plastic deformability (ε_u = 600 % ultimate strain[299]) until rupture. This can be explained by the outstanding plastic deformation ability or sliding properties of the macromolecules aligned by the external tensile force. In case of the tensile tested scaffolds in Figure 54, even more tensile elongation capability could be observed. Here, in addition to the mentioned plasticity, the scaffold design took advantage. As single fibre walls along the testing direction broke, orthogonally oriented fibre walls tended to align along the external tensile force. This structural reorientation led to ε_u = 13 ± 5 (≈ 1300 ± 500 %) in case of 90 % CTS and even to ε_u = 20 ± 2 (≈ 2000 ± 200 %) in case of the 70 % CTS samples.

Table 7: Summary of the tensile characteristics of four different scaffolds: 100 %, 90 %, 80 % and 70 % CTS. Values are given as arithmetic average ± SD.

	100 % CTS	**90 % CTS**	**80 % CTS**	**70 % CTS**
E, MPa	66 ± 21	40 ± 11	26 ± 8	14 ± 6
E_s, MPa	154 ± 23	173 ± 22	55 ± 3	42 ± 7
σ_{max}, MPa	20 ± 3	21 ± 3	19 ± 2	18 ± 1
σ_u, MPa	14 ± 3	14 ± 3	12 ± 2	11 ± 1
ε_u, 1	15 ± 3	13 ± 5	15 ± 3	20 ± 2
W_f, mJmm^{-3}	248 ± 63	227 ± 119	244 ± 55	290 ± 53

While the ultimate strain tended to increase progressively with 90 %, 80 % and 70 % CTS, both, the maximum and ultimate tensile strength decreased from 90 % CTS scaffolds with σ_{max} = 21 ± 3 MPa and σ_u = 14 ± 3 MPa towards 70 % CTS scaffolds with σ_{max} = 18 ± 1 MPa and σ_u = 11 ± 1 MPa.

When considering the total amount of relative work of fracture, the discussed increase in fibre mass for 70 % and 80 % compared to 90 % CTS scaffolds turned out (summary presented in Table 7). Here, $W_f = 227 \pm 119$ mJmm^{-3} for 90 %, $W_f = 244 \pm 55$ mJmm^{-3} for 80 % and $W_f = 290 \pm 53$ mJmm^{-3} for 70 % CTS was measured.

Beside the discussed chances in tensile characteristics, alternation in Young's moduli seem to be most prominent. At infinitesimal strains of 90 % CTS with $E = 40 \pm 11$ MPa, the modulus decreased significantly to $E = 14 \pm 6$ MPa for 70 % CTS samples. The same behaviour was observed for the secant modulus at the virtually linear region decreasing from $E_s = 173 \pm 22$ MPa to $E_s = 42 \pm 7$ MPa for 90 % and 70 % CTS, respectively.

The decreasing stiffness of scaffolds printed at decreasing collector speeds can be ascribed to the progressively forming semi-ordered elements. While completely aligned fibres (100 % CTS) are solely exposed to material strains or tensile deformation under external tensile forces, scaffolds with less structured elements (70 % CTS) undergo a certain orientation deformation at lower stresses at first and then material strain with tensile deformation subsequently. Indeed, this describes an idealised case, even 100 % CTS scaffolds contained sagged fibres in z-direction between fibre intersections for instance, while partially coiled fibres of 70 % CTS scaffolds also showed material deformation during alignment by external tensile forces obviously. However, this concept helps to understand the reduced stiffness and emphasizes the high importance of defined fibre deposition for intended controlling of the resulting mechanical properties.

Such discussed changes in scaffold stiffness may influence cell and tissue behaviour largely as the corresponding tensile strains are present in relevant deformation sizes for TE approaches. Several publications could associate the scaffold's mechanical properties with variation in cell adhesion, proliferation or differentiation characteristics determining the cell and tissue fate widely.[300-302] This can be explained by the ability of adherent cells to sense and respond to the ECM and its micromechanical environment.[303] In the first instance, the material stiffness seems to considerably influence cell recruitment or migration, angiogenesis and differentiation of MSCs *in vivo*.[304, 305]

Therefore, changing the collector speed for stiffness variation could help to process improved scaffolds. Indeed, this study is just the first of several necessary steps to understand non-linear deposition below CTS and resulting tensile mechanical properties. In addition, the understanding of shear properties could be very important to meet the actual requirements of the applied components and hence, need to be investigated as next step. Nevertheless, this study may help to increase the spectrum of feasibility and adds a new approach into the toolbox of TE for ongoing applied research.

5.4 Conclusion

MEW printing below CTS can be utilised to deposit sinusoidal shaped fibres reproducibly. Here, significant similarities to buckling of viscous falling fluids were observed. During MEW, the feeding pressure and the collector speed can be used to influence the print's morphology largely leading to a potent tool for influencing scaffold design.

In order to investigate resulting structures, different scaffold types were manufactured under sinusoid printing conditions at 100 %, 90 %, 80 % and 70 % CTS and tested concerning their tensile mechanical properties. It could be demonstrated, that the tensile strength and stiffness decreased progressively while the relative work of fracture and strain at rupture increased with semi-ordered scaffold patterns.

This simple method for scaffold design facilitates tailoring the mechanical characteristics to specific needs of the application via MEW. Using this approach, novel highly porous and semi-ordered structure elements can be processed easily and be further combined synergistically with established MEW designs for TE purposes and more.

Disadvantageously, the structural accuracy of AM-based fibre deposition ceases at multiple layers when printing below CTS in 0° and 90° direction. Due to the EHD printing behaviour, highly porous structures, as desired for TE applications, are formed nonetheless. However, by the utilisation of a MEW device with sufficient axes acceleration conditions, enforced pattern printing by collector movements could be realised, leading to highly defined and reproducible construct elements.

6 Photo-cross-linkable polymers

Parts of this chapter have already been published in the following two articles:

Fei Chen*, Gernot Hochleitner*, Tim Woodfield, Jürgen Groll, Paul D. Dalton, Brian G. Amsden

“Additive Manufacturing of a Photo-Cross-Linkable Polymer via Direct Melt Electrospinning Writing for Producing High Strength Structures”

Biomacromolecules 2016, DOI: 10.1021/acs.biomac.5b01316

Gernot Hochleitner*, Fei Chen*, Carina Blum, Paul D. Dalton, Brian G. Amsden, Jürgen Groll

“Melt electrowriting below the critical translation speed to fabricate crimped elastomer scaffolds with non-linear extension behaviour mimicking that of ligaments and tendons”

Acta Biomaterialia 2018, DOI: 10.1016/j.actbio.2018.03.023

*Shared first authorship

Presented experiments, data evaluations and writing were accomplished independently if not clearly stated otherwise.

6.1 Introduction

One key aspect for a load-bearing implant in a biomedical application is a reliable and defined set of mechanical characteristics.[169] Amongst these are not only strength, Young's modulus, strain and toughness, but also resistance against long term deformation or creep, as well as cycle fatigue, elasticity at higher strain rates, or with other words recovery after stress release for instance.[306] Such material properties can be influenced by a variety of parameters like functional groups, molecular weight, thermal conditions and more.[307-309]

While most thermoplastic polymers show a convenient technical processability, they also have a limited mechanical performance. This can be explained by the molecular nature of thermoplastics. Those are composed of loose single macromolecular chains without covalent bondings amongst them. The macromolecules rather interact in a physical or electrostatical manner via van der Waals forces, dipole interactions or hydrogen bondings.[4][306, 310]

In case of synthetic biopolymers including PCL, PLA as well as associated copolymers and blends [236, 311-313], significant creep strains by applying external forces have been observed. Especially under wet conditions as it is the case during TE and medical approaches, water molecules may diffuse into the polymer's bulk and act as plasticizer leading to distinctly reduced Young's moduli for instance.[314-316] In order to increase creep resistance and maintain the mechanical properties under these conditions, covalent crosslinking of the macromolecules has been proven as effective method.[317]

---

[4] The resulting mechanical tensile behaviour of PCL was demonstrated in **Mechanical testing** on page 123ff and is therefore not further discussed.

Using this approach, the loose macromolecular chains assemble into an interconnected supramolecular network. As a result, advanced entropy-elastic properties can emerge with (almost) no structural defects or cracks at high elongation ratios.[318] Common energy-elasticity of polymers is based on increase of internal energy of chemical bonds. Here, an increase in atomic distance and changes in valence bond angles in the so called elastic energy state at $T < T_g$ are associated with brittle material behaviour. Unlike this, the entropy-elasticity is enabled by the flexibility of the macromolecules and their ability for reversible orientation processes accompanying a reduction of entropy when deformed under the so-called elastic entropy application range at $T > T_g$. Here, the crosslinking of the macromolecular architecture fosters short relaxation times of deformed molecules while the viscous nature becomes reduced and irreversible plastic flow processes are mainly prevented.[298]

Owing to these mechanical characteristics, such elastomeric polymers are highly considered for mechanically demanding TE applications[319] like treating of load bearing soft connective tissue defects. Those comprise tendons and ligaments for instance, exhibiting only a low self-repair capacity.[320] While the required high tensile strength and stress recovery at high deformation rates could be achieved by crosslinking, the qualitative stress-strain behaviour with its naturally occurring *toe region*[321] might be mimicked by superior scaffold design using AM. However, to process crosslinked polymeric TE scaffolds via MEW, a thermoplastic precursor material is essential that can be crosslinked in a post processing step. During the exposure to heat and pressure in the melt reservoir, a minimum of crosslinking reactions is desired. Further, the melt jet and deposited fibres should solidify quickly, enabling the dimensional stability of printed scaffolds which still exhibit thermoplastic material characteristics.

6.2 Experimental section

6.2.1 Polymer

The polymers used in the present study were synthesised, characterised and provided by Dr. Fei Chen and Prof. Dr. Brian Amsden from Department of Chemical Engineering and Human Mobility Research Centre, Queen's University, Kingston, Canada.

Table 8: Different copolymers and corresponding material characteristics.[322]

Target mol. ratio (LLA/CL/AC)	Actual mol. ratio (LLA/CL/AC)	M_n (SEC), $gmol^{-1}$	Đ (SEC)	T_g, °C	T_m, °C
70/15/15	70/18/12	22600	1.6	22	108
65/25/10	60/31/9	21000	1.8	10	87
0/90/10	0/93/7	23600	1.5	-51	53

The synthesis and analysis of poly(L-lactide-*co*-ε-caprolactone-*co*-acryloyl carbonate) (p(LLA-ε-CL-AC)) has been described elswhere[322], the necessary data for this study is presented in Table 8.

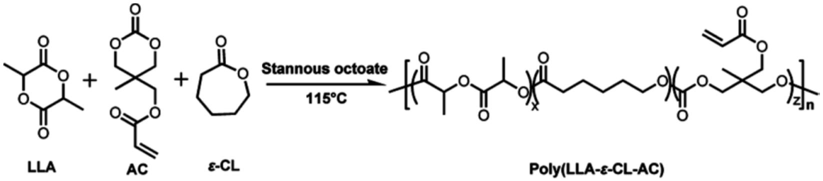

Figure 55: Schematic of the ROP synthesis of p(LLA-ε-CL-AC) and resulting polymer repetition unit.[322]
(Image by Dr. Fei Chen, reprint, Copyright © 2016, American Chemical Society)

In order to enable cross-linking of the vinyl functionalities of the acryloyl carbonates (see polymer product in Figure 55), 1.0 wt.% of the relative thermally stable UV initiator 2,2-Dimethoxy-2-phenylacetophenone (DMPA, Irgacure 651, Sigma-Aldrich, St. Louis, USA), a molecule that can undergo a Norrish Type I photolysis to provide radicals[323, 324], was added to the polymer. This solid raw substance was mixed with Dichloromethane at a ratio of 1.0 gml^{-1} and homogenised by mechanical vortexing. Afterwards, the solvent was evaporated using a fume hood under exclusion of light radiation. The resulting polymer-initiator blend was cut and mixed again.

In the **Results and discussion** section starting at page 141, the p(ε-CL-AC) with a target molecular ratio ε-CL:AC of 90:10 is referred as PCLAC. The p(LLA-ε-CL-AC) polymer with a target molecular ratio LLA:ε-CL:AC of 65:25:10 is referred as PLACLAC. GMP grade PCL was used as reference material and purchased from Corbion Inc. (CAS# 24980-41-4, PURASORB PC 12, Gorinchem, Netherlands).

6.2.2 MEW device

The **High-precision MEW device**, as already introduced on page 112f, has been used for printability testing, deposition of non-linear fibre patterns and manufacturing of scaffolds.

6.2.3 Manufacturing conditions

First of all, the processability of the different copolymers was investigated in general. Therefore, the temperature was increased stepwise ($\Delta T = +5$ °C) until a homogenous and continuous jet could be obtained. During heating, N_2 purge was established to minimise a potential adverse effect of environmental O_2 in the polymer melts. While the spinneret temperature T_2 was optimised for stable and homogeneous MEW printing, the reservoir temperature T_1 was minimised (schematic in Figure 56).

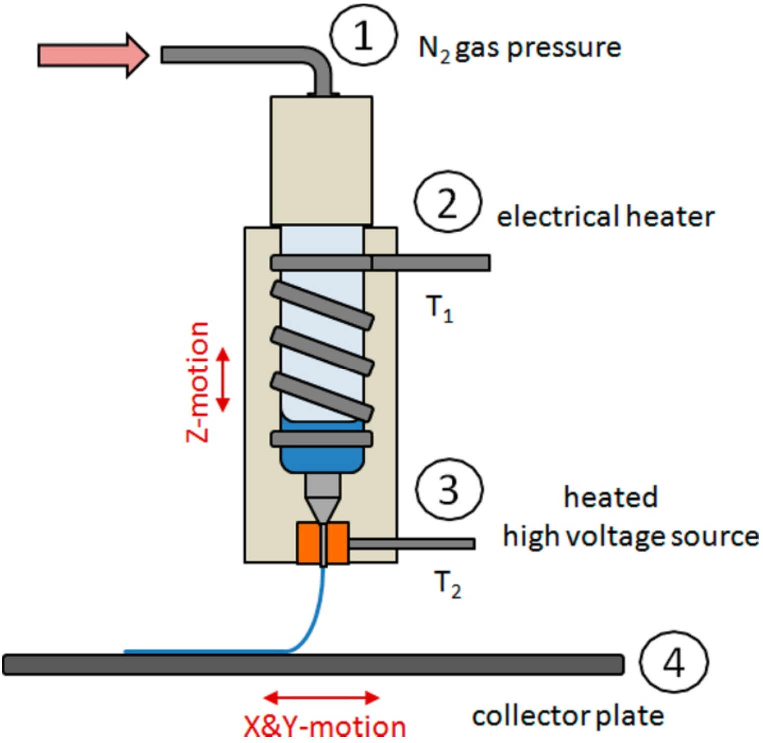

Figure 56: Schematic of the precision MEW device. 1) N_2-gas assisted melt feeder; 2) electrical reservoir heater with temperature T_1; 3) electrical heated HV electrode with temperature T_2; 4) grounded aluminium collector plate moved by ball-screw axes. While T_2 can be adjusted to optimise for a homogenous jet, T_1 can be regulated for minimal thermal polymer damage.[322]
(Reprint, Copyright © 2016, American Chemical Society)

In order to explore stable printing, 30 G spinnerets with an acceleration voltage of U = 7.0 kV at a spinning distance of h = 4.5 mm were utilised. As collector surface, glass slides coated with indium tin oxide for electrical conduction (ITO coated glass, 50 x 50 mm^2, Adafruit industries, New York, USA) were mounted on the collector plate by an aluminium tape. For CTS and fibre diameter investigation, the pressure was varied in five steps consisting p = 0.3, 0.5, 1.0, 2.0 and 4.0 bar.

In order to meet the requirements of the polymer batches, single fibres and scaffolds were manufactured using different processing parameters. Thus, information is provided in the figure description.

The study was performed at room temperature 21 ± 2 °C and an environmental humidity of 35 ± 15 % r.h. All of the measured values include the standard deviation of a sample (SD), as already presented on page 58.

6.2.4 G-code programming

Line arrays were programmed using progressively increasing collector speeds with $\Delta s_c = 12$ and $30\ \mathrm{mm \cdot min^{-1}}$. For each specific pressure, a line array was printed until matching CTS (Figure 57). The line array printing was repeated until the processability of the polymers ceased with n = 5. The entire experiment was reproduced with n = 2 for PLACLAC and n = 4 for PCLAC. Scaffold manufacturing was conducted using different G-code files with individual mesh widths, collector speeds and amounts of layers. The actual information is shown in the figure description.

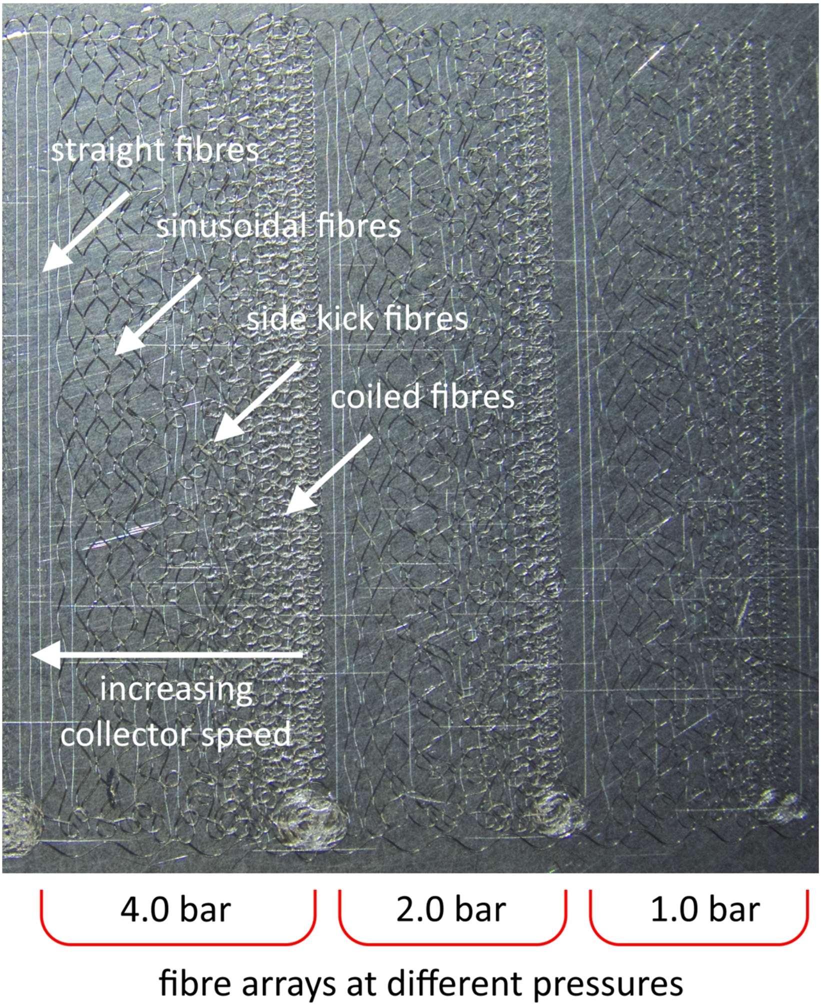

Figure 57: Photography of printed line arrays as example. PLACLAC was printed at different feeding pressures. The collector speed was increased progressively until CTS was matched. First, coiled deposition patterns could be observed changing into straight lines finally.

6.2.5 Post processing

The UV-curing for photo-initiated crosslinking of printed PCLAC scaffolds for mechanical and biological investigation was conducted using a UV light-emitting diodes device (Bluepoint, Dr. Hönle AG, Gräfelfing, Germany). A distance of 5 cm with 130 Wcm^{-2} at 300 to 600 nm wavelength was used for irradiation at different positions for 2 s each ten times. By this treatment, the entire surface of every sample was irradiated for 20 s in total.

6.2.6 Optical imaging

For fibre morphology characterisation of PCLAC below CTS, n = 5 line arrays were printed and quantified using n = 8 measurements of peak-to-peak value and wavelength similar to the procedure described in **Optical analysis** on page 115f. In addition to this, light microscopy and SEM images were taken as discussed beforehand.

For mechanical testing, single fibres were measured at n = 5 different spots in diameter by light microscopy. Due to the roughly elliptic shape of single fibres, SEM measurements were performed of cut fibre profiles as well to estimate the initial cross section properly. Further, the initial length of a sample was prepared to 3.0 mm, however, each fibre was measured additionally for determination of correct mechanical results later.

Single fibres printed below CTS in line arrays are denoted according to the additional fibre length compared to straight lines. This means, a sinusoidal fibre with 3.0 mm length in the crimped state, but with 3.3 mm stretched length was termed “sinus 10 %”. The measuring was conducted via line drawing through the centre of the fibres using the open source software ImageJ.

6.2.7 Mechanical testing

For mechanical testing of single fibres, a low-force tensile tester (ElectroForce® 5500, Bose Corporation, Framingham, USA) with a 250 gram load cell was utilised. Discussed considerations regarding tensile testing from the chapter **Mechanical testing** on page 115ff are valid in this chapter as well. A testing speed of 0.05 mms^{-1} was used stopping the measurement immediately at the point of sudden rupture. In addition, sinusoidal and straight patterned scaffolds were tested with and without cyclic preloading at 10 % strain and 1 Hz oscillation frequency for 10^4 testing cycles.

In order to avoid structural damage during preparation, the fibres were wetted by ethanol, detached from the glass slides and dried at environmental conditions. The single fibres were mounted on cardboard frames and fixed via superglue. After inserting into the tester, the paper frame was cut.

6.2.8 Cytocompatibility testing

The following tests were performed and evaluated by Carina Blum. In order to screen a potential cytotoxic material characteristic, an eluate test based on DIN EN ISO 10993-5, -12 was conducted using L929 CC1 murine fibroblasts (ATCC, Rockeville, USA) derived from a cell line. Here, a scaffold/eluate ratio of 0.1 gml^{-1} was used. The scaffolds were treated as membrane material according to the standard. Hence, PCL reference scaffolds with m = 0.080 g and PCLAC scaffolds with m = 0.078 g were immersed in 850 µl medium, each consisting of DMEM F-12 +1 Vol.% Pen/Strep and +10 Vol.% FCS (all chemicals derived from Gibco, Thermo Fisher Scientific Inc., Waltham, USA). The sterilisation procedure was performed using 70 Vol.% ethanol in H_2O followed by three washing cycles in phosphate-buffered saline. As control, PVC (polyvinylchloride) platelets

(Vekoplan KT PVC PLATTEN König GmbH, Wendelstein, Germany) and polystyrene (PS) culture dishes (Nunc GmbH & Co. KG, Wiesbaden, Germany) were utilised. Further, resulting cell number, absorbance and activity per cell for PS were set to 100 % as reference of the tested PCL and PCLAC. Here, a cell number of 100 % equalled $4.2 \cdot 10^5$ cells.

One day before usage, a concentration of 50000 cells per ml (200 µl each sample) were ceeded into wellplates. After 1 DIV, eluate concentrations of 100 %, 50 % and 25 % were used as culture medium, in case of PS and PVC 100 % eluate only. All samples were tested with n = 3. Following 2 DIV of incubation at 37 °C and 5 % CO_2 in humidified atmosphere (90 % confluent cells in T75 flasks), analysis of cell viability using assay WST-1 and cell counting via CASY 1 TCC (Schärfe System, Roche GmbH, Mannheim, Germany) was performed according to supplier's SOP.

For basic cell adhesion and live/dead-staining (LIVE/DEAD® Viability/Cytotoxicity Kit, for mammalian cells, Thermo Fisher Scientific Inc., Waltham, USA), hMSCs were used, as already introduced in **Cell adhesion experiments** on page 93f and according to supplier's SOP. After 1, 7 and 14 DIV fluorescence microscopy was conducted.

6.3 Results and discussion

The first copolymer p(LLA-ε-CL-AC) with 70/15/15 exhibited no spinnability up to a heating temperature of $T_1 = T_2 = 180$ °C under the discussed conditions. Thus, p(LLA-ε-CL-AC) 65/25/10 and p(ε-CL-AC) 0/90/10 are simply referred as PLACLAC and PCLAC, and separately discussed as well as compared in the subsequent chapters.

6.3.1 MEW processing of PLACLAC

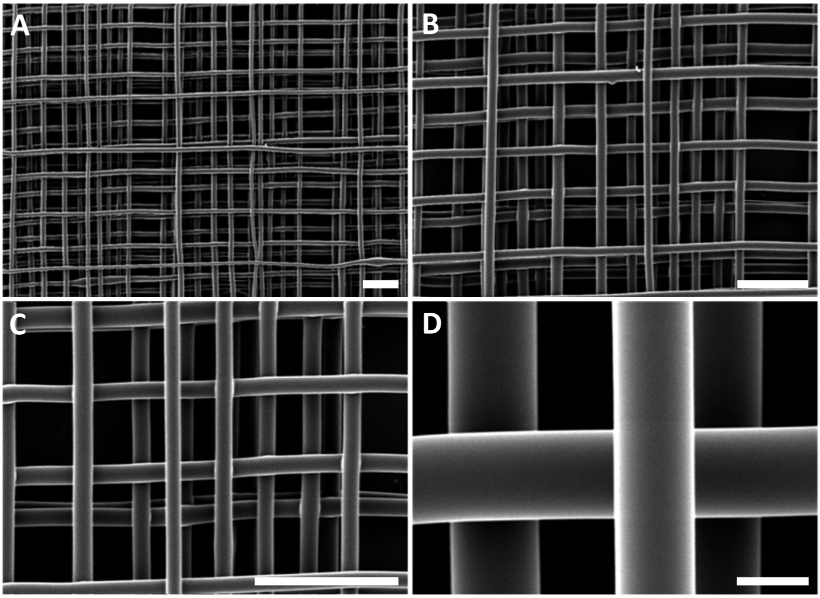

Figure 58: SEM images of a scaffold made of PLACLAC. In total 40 layers (20 in 0° and 20 in 90° direction) were printed with mesh width 100 µm and a feeding pressure of p = 3.0 bar. No accurate stacking could be observed as it occurs in case of PCL printing. This can be attributed to an excessive charge repulsion between the impinging jet and the deposited fibres. While the exact conditions of this phenomenon remain unclear, it can be assumed that charge density and/or charge storage behaviour of this PLACLAC polymer may be significantly increased compared to pure PCL. A,B,C) scale bar = 200 µm and D) scale bar = 20 µm. Conditions are presented in the original research article.[322]
(Image by Dr. Fei Chen, reprint, Copyright © 2016, American Chemical Society)

In order to generate a homogenous and stable MEW jet without breakage, a spinneret temperature of T_2 = 145 °C was established. The reservoir temperature could be decreased to T_1 = 130 °C for minimised heat exposure of the PLACLAC melt without a visible loss in printing performance. In Figure 58, a scaffold manufactured at p = 3.0 bar is presented.

While the SEM images prove the processability of fibres with stable diameters basically, accurate stacking as it occurred in case of PCL was not feasible using PLACLAC under studied conditions. Here, a mesh width of 100 µm was programmed using a ball-screw axis system with an accuracy ≤ 2.0 µm and a repeatability of ≤ 1.0 µm. Nevertheless, the actual fibre distances varied in a broad range preventing the deposition of highly defined scaffold architectures. It could be observed that no single fibre stacked on top of another indicating a strong repulsing effect presumably by significant charge density and/or storage behaviour of the PLACLAC polymer.

When spending attention to the correlation between feeding pressure and jet speed, another significant difference between PLACLAC and pure PCL turned out. As also shown in detail later in Figure 59, the CTS clearly depended on the utilised feeding pressure. While $p = 0.3$ bar led to a peak value of $510 < \text{CTS} < 540\ \text{mm}\cdot\text{min}^{-1}$, $p = 4.0$ bar led to even a maximum of $780 < \text{CTS} < 810\ \text{mm}\cdot\text{min}^{-1}$.

This PLACLAC polymer characteristic of increasing jet speed at increasing feeding pressures is invasively valid for PCL showing a reduced CTS at increased feeding pressures (comparison to Figure 25 on page 63).This phenomenon cannot be easily explained by an increased melt infeed through the spinneret only. A simple mathematical assumption supports this, considering the fibre deposition volume flow rate with an estimated cylindrical shape of a fibre segment printed at $p = 4.0$ bar with approximately $f\text{Ø} = 50\ \mu\text{m}$ and $\text{CTS} = 800\ \text{mm}\cdot\text{min}^{-1}$:[325]

$$\frac{dV_3}{dt} = A_f \cdot CTS = \left(\frac{f\text{Ø}}{2}\right)^2 \cdot \pi \cdot \frac{\varDelta l_f}{\varDelta t_f} =$$

$$= \left(\frac{50 \cdot 10^{-3}\, mm}{2}\right)^2 \cdot \pi \cdot 800 \frac{mm}{min} \approx 1.6 \frac{mm^3}{min}$$

dV_3/dt = volume rate of deposited fibres; A_f = fibre cross-section; CTS = critical translation speed, fØ = fibre diameter; l_f = fibre segment length, t_f = time to print fibre segment

As defined in **Considerations on MEW** on page 59f, a conservation of masses can be assumed. In order to roughly estimate the average melt speed $\hat{v}_1$ through the spinneret with IØ: 30 G ≈ 160 µm, a laminar flow pattern and a density changes of 10 % from molten to solid state has been assumed:[325]

$$\hat{v}_1 = \frac{dV_1}{dt} \cdot \frac{1.1}{\pi \cdot r^2} = \frac{1.1 \cdot 1.6 mm^3}{\pi \cdot \left(\frac{160 \cdot 10^{-3} mm}{2}\right)^2 min} \approx 90 \frac{mm}{min}$$

dV_1/dt = volume rate through spinneret; r = inner diameter of the spinneret;
$\hat{v}_1$ = average melt flow speed through the spinneret

Indeed, this simple calculation bears a certain error by the assumptions made, nevertheless, the scale of outcome can help for processing estimations. Here, $\hat{v} \approx 90$ mm·min^{-1} at p = 4.0 bar feeding pressure indicated further effects causing the CTS difference of ΔCTS = 270 mm·min^{-1} between p = 0.3 bar and p = 4.0 bar. Moreover, pure PCL jets decrease significantly in CTS, although the melt infeed speed increases.

While the exact physical reason for the different rheological behaviour remains speculative, explanation attempts may be found by spending attention to the difference in the (potentially improved) charge and shear-thinning behaviour of PLACLAC. While printed fibres exhibited a strong repulsion and showed no stacking as discussed priorly (in contrast to PCL), higher Coulomb interactions by increased charge injection in the MEW *Taylor Cone* or jet may be concluded, which may have led to a stronger acceleration in the electrical field supporting a fast jet at high feeding pressures. However, electrorheological phenomena are highly complex problems which cannot be explained simply by a few experiments.

Furthermore, the polymer's shear-thinning properties could have influenced the flow behaviour and speed of the EHD jet as well. Basically, the viscosities of polymer melts tend to decrease significantly at increased shear rates (compare Figure 10 on page 20). A faster melt feed through the spinneret enforced by higher pressures may also have resulted in increased shear-thinning and thus, a reduced viscosity of the melt. Given that partially aligned macromolecules cannot (fully) relax after leaving the spinneret and entering the *Taylor Cone*, a lowered flow resistance in the jet may have resulted. However, the extensional viscosity of stretched p(LLA-ε-CL-AC) at high strain ratios in the jet is unknown and cannot be measured easily.

Further, in general an increased melt infeed might also remove potential yield stresses by shorter residual times at the *Taylor Cone* etc. If this or similar effects have had an influence on the discussed experiments remains unclear due to the lack of understanding of charge injection, trapping, transport and dissipation finally as interaction with EHD-driven polymer acceleration combined with EHD quenching and flow induced crystallisation solidification.

Nevertheless, the dimension of the apparent shear rate, the maximum shear rate emerging at the spinneret wall, can be appraised by a simple approach using the Rabinowitsch correction for shear-thinning fluids assuming a common power-law index of $n_{pl} = 0.4$:[326]

$$\frac{d\gamma_{ap}}{dt} = \frac{3 \cdot n_{pl} + 1}{4 \cdot n_{pl}} \cdot \frac{dV_1}{dt} \cdot \frac{4}{\pi \cdot r^3} = \frac{5.5 \cdot 1.8 mm^3}{\pi \cdot \left(\frac{160 \cdot 10^{-3} mm}{2}\right)^3 min} \approx 100 \frac{1}{s}$$

dV_1/dt = volume rate through spinneret; r = inner diameter of the spinneret;

$\hat{v}_1$ = average melt flow speed through the spinneret; n_{pl} = power-law index

Like the calculations before, this estimation may exhibit errors as the equation is a simplification neglecting pipe roughness, potential temperature gradients etc. The extrusion of macromolecular and thus, viscoelastic polymer melts through a spinneret or pipe is a complicated process. However, the calculation is an indicator. The small sized 30 G spinneret determined the average shear rate clearly with a dependency of $\sim r^{-3}$ resulting in $d\gamma_{ap}/dt \approx 100\ s^{-1}$ at p = 4.0 bar having a potential impact since AM melt extrusion techniques process at a typical range of $d\gamma/dt = 100\text{-}200\ s^{-1}$ (as discussed in **The rheological limits of polymer extrusion** on page 18ff).

Beside the increasing CTS with increasing feeding pressure, other phenomena could be observed differentiating PLACLAC's printing behaviour from PCL. Also shown in Figure 59, the CTS changed significantly over processing time, given as normalised time; with $t_{norm} = 1.0$ the processability ceased. While the CTS was small at the beginning at $0.01 \leq t_{norm} \leq 0.05$ with $135 \leq CTS \leq 315\ mm \cdot min^{-1}$, the heating of the polymer melt was not completed explaining the relatively small jet speeds.

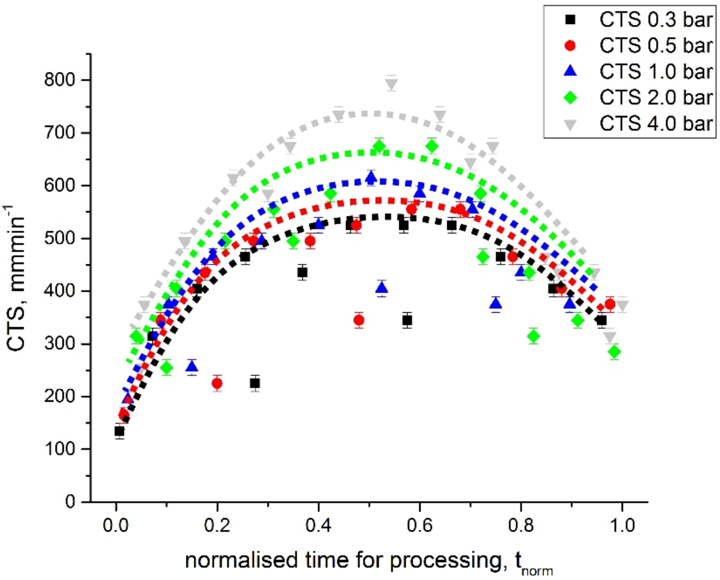

Figure 59: CTS as function of the feeding pressure and processing time of PLACLAC. The time is presented as normalised time until crosslinking occurred in the melt reservoir accompanied by ceased printability. Implemented lines visualise the progress of CTS. Here, an increasing feeding pressure led to an increased CTS. Further, the CTS evolved over time having a maximum at roughly $0.5 < t_{norm} < 0.7$ in the figure. The dashed lines illustrate the trend of one single experiment. Presented outliers were collected from the repetition of the experiment and basically follow the same trend with deviated values.[327]
(Published under Creative Commons licence CC BY-NC-ND 4.0)

Subsequently, the CTS-t_{norm} function evolved to a maximum at $0.5 < t_{norm} < 0.7$ with $525 \leq CTS \leq 795$ mm·min^{-1}, followed by a gradual decrease again. The spinnability ceased with $345 \leq CTS \leq 375$ mm·min^{-1}, this can be explained by undesired crosslinking of the melt in the cavity at elevated temperatures.

Beside the time-dependent CTS-changes, additional changes in the fibre diameter were observed. While the uncompleted heating of the polymer melt, leading to increased fibre diameter sizes, is reflected in Figure 60 until roughly

$t_{norm} \leq 0.3$ as well, a plateau-like zone at $0.3 < t_{norm} < 0.7$ occurred independently to the feeding pressure. Afterwards at $t_{norm} \geq 0.7$ the fibre diameter dropped again until spinnability ceased.

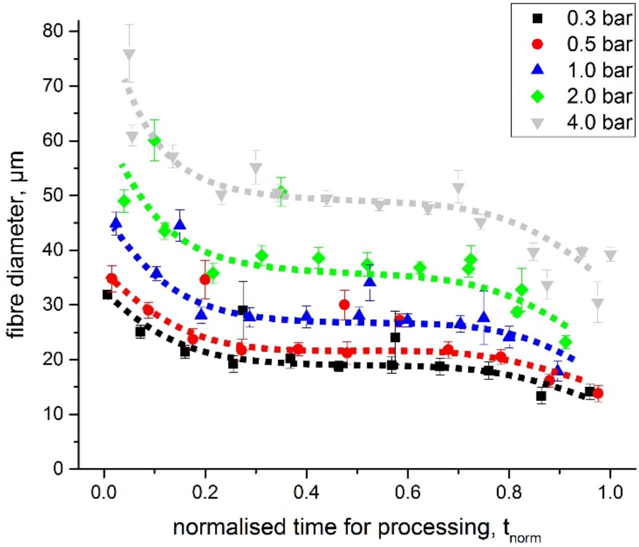

Figure 60: Fibre diameter as function of the feeding pressure and processing time of PLACLAC. The time is presented as normalised time until crosslinking occurred in the melt reservoir accompanied by ceased printability. Implemented lines visualise the progress of the fibre diameter, increased pressures led to increased fibre diameters as it could be expected. While the fibre diameter decreased over time, a plateau-like behaviour was observed for all feeding pressures between roughly $0.3 < t_{norm} < 0.7$*. The dashed lines illustrate the trend of one single experiment. Presented outliers were collected from the repetition of the experiment and basically follow the same trend with deviated values.[327]*
(Published under Creative Commons licence CC BY-NC-ND 4.0)

When spending attention to the low fibre diameters combined with the low CTS at $0.7 \leq t_{norm} < 1.0$, a small volume or mass flow rate through the spinneret could be concluded. This can be explained by considering the Hagen-Poiseuille equation (see formula *(1)* on page 18); an increased viscosity by an increased molecular weight resulted in small throughputs.

While the progress of cross-linking raised questions, viscosity changes or resulting molecular weights at different points of time were not further quantified due to the low relevance of a polymer melt with a total life time of only $t = 1.4 \pm 0.7$ h. When estimating an almost stable printing characteristic of PLACLAC between $0.3 < t_{norm} < 0.7$, not more than $t = 0.6 \pm 0.3$ h remained for reliable MEW processing. Nevertheless, **the beneficial mechanical characteristics of the polymer could be proven by Dr. Fei Chen.** Even under hydrated conditions and after 10,000 cycles of load with 10 % tensile strain, scaffolds made of PLACLAC exhibited relevant mechanical characteristics (a Young's modulus of $E = 370 \pm 166$ MPa for instance). More tests including details and explanations are presented in [322].

6.3.2 MEW processing of PCLAC

Using the spinnability testing with $\Delta T = +5$ °C steps for the PCLAC revealed a clearly decreased necessary minimum heating temperature. A spinneret temperature of $T_2 = 105$ °C and a reservoir temperature of $T_1 = 90$ °C already led to stable MEW printing (Figure 61). While the molecular weights were virtually similar with $M_n = 21000\ gmol^{-1}$ including $Đ = 1.8$ for PLACLAC and $M_n = 23600\ gmol^{-1}$ including $Đ = 1.5$ for PCLAC, the latter formed constant jets at $\Delta T = -40$ °C. As discussed in **Polycaprolactone** on page 49ff, this can be attributed to the 90 mol.%-content of low melting point $T_m \approx 60$ °C of PCL leading to a $T_m = 53$ °C of PCLAC. In contrast to this, PLLA with a high melting point of $T_m \approx 180$ °C represented the majority with 65 mol.% in PLACLAC exhibiting a $T_m = 87$ °C.

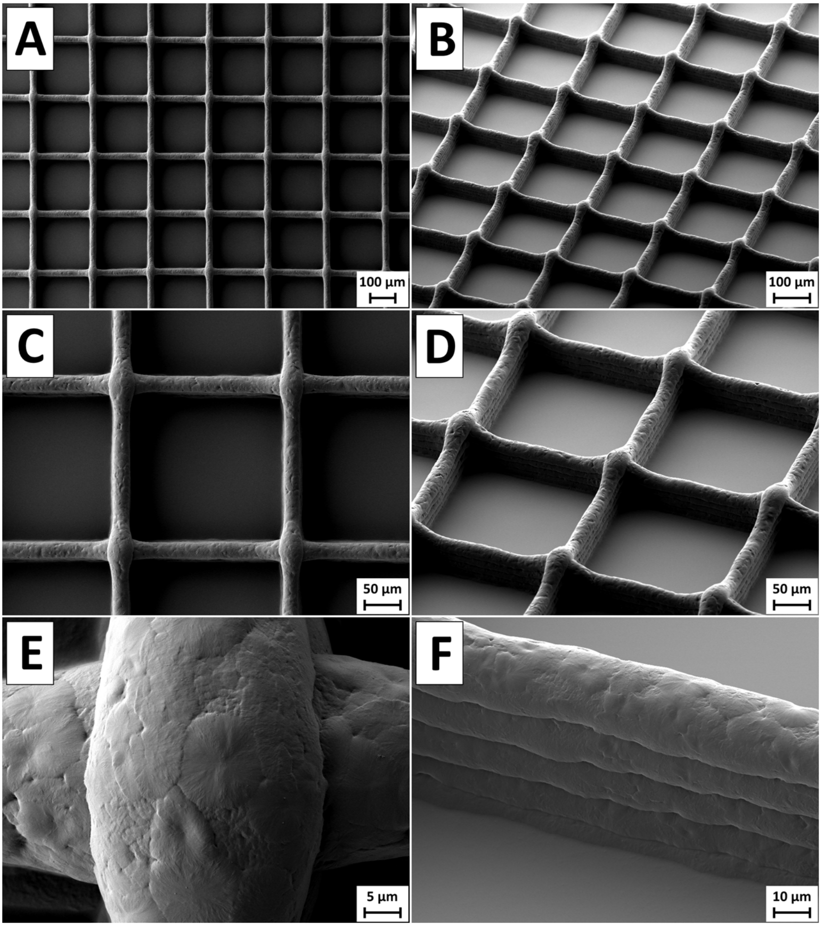

Figure 61: SEM images of a scaffold made of PCLAC. In total 10 layers (5 in 0° and 5 in 90° direction) were printed with mesh width of 200 µm and a feeding pressure of p = 1.0 bar (other parameters as described). A-D) the overview images show the accurate macroscopic structure. E&F) The surface exhibited spherulites, a typical super-ordinated morphology characteristic of semi-crystalline polymers. In contrast to the LLA-containing polymer PLACLAC, the PCLAC fibres can be stacked accurately. This enabled direct writing in a controlled manner. As shown in F), the initial layer touching the collector surface seemed to be strongly deformed. This observation is of interest and shown later again by the single fibre experiments.[327]
(Image by Dr. Claus Moseke, published under Creative Commons licence CC BY-NC-ND 4.0)

In contrast to PLACLAC, the polymer PCLAC exhibited an excellent stacking behaviour at the minimum spinning temperature, making it a reasonable choice for MEW printing of highly defined scaffolds. Another difference could be observed by spending attention to the surface morphology. PLACLAC's surface appeared smooth on the micro-scale, whereas PCLAC formed distinct structures indicating crystallisation processes. (Figure 61 E&F). Here, especially spherulites were observed. These are super-ordinated structures with roughly round or polygonal shapes often occurring when polymer melts with the ability to (partially) crystallise are cooled below T_m.[328, 329] As result, fibrillar crystals grow radially from the centred nucleus by chain-folding, naturally surrounded by residual amorphous phases, until the crystal growth becomes inhibited sterically.

Besides morphological aspects, PCLAC comprised also differences in the printing behaviour. The CTS-t_{norm} functions (Figure 62) indicated a similar behaviour to PLACLAC including cross-linking finally, except two important differences. First of all, the CTS peak values with $195 \leq CTS \leq 264$ mm·min^{-1} can be found at earlier relative times with $0.2 < t_{norm} < 0.4$, while the total processing time of $t = 13 \pm 7$ h at $p = 4.0$ bar increased substantially. Considering similar polymer heating performance for PLACLAC, the peak of the normalised time of PCLAC was shifted to lower values consequently.

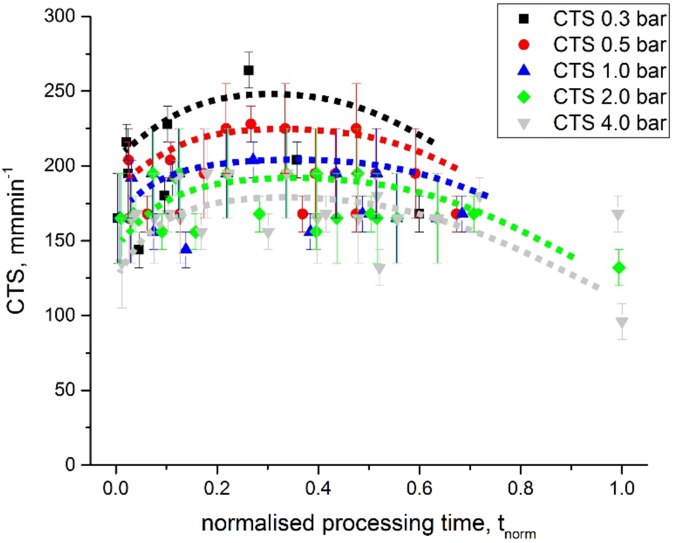

Figure 62: CTS as function of the feeding pressure and processing time of PCLAC. The time is presented as normalised time until crosslinking occurred in the melt reservoir accompanied by ceased printability. Implemented lines visualise the progress of CTS. Higher feeding pressures led to lower jet speeds. A maximised CTS was observed at $0.2 < t_{norm} < 0.4$. The dashed lines illustrate the trend of one single experiment. Presented outliers were collected from the repetition of the experiment and basically follow the same trend with deviated values.[327] (Published under Creative Commons licence CC BY-NC-ND 4.0)

However, more important is the second observation. Here, the jet speed decreased with increasing feeding pressures indicating a more similar printing behaviour of PCLAC to PCL than to PLACLAC (comparison Figure 63 and Figure 25 on page 63). However, if this is a result of the missing LLA-content in the polymer or the decreased minimum heating temperature is not finally clear and subject of ongoing research.

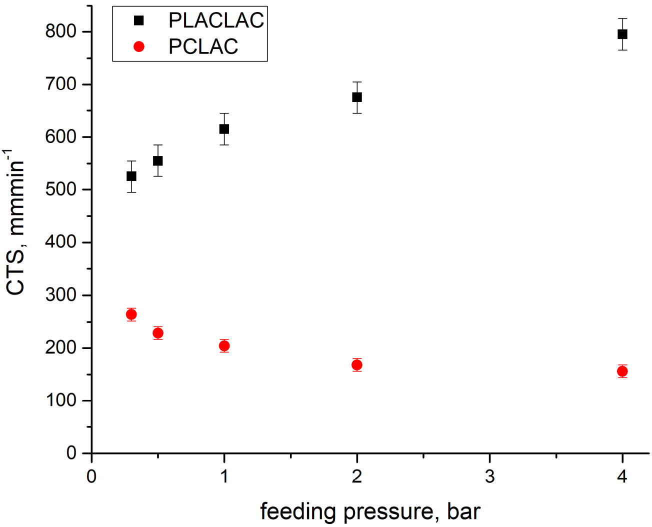

Figure 63: CTS of PLACLAC and PCLAC as function of the feeding pressure. The peak values of the CTS-t_{norm} functions have been chosen for both polymers. While PLACLAC showed an increase in CTS at raising pressures, the CTS of PCLAC decreased.

As presented in Figure 64, the fibre diameters increased strongly with raising feeding pressures. Here, a broad variation from p = 0.3 bar with fØ ≈ 20 µm to p = 4.0 bar with fØ ≈ 55 µm was adjustable. Supported by the increased processing time, a difference between low and high feeding pressures turned out. At $t_{norm} > 0.6$ fibres could not be processed at p = 0.3 bar anymore followed by p = 0.5 bar and p = 1.0 bar at roughly $t_{norm} > 0.7$. Only p = 2.0 bar and p = 4.0 bar led to fibre printing until $t_{norm} \approx 1.0$. However, fibre diameter instabilities became frequent close to $t_{norm} = 1.0$ as reflected by the SD in Figure 64.

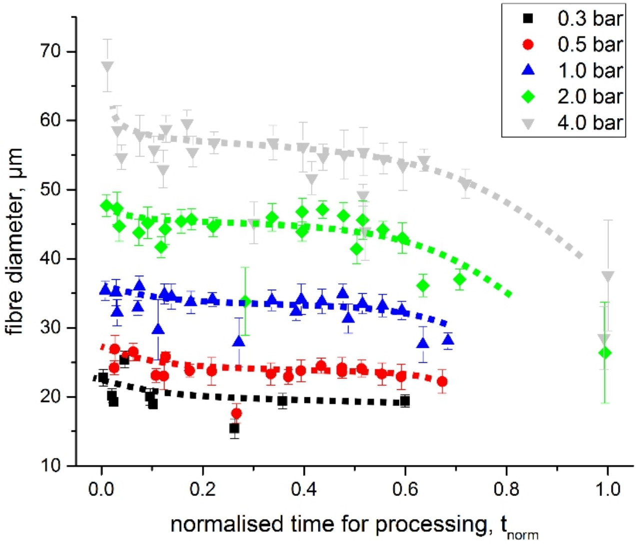

Figure 64: Fibre diameter as function of the feeding pressure and processing time of PCLAC. The time is presented as normalised time until crosslinking occurred in the melt reservoir accompanied by ceased printability. Implemented lines visualise the progress of the fibre diameter, increasing pressures led to increasing fibre diameter as expected. While the fibre diameter decreased over time, a plateau-like behaviour was observed for all feeding pressures between roughly $0.1 < t_{norm} < 0.6$. The dashed lines illustrate the trend of one single experiment. Presented outliers were collected from the repetition of the experiment and basically follow the same trend with deviated values.[327]
(Published under Creative Commons licence CC BY-NC-ND 4.0)

Thus, it seems to be practical to manufacture scaffolds at elevated pressures, if possible and in accordance with the desired fibre diameter. Using the PCLAC polymer, scaffolds could be processed under stable conditions at $0.1 < t_{norm} < 0.6$ and for a total time of $t = 7 \pm 4$ h respectively. Nevertheless, the inconvenient CV ≈ 50 % (Figure 65) of processing times until crosslinking shows the poor reproducibility from batch to batch. However, PCLAC showed a clearly advanced MEW processing performance in contrast to PLACLAC.

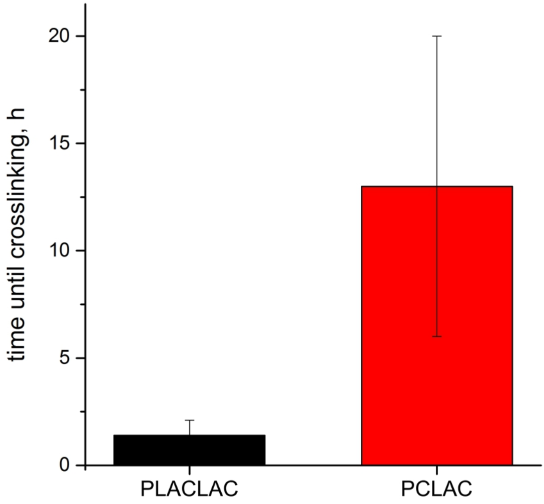

Figure 65: Processing time at the relative minimum heating temperature for PLACLAC and PCLAC until cross-linking in the melt reservoir. The time frame is presented starting from the very beginning of processing until the polymers are not printable anymore using high feeding pressures $p = 4.0$ bar. While PCLAC's processing time was increased about an order of magnitude, the CV ≈ 50 % of both polymers was high.

Evidently, the processing time could be increased about one order of magnitude and a beneficial stacking behaviour made PCLAC a proper candidate for further mechanical and biological investigations.

6.3.3 Printing of PCLAC below CTS

Similar to **MEW printed patterns below CTS** of PCL on page 117, the printing performance of PCLAC regarding sinusoidal meanders was investigated. Here, the aim was to mimic the specific load-bearing characteristic of natural tissue, like tendons or ligaments. Therefore, the tensile performance was taken into account, at the beginning of the deformation, the Young's modulus has to be rather small (so-called *toe region*[330]) but increasing strongly after approximately 1 – 3 % tensile strain.

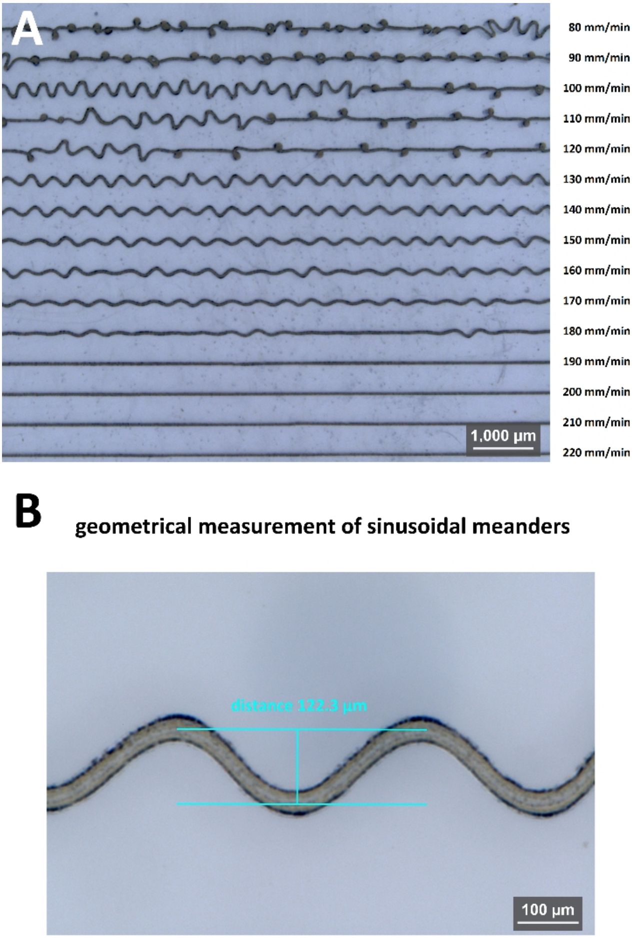

Figure 66: Microscopy image of a line array of PCLAC fibres at different collector speeds. A) Straight lines were printed at a collector speed of $180 < s_c = CTS \leq 190$ mm·min^{-1}. Below CTS, sinusoidal meanders and side kicks (finally) could be observed analogously to PCL printing. B) Elucidation of the geometrical measurement of non-linear patterns. The colour was inverted to increase the visibility. Feeding pressure was set to $p = 1.0$bar.[327]
(Published under Creative Commons licence CC BY-NC-ND 4.0)

Such a behaviour of natural tissue can be attributed to its morphology; a sinusoidal or uniaxially crimped ECM mainly composed of a triple helical collagen type I structure[331, 332] to bear mechanical load and elastin for a proper stress relaxation performance.[333] However, MEW printing of PCLAC below CTS resulted, identically to PCL (compare page 120), in sinusoids with the opportunity to adjust wavelengths and peak-to-peak values. As illustrated in Figure 66 A, straight lines were printed above > 180 mm·min^{-1}, while sinusoidal meanders were deposited at collector speeds of $180 \geq s_c > 120$ mm·min^{-1}. Figure 66 B illustrates the procedure of geometrical quantification.

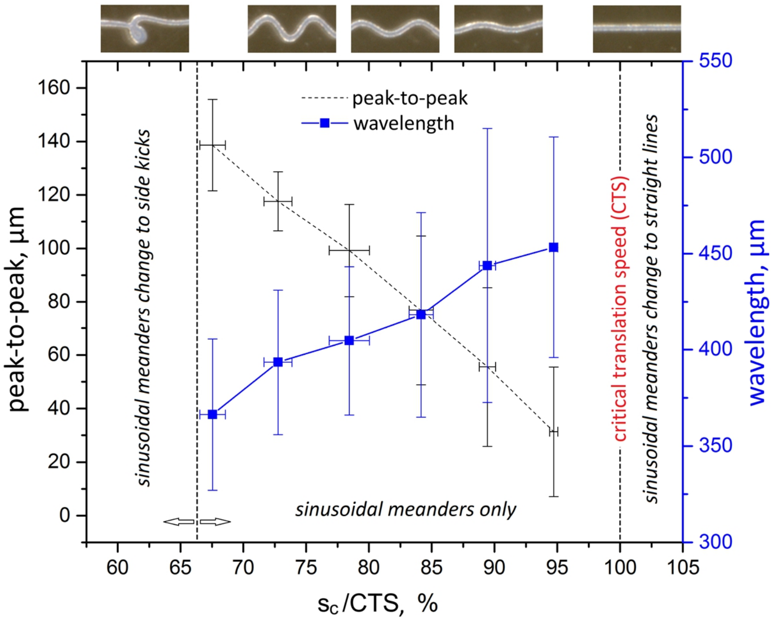

Figure 67: Quantified geometry of sinusoidal structure elements using PCLAC as function of the collector speed. While the sinusoidal peak-to-peak value increased at decreasing relative collector speeds (s_C divided by CTS in %), the wavelength increased meanwhile. The relatively high SD of the values can be explained by the repetition n = 5 with batch to batch changes, however, a distinct trend could be observed during every single experiment.[327]
(Published under Creative Commons licence CC BY-NC-ND 4.0)

Further, the total determination of wavelength and peak-to-peak value is presented in Figure 67, elucidating the dependency of the shape and the relative collector speed. Under the studied conditions, sinusoids were printed at 100 > CTS > 67 %, with peak-to-peak values ranging from approximately 30 µm to 140 µm at wavelengths of 450 µm to 370 µm and fibre diameters of fØ ≈ 30 µm (quantified and discussed later). This extensive adjustability of the peak-to-peak values enabled a specific tailoring of the thermoplastic precursor polymer patterns. Post-curing via UV-initiated radical cross-linking maintained the pattern only and did not lead to significant deformation of fibres, allowing to study the mechanical behaviour of the deposited single sinusoids.

6.3.4 Mechanical testing of sinusoidal PCLAC fibres

In order to prevent mechanical fibre damage during preparation, cardboard frames were utilised for single fibre orientation and fixation (Figure 68).

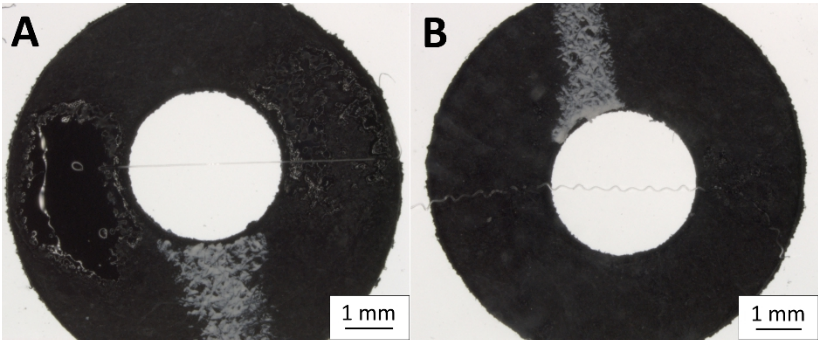

Figure 68: Microscopic images of cardboard frames for preparation of mechanical testing of single fibres. A) Straight fibre printed at CTS, B) sinusoidal fibre with additional 20 % material elongation printed at roughly 0.75 x CTS.[327]
(Published under Creative Commons licence CC BY-NC-ND 4.0)

Using this approach, accurate fibre length examination could be conducted. In addition to this, a fibre cross-section determination was necessary as the fibres have shown an approximately elliptic profile (Figure 69) with a distinct deviation from a circular shape. This could be observed only for monolayers directly in contact with the collector surface and not for those on top of already deposited fibres interestingly.

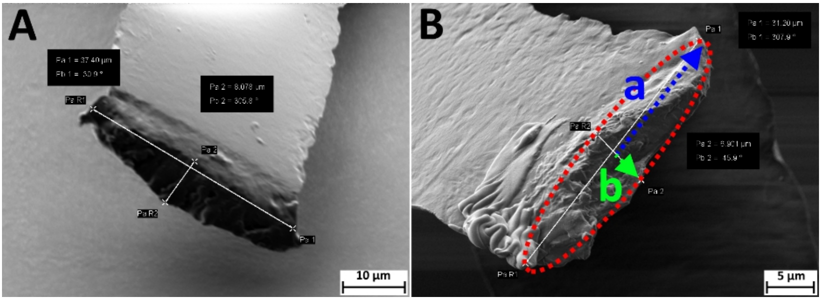

Figure 69: SEM images of single fibre cross sections. A roughly elliptic fibre profile has been assumed, considering the half-axes a and b.[327]
(Image by Dr. Claus Moseke, published under Creative Commons licence CC BY-NC-ND 4.0)

However, a conservative assumption was made regarding the ratio between the ellipse half-axes 4b = a with the aim, to provide credible results for mechanical testing. While a comparatively small error was assumed during quantification of the fibre half-axis a using a sufficient number of microscopy images, actual SEM measurements of half-axis b revealed values of 5b ≈ a. Due to expected angular deviations during SEM quantification of tilted single fibre cross-sections and fibre defects, the assumption 4 b = a leading to $A_0 = 1/4 \pi a^2$[334] seemed to be reasonable.

Figure 70 presents the tensile mechanical behaviour of differently shaped sinusoidal single fibres systematically printed below CTS in comparison to straight fibres printed at CTS. First of all, a clearly advanced maximum tensile strength of the PCLAC fibres could be observed with $\sigma_{max} = 53 \pm 16$ MPa ($\approx \sigma_u$) compared to PCL with σ_{max} = 20 ± 3 MPa (fØ ≈ 20 µm), taken from the prior chapter **Mechanical testing** on page 123ff. Here, single fibres are compared to scaffolds which indeed may exhibit errors. However, the fibre diameters were roughly similar (elliptic single fibres with a ≈ 15 µm, hence b ≈ 15/4 µm compared to circular fibres with r ≈ 10 µm) and thus, the vast difference confirmed the benefit of a cross-linked system.

Downsides, the straight PCLAC fibres revealed an ultimate strain of ε_u = 90 ± 12 % until rupture. This can be considered as sufficient characteristic itself, but compared with PCL's ε_u = 600 %[299], this is rather low due to the missing (extraordinary) plastic macromolecular flow processes under mechanical load.

As shown in Figure 70, at 0 to 2 % strain an E = 314 ± 157 MPa for straight fibres, E = 79 ± 14 MPa for sinus 10 ± 1 % fibres and only E = 29 ± 17 MPa for sinus 13 ± 1 % could be observed. While the Young's moduli of straight fibres only decreased at higher strains as expectable (summarised in Table 9), the stiffness for the sinusoidal fibres increased significantly at 2 to 5 % strain with E = 137 ± 14 MPa for sinus 10 ± 1 % fibres and E = 41 ± 6 MPa for sinus 13 ± 1 . At strains of 5 to 10 %, E = 200 ± 1 MPa for sinus 10 ± 1 % and E = 111 ± 53 MPa for sinus 13 ± 1 % were measured.

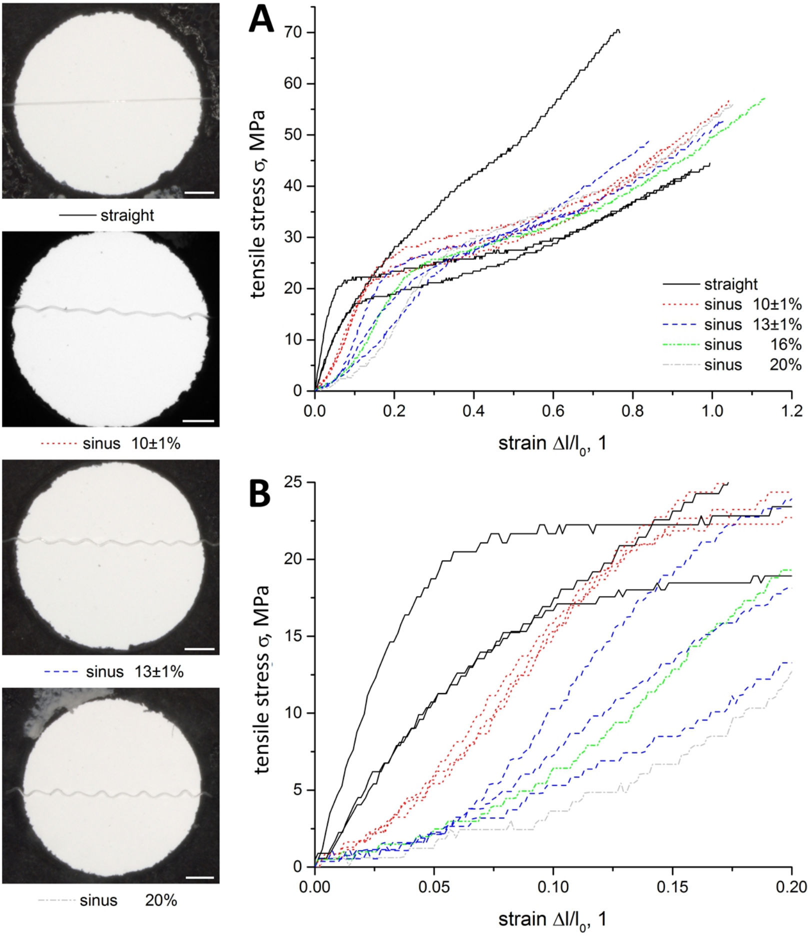

Figure 70: Tensile Stress-strain functions of single fibres with different sinusoidal patterns. A) Overview figure comprising the stress-strain behaviour until fracture. B) Illustration of the close-range area until 20 % strain. A distinct toe region was observed at testing sinusoidal shaped fibres. Here, sinusoidal patterns with increased peak-to-peak values led to significantly decreased Young's moduli at small strains. Scale bar = 500 µm.[327]
(Published under Creative Commons licence CC BY-NC-ND 4.0)

On one hand, significant mechanical differences between sinus 10 ± 1 % and sinus 13 ± 1 % at small strains were observed showing the sensitive dependency of sinusoidal patterns and resulting tensile performance. On the other hand, the results proved the adjustability of the *toe region* at the desired small range of strain ≈2-4 % to mimic the tensile behaviour of tendons and ligaments.[335, 336] However, when comparing the resulting maximum tensile strength and ultimate strain to rupture of straight and sinusoidal fibres, no significant differences can be observed.

Table 9: Summary of the tensile characteristics of the differently patterned single fibres. Values are given as arithmetic average ± SD.[327]

	Straight	**Sinus 10±1 %**	**Sinus 13±1 %**
E(0-2 %), MPa	314 ± 157	79 ± 14	29 ± 17
E(2-5 %), MPa	232 ± 51	137 ± 14	41 ± 6
E(5-10 %), MPa	99 ± 41	200 ± 1	111 ± 53
σ_{max}, MPa	53 ± 16	51 ± 5	46 ± 9
ε_u, 1	0.90 ± 0.12	0.95 ± 0.09	0.86 ± 0.17

6.3.5 Mechanical testing of sinusoidal PCLAC scaffolds

In order to use the observed beneficial sinusoidal features for scaffold processing, further MEW printing experiments were conducted. As discussed beforehand, the CTS changes complicate the defined printing of reproducible scaffolds with sinusoidal patterns substantially. Nevertheless, scaffolds with 6 layers, 3 layers in 0° and 3 layers in 90° direction, could be manufactured properly (Table 10). Therefore, modified instrumental parameters had to be used: U = 5.5 kV and p = 4.0 bar.

Table 10: Fibre diameter quantification of PCLAC scaffolds.Measured fibre diameters were similar, nevertheless, fibre diameter fluctuations were observed. The scaffolds are presented in Figure 71.

	Scaffold A	Scaffold B	Scaffold C	Scaffold D
Average, µm	28.4	28.8	28.6	28.6
SD, µm	3.9	3.5	3.6	3.6
CV, %	13.7	12.2	12.6	12.6

As presented in Figure 71, such scaffolds were processed as proof, providing sinusoidal fibre patterns in one direction and straight fibres in another as support structure. While the sinusoidal fibres were deposited with programmed 300 µm of mesh width, only every 10 mm straight fibres were deposited as crossing struts. Thereby, highly uniaxial but coherent scaffolds could be manufactured.

Like the single fibres, the corresponding sinusoidal and straight patterned scaffolds have been subject of mechanical analysis. Here, tensile testing of samples was performed with and without 10^4 cycles of mechanical preload (10 % strain, 1 Hz) as basic proof for entropy-elasticity or cycle fatigue respectively.

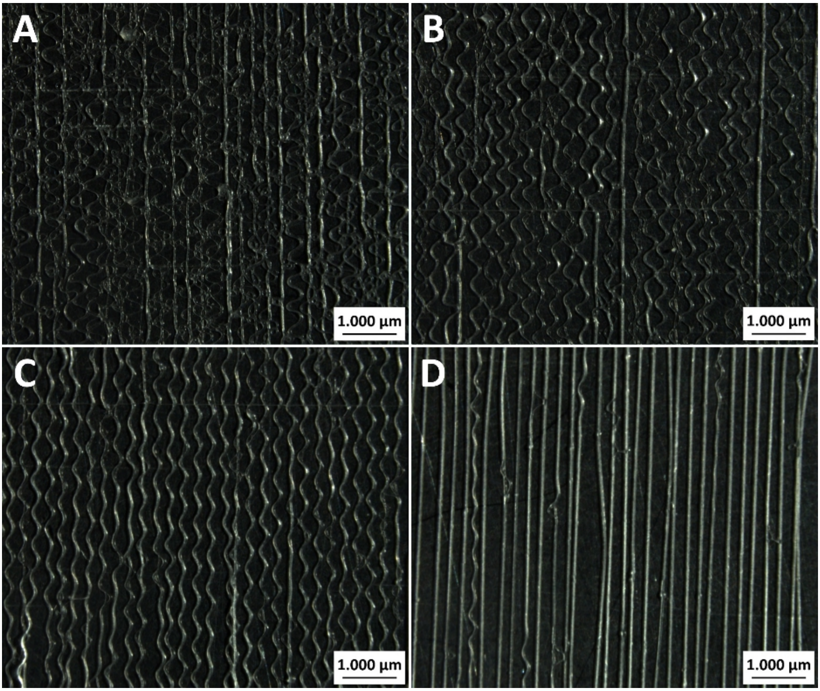

Figure 71: Microscopy images of uniaxial scaffolds printing using PCLAC below CTS. As discussed, the CTS changed over the processing time. As result, scaffolds with different morphological patterns occurred. A) Mixture of side kicks and sinusoids, B) Mainly sinusoids, C) sinusoids only and finally D) straight lines predominantly. The scaffolds have been MEW printed at $U = 5.5$ kV and $p = 4.0$ bar, other parameters as described.[327]
(Published under Creative Commons licence CC BY-NC-ND 4.0)

In order to determine the cross-section A_0 for mechanical calculations, the diameters of the fibre stacks with sinusoidal and straight features (both sample types $n = 3$) were analysed using light microscopy with $n = 10$ measurements each. Based on SEM measurements (examples in Figure 72), a halved elliptic shape was assumed with a fibre stack height of 1.5 fØ leading to an initial cross-section of $A_0 = 3/8\ \text{fØ}^2\ \pi$.

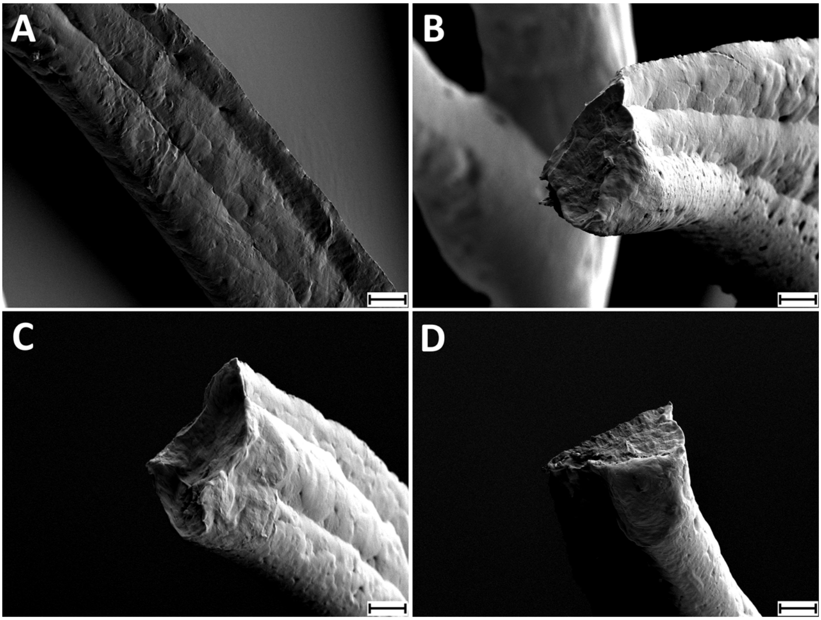

Figure 72: SEM images of fibre stacks of PCLAC scaffolds with 3 layers in tensile testing direction. The SEM images were examined for analysis of the fibre stack cross-section. Further, the surface exhibited pores between the sperulites which can be considered as mechanical weak spots. A) Image of stacked fibres, B-D) example cross-sections. Scale bar = 10 µm.[327]
(Image by Dr. Claus Moseke, published under Creative Commons licence CC BY-NC-ND 4.0)

As presented in Figure 73, the cross-linked PCLAC scaffolds exhibited improved mechanical characteristics similar to the corresponding single fibres. Indeed, the maximum tensile strength and the stiffness of the scaffolds was reduced, however, this can be attributed to different phenomena during preparation and mechanical testing.

While it is feasible to orient a single fibre along the tensile direction with precision in general, a certain amount of fibres of a scaffold might not be perfectly in line with the pulling forces at the beginning of the mechanical testing. This may have led to decreased Young's moduli. Further, some fibres of the scaffold broke earlier during testing than others resulting in a reduced maximum strength as the detected force was divided by the starting area cross-section A_0. This circumstance is reflected in Figure 73, sudden drops in stress indicated fibre ruptures.

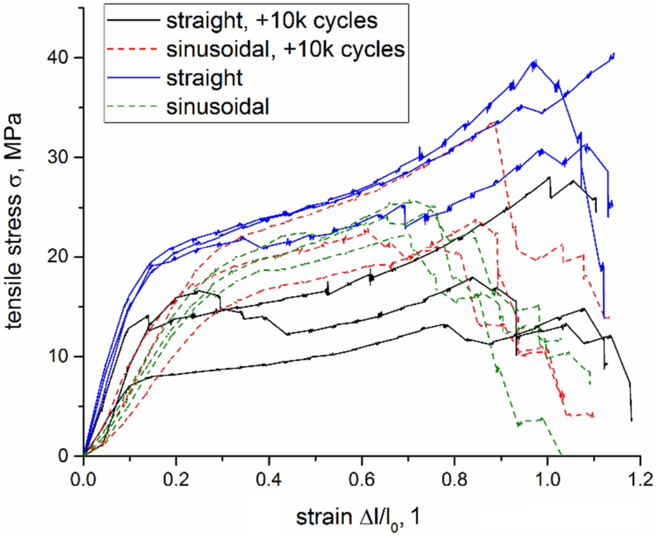

Figure 73: Tensile Stress-strain functions of scaffolds with sinusoidal and straight patterns. Similar to the single fibres, the Young's moduli as slopes of the functions were clearly higher in case of straight fibre patterns. In contrast, the sinusoidal scaffolds exhibited a toe region. Further, the preloading with 10^4 cycles at 1 Hz and 10 % strain led to significantly decreased mechanical properties in case of straight scaffolds only. However, the results confirmed the improved mechanical fatigue resistance compared to thermoplastic polymer systems.[327] (Published under Creative Commons licence CC BY-NC-ND 4.0)

In addition, the relatively high CV = 12.6 % for both fibre diameters of the sinusoidal and straight patterned scaffolds reduced the mechanical values further. While the average fibre diameter is used for calculations, fibres break at the weakest spots since the mechanical stress effects the whole volume during tensile loading. Here, a thinned section of a *pulsed* fibre for example has a reduced cross-section area and is therefore prone to rupture at this weak spot.

Despite these problems, the mechanical characteristics of straight deposited PCLAC polymer with σ_{max} = 37 ± 5 MPa still exceeded those of PCL respectively (σ_{max} = 20 ± 3 MPa) as quantified in the prior chapter **Mechanical testing** on page 123ff.

Table 11: Summary of the tensile characteristics of the differently patterned scaffolds. Values are given as arithmetic average ± SD.[327]

	Straight	Sinusoidal
	Without preload	
E(1-3 %), MPa	170 ± 29	42 ± 16
σ_{max}, MPa	37 ± 5	24 ± 2
	With preload; 10^4 cycles, 10 %, 1 Hz	
E(1-3 %), MPa	75 ± 51	47 ± 25
σ_{max}, MPa	20 ± 7	26 ± 7

When comparing the mechanical results of sinusoidal and the straight patterned scaffolds without preload, distinct differences can be concluded (summarised in Table 11). First of all, straight patterns revealed a clearly increased Young's modulus of E = 170 ± 29 MPa and maximum tensile strength of σ_{max} = 37 ± 5 MPa compared to sinusoidal structured scaffolds with E = 42 ± 16 MPa and σ_{max} = 24 ± 2 MPa. While the decreased stiffness can be understood as desired proof of the desired *toe region,* the decreased strength was not favourable, however, not lower than the PCL reference material.

Interestingly, the sinusoidal scaffold's mechanical performance was not noticeable diminished by the cyclic preloading. Here, testing resulted in $\sigma_{max} = 24 \pm 2$ MPa / $E = 42 \pm 16$ MPa without and $\sigma_{max} = 26 \pm 2$ MPa / $E = 47 \pm 25$ MPa with preloading conditions. In contrast, the straight scaffold's mechanical characteristics decreased clearly with $\sigma_{max} = 37 \pm 5$ MPa / $E = 170 \pm 29$ MPa with and $\sigma_{max} = 20 \pm 7$ MPa / $E = 75 \pm 51$ MPa without preloading.

The observed material fatigue in case of straight patterns can be explained by the 10 % pure material strain, including conformational change in the polymer, during 10^4 cycles of preloading. These may have led to molecular scission, plastic deformation or polymer flow and crack initiation ultimately. On the contrary, the sinusoidal patterns may have acted as "buffer zone" for material stretching as they deformed to straight lines during the first percentages of strain first, subsequently followed by more and more material stretching. Hence, sinusoidal fibres were less subjected to pure material deformation and stress than straight fibres at a similar tensile strain.

Nevertheless, shear and tensile tension must have occurred in the polymer mainly leading to reversible macromolecular orientation during deformation from sinusoidal to straight lines. Consequently, sinusoidal shaping of the cross-linked PCLAC fibres of MEW printed scaffolds exhibited further improved the mechanical performance regarding cycle fatigue. Here, a potential advantage for load bearing TE applications and concerning biomechanical mimicking scaffolds stands to reason.

6.3.6 Cytocompatibility of PCLAC scaffolds

Cell seeding, analysis of the WST-1 assay and fluorescence microscopy in this subchapter was performed by Carina Blum.

In order to investigate a potential cytotoxic influence, MEW printed PCLAC with 1.0wt.% I651 UV-initiator was studied *in vitro* utilising a WST-1 assay with L929 murine fibroblasts over 2 DIV incubation of scaffolds in DMEM as first test. As illustrated in Figure 74, the generated eluate had, in all cases, no adverse influence on cell number, cell viability or activity. Here, cells cultured on pure PS were used as 100 % reference value.

Table 12: Cell number, absorbance and activity of the WST-1 assay using L929 murine fibroblast.

	Cell number, 10^3 ml^{-1}	**Absorbance, a. u.**	**Activity per cell, a. u.**
PS	418.9 ± 18.8	0.218 ± 0.020	26.0 ± 2.7
PVC	1.4 ± 0.3	0 ± 0	0 ± 0
100 % PCLAC	405.3 ± 22.8	0.186 ± 0.019	22.9 ± 2.6
50 % PCLAC	469.4 ± 23.2	0.210 ± 0.022	22.4 ± 2.6
25 % PCLAC	494.3 ± 25.7	0.249 ± 0.004	24.1 ± 1.3
100 % PCL	437.7 ± 33.5	0.196 ± 0.021	22.4 ± 3.0
50 % PCL	500.4 ± 77.7	0.220 ± 0.028	22.0 ± 4.4
25 % PCL	521.3 ± 5.6	0.272 ± 0.066	26.1 ± 6.4

The results of the WST-1 assay are further summarised in Table 12. Indeed, I651 is known as strongly cytotoxic UV-initiator[337, 338], nevertheless, after photolysis and covalent bonding to the π-bond of the vinyl functionality from the AC, the initiator's cytotoxic influence was prevented or strongly reduced at least.

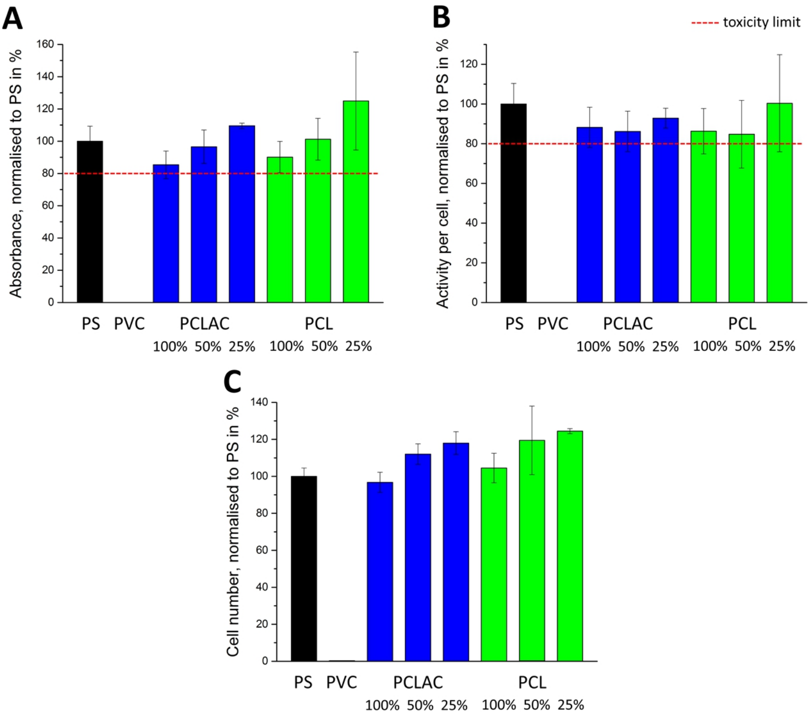

Figure 74: WST-1 eluate assay of PCLAC and PCL for cell viability analysis. As reference and control material, PS and PVC have been used. Neither A) Absorbance or B) activity per cell, nor C) cell number of L929 murine fibroblasts were affected adversely. Here, all of the eluates with 100%, 50% or 25% concentration and all of the samples, whether PCL or PCLAC including 1.wt.% of the UV-initiator I651, exhibited values above the standard toxicity limit of 80 % compared to pure PS with 100 %. Thus, the cross-linked system PCLAC can be considered as non-cytotoxic material at the first glance.[327]
(Published under Creative Commons licence CC BY-NC-ND 4.0)

The second test, a live/dead staining of hMSCs adherent to PCLAC fibres including initiator (shown in Figure 75), revealed a promising biomaterial performance as well. After 1 DIV, the cells started to adhere, occurring as partially alive (green) and partially dead (red). After 7 DIV, a vital and dense cell layer formed exhibiting a stretched cell appearance. No clear difference between 7 and

14 DIV could be observed, however, lifting the scaffolds in the cell culture confirmed the suitable adherence to the scaffold only and preclude a potential adherence to the substrate.

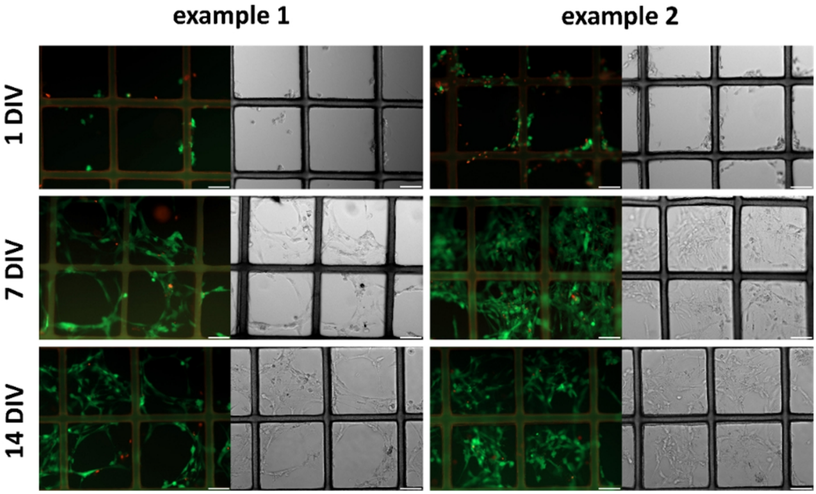

Figure 75: Fluorescence microscopy images of a live/dead staining of hMSCs on PCLAC scaffolds after 1, 7 and 14 DIV by two representative example. A green colour staining indicated living, a red one dead cells. After 1 DIV, initial cell adhesion was observed, living and dead cells were in balance. After 7DIV, a clear proliferation occurred leading to a dense cell layer adherent to the scaffold. Much more living cells were present, with a partially stretched appearance. After 14 DIV not much difference was detected compared to 7 DIV. Scale bar = 100 µm.[327]
(Image by Carina Blum, published under Creative Commons licence CC BY-NC-ND 4.0)

Nonetheless, neither cell viability, nor live/dead staining can be considered as full proof for biocompatibility. Whether cells are damaged or rather their receptors and desoxyribonucleic-acids are manipulated by potential cytotoxic degradation products containing reacted I651 etc. is not clear yet. Further, the penetration depth of the UV-light into the fibres remains uncertain, a potential release of non-reacted I651 during degradation should be investigated consequently.

To overcome issues regarding cytotoxic UV-initiators completely, cross-linking reactions of thermoplastic pre-polymers for MEW must be taken into account without usage of I651.

6.4 Conclusion

In this study, PLACLAC and PCLAC copolymers, were successfully printed by MEW. To enable reproducible manufacturing, the processing behaviour was studied and assessed comparatively. In contrast to other polymers available for MEW, the presented thermoplastics can be cross-linked in a post-processing step leading to formation of mechanically improved fibres with a maximum tensile strength of σ_{max} = 53 ± 16 MPa, a Young's modulus of E = 314 ± 157 MPa at a ultimate strain of ε_u = 90 ± 12 % until rupture.

Additionally, systematic printing of PCLAC to sinusoidal fibres comprised of different geometries revealed the opportunity to tailor the tensile stress-strain function largely at small deformations (< 10 % strain). The presented patterns resemble the naturally occurring crimped morphology of load-bearing soft tissues like tendon or ligaments and further mimic the corresponding mechanical behaviour qualitatively.

The presented straight and sinusoidal structure features were further successfully used to print uniaxially optimised scaffolds. In addition, tensile testing was conducted with and without a cyclic preload (10^4 cycles, 1 Hz, 10 % strain). The results confirmed both, the possibility to print tailored scaffolds with the desired *toe region* and a significantly advanced mechanical performance.

Furthermore, cell viability according to the relevant standard, as well as hMSC adhesion on scaffolds including live/dead assays revealed a promising biomaterial characteristic of PCLAC. Hence, to manufacture cytocompatible, high-strength, high elastic and fatigue resistant scaffolds with biomimetic stress-strain-characteristics via MEW turned out as a highly promising approach for ligaments and tendon repair.

7 Summary

In order to mimic the extracellular matrix for tissue engineering, recent research approaches often involve 3D printing or electrospinning of fibres to scaffolds as cell carrier material. Within this thesis, a micron fibre printing process, called melt electrospinning writing (MEW), combining both additive manufacturing and electrospinning, has been investigated and improved. Thus, a unique device was developed for accurate process control and manufacturing of high quality constructs. Thereby, different studies could be conducted in order to understand the electrohydrodynamic printing behaviour of different medically relevant thermoplastics as well as to characterise the influence of MEW on the resulting scaffold performance.

For reproducible scaffold printing, a commonly occurring processing instability was investigated and defined as *pulsing*, or in extreme cases as *long beading*. Here, processing analysis could be performed with the aim to overcome those instabilities and prevent the resulting manufacturing issues. Two different biocompatible polymers were utilised for this study: poly(ε-caprolactone) (PCL) as the only material available for MEW until then and poly(2-ethyl-2-oxazoline) for the first time. A hypothesis including the dependency of *pulsing* regarding involved mass flows regulated by the feeding pressure and the electrical field strength could be presented. Further, a guide via fibre diameter quantification was established to assess and accomplish high quality printing of scaffolds for subsequent research tasks.

By following a combined approach including small sized spinnerets, small flow rates and high field strengths, PCL fibres with submicron-sized fibre diameters (fØ = 817 ± 165 nm) were deposited to defined scaffolds. The resulting material characteristics could be investigated regarding molecular orientation and morphological aspects. Thereby, an alignment and isotropic crystallinity was observed that can be attributed to the distinct acceleration of the solidifying jet in the electrical field and by the collector uptake. Resulting submicron fibres formed accurate but mechanically sensitive structures requiring further preparation for a suitable use in cell biology. To overcome this handling issue, a coating procedure, by using hydrophilic and cross-linkable star-shaped molecules for preparing fibre adhesive but cell repellent collector surfaces, was used.

Printing PCL fibre patterns below the critical translation speed (CTS) revealed the opportunity to manufacture sinusoidal shaped fibres analogously to those observed using purely viscous fluids falling on a moving belt. No significant influence of the high voltage field during MEW processing could be observed on the buckling phenomenon. A study on the sinusoidal geometry revealed increasing peak-to-peak values and decreasing wavelengths as a function of decreasing collector speeds s_c between $\text{CTS} > s_c \geq 2/3\ \text{CTS}$ independent of feeding pressures. Resulting scaffolds printed at 100 %, 90 %, 80 % and 70 % of CTS exhibited significantly different tensile properties, foremost regarding Young's moduli ($E = 42 \pm 7$ MPa to 173 ± 22 MPa at 1 – 3 % strain). As known from literature, a changed morphology and mechanical environment can impact cell performance substantially leading to a new opportunity of tailoring TE scaffolds.

Further, poly(L-lactide-*co*-ε-caprolactone-*co*-acryloyl carbonate) as well as poly(ε-caprolactone-*co*-acryloyl carbonate) (PCLAC) copolymers could be used for MEW printing. Those exhibit the opportunity for UV-initiated radical cross-linking in a post-processing step leading to significantly increased mechanical characteristics. Here, single fibres of the polymer composed of 90 mol.% CL and 10 mol.% AC showed a considerable maximum tensile strength of $\sigma_{max} = 53 \pm 16$ MPa. Furthermore, sinusoidal meanders made of PCLAC yielded a specific tensile stress-strain characteristic mimicking the qualitative behaviour of tendons or ligaments. Cell viability by L929 murine fibroblasts and live/dead staining with human mesenchymal stem cells revealed a promising biomaterial behaviour pointing out MEW printed PCLAC scaffolds as promising choice for medical repair of load-bearing soft tissue.

Indeed, one apparent drawback, the small throughput similar to other AM methods, may still prevent MEW's industrial application yet. However, ongoing research focusses on enlargement of manufacturing speed with the clear perspective of relevant improvement. Thereby, the utilisation of large spinneret sizes may enable printing of high volume rates, while downsizing the resulting fibre diameter via electrical field and mechanical stretching by the collector uptake. Using this approach, limitations of FDM by small nozzle sizes could be overcome. Thinking visionary, such printing devices could be placed in hospitals for patient-specific printing-on-demand therapies one day. Taking the evolved high deposition precision combined with the unique small fibre diameter sizes into account, technical processing of high performance membranes, filters or functional surface finishes also stands to reason.

8 Zusammenfassung

Um biomimetische extrazelluläre Matrices für das Tissue Engineering herzustellen, bedienen sich aktuelle Forschungsansätze oftmals der Produktion von Faser-Konstrukten durch additive Fertigung oder Elektrospinn-Verfahren. Das sogenannte Melt Electrospinning Writing (MEW) kombiniert Vorteile beider Techniken und weist dadurch ein hohes Applikationspotential auf. Daher bestand das Ziel der vorliegenden Arbeit in der Weiterentwicklung und Erforschung des MEW. Für diesen Zweck wurde eine neuartige Forschungsanlage konzipiert und gebaut, welche mit einzigartiger Verfahrenspräzision und Prozesskontrolle die Fertigung von hochqualitativen Konstrukten ermöglichte. Auf Basis dessen konnten die durchgeführten Studien das Verständnis des elektrohydrodynamischen Druckvorgangs und der untersuchten Prozessparameter vertiefen und letztendlich zur Ausweitung des Verfahrens auf neue medizinisch relevante Thermoplaste beitragen.

Um eine reproduzierbare Herstellung von Scaffolds zu ermöglichen, wurde eine häufig auftretende Prozessinstabilität erforscht und als *pulsing,* oder in stark ausgeprägten Fällen als *long beading*, klassifiziert. Durch Prozessanalyse konnte zudem eine Methode zur Vermeidung dieser Instabilität entwickelt werden. Dafür wurden zwei unterschiedliche biokompatible Polymere verwendet: Poly(ε-Caprolacton) (PCL) als bis dahin einziger verfügbarer MEW Werkstoff, sowie erstmalig Poly(2-Ethyl-2-Oxazolin). Die aufgestellte Hypothese umfasst eine universelle Abhängigkeit der *pulsing* Instabilität zu involvierten Massenströmen, welche durch Anpassung des angelegten Prozessdruckes und der elektrischen Feldstärke reguliert werden kann. Um ein optimales Prozessergebnis für nachfolgende Forschungsarbeiten zu erzielen, wurde zusätzlich ein Leitfaden zur quantitativen Bewertung des Grades der Instabilität bereitgestellt.

Durch Kombination kleiner Spinndüsen, kleiner Schmelze-Flussraten und hoher elektrischen Feldstärken, konnten erstmalig PCL Fasern mit sub-mikron Durchmessern (fØ = 817 ± 165 nm) zu präzisen Scaffolds verarbeitet werden. Diese wurden anschließend durch materialwissenschaftliche Analytik charakterisiert. Dabei wurde eine molekulare Vorzugsorientierung und isotrope Kristallausrichtung entlang der Faser beobachtet, welche durch den hohen Verstreckungsgrad des erstarrenden Polymerstrahls erklärt werden konnte. Resultierende sub-mikron Fasern konnten zwar für einen akkuraten Druckvorgang verwendet werden, jedoch erwiesen sich die Strukturen als instabil und daher nicht geeignet für die Handhabung bei Zellkulturstudien. Aus diesem Grund wurde ein Beschichtungsansatz mittels hydrophilen und vernetzbaren Sternmolekülen für Substratflächen herangezogen. Während solche modifizierten Oberflächen bekanntermaßen Zelladhäsion verhindern, konnten gedruckte sub-mikron Scaffolds auf der Oberfläche haften und so für biologische Studien verwendet werden.

Durch das gezielte Ablegen von Fasern unterhalb der kritischen Translationsgeschwindigkeit (CTS) des Kollektors, konnten sinusförmige Faserstrukturen erzeugt werden. Analog zu rein viskosen Fluiden, welche durch ein bewegliches Band aufgesammelt werden, schien dieser Vorgang dem sogenannten *buckling* zu unterliegen und daher phänomenologisch nicht oder nur geringfügig vom elektrischen Feld abhängig zu sein. Zudem konnte eine durchgeführte Studie die direkte Abhängigkeit der Fasergeometrie mit der Kollektorbewegung belegen. Unabhängig vom Prozessdruck, führte eine verminderte Kollektorgeschwindigkeit s_c in den Grenzen CTS > s_c ≥ 2/3 CTS zu erhöhten Amplituden bzw. Spitze-zu-Spitze Werten und verkürzten Wellenlängen. Durch das kontrollierte Ablegen der Fasern bei Geschwindigkeiten von 100 %, 90 % 80 % und 70 % CTS konnten zudem Scaffolds mit unterschiedlichen mechanischen Eigenschaften hergestellt werden. Speziell der Zugmodul wurde dadurch etwa um eine halbe Größenordnung moduliert (E_s = 42 ± 7 MPa bis 173 ± 22 MPa bei 1 – 3 % Dehnung). Dies ist in Kombination mit der Strukturierung für maßgeschneiderte TE Scaffolds von großem Interesse, da zelluläre Systeme sensibel auf ihre Umgebung reagieren können.

Des Weiteren wurden Poly(L-Lactid-*co*-ε-Caprolacton-*co*-Acryloylcarbonat) und Poly(ε-Caprolacton-*co*-Acryloylcarbonat) (PCLAC) Copolymere hinsichtlich deren MEW Verarbeitbarkeit untersucht. Solche Kunststoffe können nach dem Druckvorgang mit UV-Strahlung radikalisch vernetzt werden und dadurch deutlich erhöhte mechanische Eigenschaften ausbilden. Für Fasern aus 90 mol.% CL und 10 mol.% AC wurden beispielsweise maximale Zugfestigkeiten von σ_{max} = 53 ± 16 MPa ermittelt. MEW gedruckte sinusförmige Faserstrukturen aus PCLAC wiesen darüber hinaus ein biomimetisches Spannungs-Dehnung-Verhalten auf, vergleichbar zu Sehnen- und Ligamentgewebe. Eine Untersuchung der Zellviabilität von L929 murinen Fibroblasten im Eluattest, sowie eine lebend/tot-Färbung von humanen mesenchymalen Stammzellen auf den Scaffolds, ergab vielversprechende Resultate und damit ein relevantes Anwendungspotential solcher Strukturen als Implantat.

Neben genannten Vorteilen, weist MEW als Verfahren bislang allerdings geringe Produktionsgeschwindigkeiten auf. Diese sind daher in den Fokus aktueller Forschungsvorhaben gerückt. Einen Ansatz hierfür bieten Spinndüsen mit hohem Innendurchmesser und erhöhter Austragsrate, wobei die optimierte elektrische Feldstärke, sowie ein Verstrecken durch die Kollektorbewegung, zu den erwünschten dünnen Fasern führen können. Dadurch kann die abwärtslimitierte Düsengröße des FDM Verfahrens überwunden werden. Visionär gedacht, könnte eine solche Anlage direkt in Krankenhäusern zur Fertigung von patienten- und defektspezifischen Implantaten eingesetzt werden. Darüber hinaus ermöglicht die hohe Präzision, zusammen mit dem Drucken von Mikro-Fasern, einen technischen Einsatz zur Herstellung von Membranen, Filtern oder funktionalen Oberflächenbeschichtungen.

9 References

[1] E.T. Pashuck, M.M. Stevens, Designing regenerative biomaterial therapies for the clinic, Science translational medicine 4(160) (2012) 160sr4.

[2] W.R. Moore, S.E. Graves, G.I. Bain, Synthetic bone graft substitutes, ANZ journal of surgery 71(6) (2001) 354-361.

[3] M.W. Mariscalco, R.A. Magnussen, D. Mehta, T.E. Hewett, D.C. Flanigan, C.C. Kaeding, Autograft Versus Nonirradiated Allograft Tissue for Anterior Cruciate Ligament Reconstruction: A Systematic Review, The American journal of sports medicine 42(2) (2013) 492-499.

[4] J.L. Hudgens, B.P. Gillette, A.J. Krych, M.J. Stuart, J.H. May, B.A. Levy, Allograft versus autograft in posterior cruciate ligament reconstruction: an evidence-based systematic review, Journal of Knee Surgery 26(02) (2013) 109-116.

[5] B.M. Holzapfel, J.C. Reichert, J.-T. Schantz, U. Gbureck, L. Rackwitz, U. Noeth, F. Jakob, M. Rudert, J. Groll, D.W. Hutmacher, How smart do biomaterials need to be? A translational science and clinical point of view, Advanced drug delivery reviews 65(4) (2013) 581-603.

[6] S.J. Hollister, Porous scaffold design for tissue engineering, Nature materials 4(7) (2005) 518-524.

[7] X. Mo, C. Xu, M. Kotaki, S. Ramakrishna, Electrospun P (LLA-CL) nanofiber: a biomimetic extracellular matrix for smooth muscle cell and endothelial cell proliferation, Biomaterials 25(10) (2004) 1883-1890.

[8] T. Jiang, E.J. Carbone, K.W.-H. Lo, C.T. Laurencin, Electrospinning of polymer nanofibers for tissue regeneration, Progress in Polymer Science 46 (2015) 1-24.

[9] P.D. Dalton, C. Vaquette, B.L. Farrugia, T.R. Dargaville, T.D. Brown, D.W. Hutmacher, Electrospinning and additive manufacturing: converging technologies, Biomaterials Science 1(2) (2013) 171-185.

[10] S. Knappe, O. Stachs, A. Zhivov, M. Hovakimyan, R. Guthoff, Results of confocal microscopy examinations after collagen cross-linking with riboflavin and UVA light in patients with progressive keratoconus, Ophthalmologica 225(2) (2011) 95-104.

[11] C. Wei, L. Cai, B. Sonawane, S. Wang, J. Dong, High-precision flexible fabrication of tissue engineering scaffolds using distinct polymers, Biofabrication 4(2) (2012) 025009.

[12] A. Martins, R. Reis, N. Neves, Electrospinning: processing technique for tissue engineering scaffolding, International Materials Reviews 53(5) (2008) 257-274.

[13] W. Lee, H. Rahman, M.E. Kersh, K.C. Toussaint, Application of quantitative second-harmonic generation microscopy to posterior cruciate ligament for crimp analysis studies, Journal of Biomedical Optics 22(4) (2017) 046009.
[14] A. Herchenhan, N.S. Kalson, D.F. Holmes, P. Hill, K.E. Kadler, L. Margetts, Tenocyte contraction induces crimp formation in tendon-like tissue, Biomech Model Mechan 11(3-4) (2012) 449-459.
[15] G.G. Wallace, R. Cornock, C. O'Connell, S. Bernie, S.M. Dodds, F. Gilbert, 3D BioPrinting: Printing parts for bodies (2014).
[16] I. Campbell, D. Bourell, I. Gibson, Additive manufacturing: rapid prototyping comes of age, Rapid Prototyping J 18(4) (2012) 255-258.
[17] J.-P. Kruth, Material incress manufacturing by rapid prototyping techniques, CIRP Annals-Manufacturing Technology 40(2) (1991) 603-614.
[18] J.D. Prince, 3D printing: an industrial revolution, Journal of Electronic Resources in Medical Libraries 11(1) (2014) 39-45.
[19] C.W. Hull, Apparatus for production of three-dimensional objects by stereolithography, U.S. Patent No. 4,575,330, Google Patents, 1986.
[20] T.B. Heller, R.M. Hill, A.F. Saggal, Apparatus for forming a solid three-dimensional article from a liquid medium, U.S. Patent No. 5,071,337, Google Patents, 1991.
[21] G.N. Levy, R. Schindel, J.-P. Kruth, Rapid manufacturing and rapid tooling with layer manufacturing (LM) technologies, state of the art and future perspectives, CIRP Annals-Manufacturing Technology 52(2) (2003) 589-609.
[22] J.-P. Kruth, M.-C. Leu, T. Nakagawa, Progress in additive manufacturing and rapid prototyping, CIRP Annals-Manufacturing Technology 47(2) (1998) 525-540.
[23] G. Bull, J. Groves, The Democratization of Production, Learning & Leading with Technology 37(3) (2009) 36-37.
[24] K.V. Wong, A. Hernandez, A review of additive manufacturing, ISRN Mechanical Engineering 2012 (2012).
[25] M. Vaezi, H. Seitz, S. Yang, A review on 3D micro-additive manufacturing technologies, The International Journal of Advanced Manufacturing Technology 67(5-8) (2013) 1721-1754.
[26] O. Ivanova, C. Williams, T. Campbell, Additive manufacturing (AM) and nanotechnology: promises and challenges, Rapid Prototyping J 19(5) (2013) 353-364.
[27] B. Wendel, D. Rietzel, F. Kühnlein, R. Feulner, G. Hülder, E. Schmachtenberg, Additive processing of polymers, Macromolecular materials and engineering 293(10) (2008) 799-809.

[28] E.C. Santos, M. Shiomi, K. Osakada, T. Laoui, Rapid manufacturing of metal components by laser forming, International Journal of Machine Tools and Manufacture 46(12) (2006) 1459-1468.

[29] J. Deckers, J. Vleugels, J.-P. Kruth, Additive manufacturing of ceramics: A review, J. Ceram. Sci. Technol 5(4) (2014) 245-260.

[30] N. Guo, M.C. Leu, Additive manufacturing: technology, applications and research needs, Frontiers of Mechanical Engineering 8(3) (2013) 215-243.

[31] V. Mironov, G. Prestwich, G. Forgacs, Bioprinting living structures, J. Mater. Chem. 17(20) (2007) 2054-2060.

[32] Standard, ASTM, F2792-12a Standard terminology for additive manufacturing technologies, ASTM International, West Conshohocken, PA, 2012.

[33] S.H. Huang, P. Liu, A. Mokasdar, L. Hou, Additive manufacturing and its societal impact: a literature review, The International Journal of Advanced Manufacturing Technology 67(5-8) (2013) 1191-1203.

[34] I.J. Petrick, T.W. Simpson, 3D printing disrupts manufacturing: how economies of one create new rules of competition, Research-Technology Management 56(6) (2013) 12-16.

[35] B. Berman, 3-D printing: The new industrial revolution, Business horizons 55(2) (2012) 155-162.

[36] B. Sedacca, Hand built by lasers, Engineering & Technology 6(1) (2011) 58-60.

[37] B.P. Conner, G.P. Manogharan, A.N. Martof, L.M. Rodomsky, C.M. Rodomsky, D.C. Jordan, J.W. Limperos, Making sense of 3-D printing: Creating a map of additive manufacturing products and services, Additive Manufacturing 1 (2014) 64-76.

[38] K.-U. Bletzinger, E. Ramm, Structural optimization and form finding of light weight structures, Computers & Structures 79(22) (2001) 2053-2062.

[39] Y. Huang, M.C. Leu, J. Mazumder, A. Donmez, Additive manufacturing: Current state, future potential, gaps and needs, and recommendations, Journal of Manufacturing Science and Engineering 137(1) (2015) 014001.

[40] S. Robertshaw, The collaborative economy: impact and potential of collaborative internet and additive manufacturing, Scientific Foresight Unit (STOA), European Parliament, 2015.

[41] P. Heinl, L. Müller, C. Körner, R.F. Singer, F.A. Müller, Cellular Ti–6Al–4V structures with interconnected macro porosity for bone implants fabricated by selective electron beam melting, Acta biomaterialia 4(5) (2008) 1536-1544.

[42] S.L. Ford, Additive Manufacturing Technology: Potential Implications for US Manufacturing Competitiveness, Journal of International Commerce and Economics (2014) 1-35.

[43] C. Taylor, Category Archives: SMHM 2350 Fashion Forecasting (2012).
[44] T. Wohlers, Making products by using additive manufacturing, Manufacturing Engineering 146(4) (2011) 70.
[45] J. Chua, Are 3D-Printed Fabrics the Future of Sustainable Textiles?, Ecouter re (2010).
[46] I. Gibson, T. Kvan, L. Wai Ming, Rapid prototyping for architectural models, Rapid Prototyping J 8(2) (2002) 91-95.
[47] S. Singare, Q. Lian, W. Ping Wang, J. Wang, Y. Liu, D. Li, B. Lu, Rapid prototyping assisted surgery planning and custom implant design, Rapid Prototyping J 15(1) (2009) 19-23.
[48] C. Chu, G. Graf, D.W. Rosen, Design for additive manufacturing of cellular structures, Computer-Aided Design and Applications 5(5) (2008) 686-696.
[49] Y. Luo, Z. Ji, M.C. Leu, R. Caudill, Environmental performance analysis of solid freedom fabrication processes, Proceedings of the International Symposium on Electronics and the Environment, IEEE, 1999, 1-6.
[50] N. Serres, D. Tidu, S. Sankare, F. Hlawka, Environmental comparison of MESO-CLAD® process and conventional machining implementing life cycle assessment, Journal of Cleaner Production 19(9) (2011) 1117-1124.
[51] Y. Xiong, J.M. Schoenung, Process Cost Comparison for Conventional and Near-Net-Shape Cermet Fabrication, Advanced Engineering Materials 12(3) (2010) 235-241.
[52] W. Morrow, H. Qi, I. Kim, J. Mazumder, S. Skerlos, Environmental aspects of laser-based and conventional tool and die manufacturing, Journal of Cleaner Production 15(10) (2007) 932-943.
[53] J. Mazumder, A. Schifferer, J. Choi, Direct materials deposition: designed macro and microstructure, Material Research Innovations 3(3) (1999) 118-131.
[54] P. Reeves, How the socioeconomic benefits of rapid manufacturing can offset technological limitations, RAPID 2008 Conference and Exposition. Lake Buena Vista, FL, 2008, 1-12.
[55] M. Walter, J. Holmström, H. Tuomi, H. Yrjölä, Rapid manufacturing and its impact on supply chain management, Proceedings of the Logistics Research Network Annual Conference, 2004, 9-10.
[56] C. Tuck, R. Hague, N. Burns, Rapid manufacturing: impact on supply chain methodologies and practice, International Journal of Services and Operations Management 3(1) (2006) 1-22.
[57] J. Gero, Recent advances in computational models of creative design, Computing in civil and building engineering, balkema (1995) 21-30.
[58] V. Mironov, T. Boland, T. Trusk, G. Forgacs, R.R. Markwald, Organ printing: computer-aided jet-based 3D tissue engineering, TRENDS in Biotechnology 21(4) (2003) 157-161.

[59] V. Mironov, R.P. Visconti, V. Kasyanov, G. Forgacs, C.J. Drake, R.R. Markwald, Organ printing: tissue spheroids as building blocks, Biomaterials 30(12) (2009) 2164-2174.
[60] S.V. Murphy, A. Atala, 3D bioprinting of tissues and organs, Nature biotechnology 32(8) (2014) 773-785.
[61] J. Gardan, Additive manufacturing technologies: state of the art and trends, International Journal of Production Research (2015) 1-15.
[62] I. Gibson, D.W. Rosen, B. Stucker, Additive manufacturing technologies, Springer (2010).
[63] A. Gebhardt, Understanding additive manufacturing, Carl Hanser Verlag GmbH & Co. KG, Munich (2012).
[64] W. Gao, Y. Zhang, D. Ramanujan, K. Ramani, Y. Chen, C.B. Williams, C.C. Wang, Y.C. Shin, S. Zhang, P.D. Zavattieri, The status, challenges, and future of additive manufacturing in engineering, Computer-Aided Design 69 (2015) 65-89.
[65] T. Billiet, M. Vandenhaute, J. Schelfhout, S. Van Vlierberghe, P. Dubruel, A review of trends and limitations in hydrogel-rapid prototyping for tissue engineering, Biomaterials 33(26) (2012) 6020-6041.
[66] J. Giannatsis, V. Dedoussis, Additive fabrication technologies applied to medicine and health care: a review, The International Journal of Advanced Manufacturing Technology 40(1-2) (2009) 116-127.
[67] T. Jungst, W. Smolan, K. Schacht, T. Scheibel, J. Groll, Strategies and Molecular Design Criteria for 3D Printable Hydrogels, Chemical reviews 116(3) (2015) 1496-539.
[68] B. N. Turner, R. Strong, S. A. Gold, A review of melt extrusion additive manufacturing processes: I. Process design and modeling, Rapid Prototyping J 20(3) (2014) 192-204.
[69] A. Youssef, S.J. Hollister, P.D. Dalton, Additive manufacturing of polymer melts for implantable medical devices and scaffolds, Biofabrication 9(1) (2017) 012002.
[70] F. Pati, J. Jang, D.-H. Ha, S.W. Kim, J.-W. Rhie, J.-H. Shim, D.-H. Kim, D.-W. Cho, Printing three-dimensional tissue analogues with decellularized extracellular matrix bioink, Nature communications 5 (2014) 3935.
[71] J. Pfitzner, Poiseuille and his law, Anaesthesia 31(2) (1976) 273-275.
[72] A. Bellini, S. Guceri, M. Bertoldi, Liquefier dynamics in fused deposition, Journal of Manufacturing Science and Engineering 126(2) (2004) 237-246.
[73] N. Mostafa, H.M. Syed, S. Igor, G. Andrew, A study of melt flow analysis of an ABS-Iron composite in fused deposition modelling process, Tsinghua Science & Technology 14 (2009) 29-37.

[74] H. Ramanath, C. Chua, K. Leong, K. Shah, Melt flow behaviour of poly-ε-caprolactone in fused deposition modelling, Journal of Materials Science: Materials in Medicine 19(7) (2008) 2541-2550.
[75] M. Yardimci, T. Hattori, S. Guceri, S. Danforth, Thermal analysis of fused deposition, Proceedings of the Solid Freeform Fabrication Symposium, Austin, 1997, 689-698.
[76] T. Karis, D. Dawson, C. Davis, R.-N. Kono, G. Kim, M. Jhon, S. Kim, Rapid prototyping materials rheology, Journal of Imaging Science and Technology 40(2) (1996) 147-155.
[77] L.C.F. Andrade, J.A. Petronílio, C.E.d.A. Maneschy, D.O.d.A. Cruz, The Carreau-Yasuda fluids: A skin friction equation for turbulent flow in pipes and Kolmogorov dissipative scales, Journal of the Brazilian Society of Mechanical Sciences and Engineering 29(2) (2007) 162-167.
[78] J. Boyd, J.M. Buick, S. Green, Analysis of the Casson and Carreau-Yasuda non-Newtonian blood models in steady and oscillatory flows using the lattice Boltzmann method, Physics of Fluids 19(9) (2007) 093103.
[79] J. Aho, J.P. Boetker, S. Baldursdottir, J. Rantanen, Rheology as a tool for evaluation of melt processability of innovative dosage forms, International journal of pharmaceutics 494(2) (2015) 623-642.
[80] W. Kuhn, über die gestalt fadenförmiger moleküle in lösungen, Kolloid-Zeitschrift 68(1) (1934) 2-15.
[81] K. Šolc, Shape of a Random-Flight Chain, The Journal of Chemical Physics 55(1) (1971) 335-344.
[82] F. Cogswell, Converging flow of polymer melts in extrusion dies, Polymer Engineering & Science 12(1) (1972) 64-73.
[83] W. Michaeli, Extrusion dies for plastics and rubber, Carl Hanser Verlag GmbH & Co. KG (2003).
[84] H.F. Brinson, L.C. Brinson, Polymer engineering science and viscoelasticity, Springer (2008).
[85] K. Marynowski, T. Kapitaniak, Kelvin–Voigt versus Bürgers internal damping in modeling of axially moving viscoelastic web, International Journal of Non-Linear Mechanics 37(7) (2002) 1147-1161.
[86] H. Schiessel, R. Metzler, A. Blumen, T. Nonnenmacher, Generalized viscoelastic models: their fractional equations with solutions, Journal of physics A: Mathematical and General 28(23) (1995) 6567.
[87] A.P. Deshpande, J.M. Krishnan, S. Kumar, Rheology of complex fluids, Springer Science & Business Media (2010).
[88] J.-Z. Liang, A relationship between extrudate swell ratio and entry stored elastic strain energy during die flow of tyre compounds, Polymer testing 23(4) (2004) 441-446.

[89] J.Z. Liang, Die-swell behavior during the short-tube flow of rubber compounds, Journal of applied polymer science 104(1) (2007) 70-74.
[90] C.D. Han, R.R. Lamonte, Y.T. Shah, Studies on melt spinning. III. Flow instabilities in melt spinning: Melt fracture and draw resonance, Journal of Applied Polymer Science 16(12) (1972) 3307-3323.
[91] V. González-González, G. Neira-Velázquez, J. Angulo-Sánchez, Polypropylene chain scissions and molecular weight changes in multiple extrusion, Polymer Degradation and Stability 60(1) (1998) 33-42.
[92] T. Ogawa, Effects of molecular weight on mechanical properties of polypropylene, Journal of applied polymer science 44(10) (1992) 1869-1871.
[93] G. Perego, G.D. Cella, C. Bastioli, Effect of molecular weight and crystallinity on poly (lactic acid) mechanical properties, Journal of Applied Polymer Science 59(1) (1996) 37-43.
[94] W. Gilbert, E. Wright, De magnete, magneticisque corporibus, et de magno magnete tellure: physiologia noua, plurimis & argumentis, & experimentis demonstrata, excudebat Short (1967).
[95] D. Li, Y. Xia, Electrospinning of nanofibers: reinventing the wheel?, Advanced materials 16(14) (2004) 1151-1170.
[96] A. Greiner, J.H. Wendorff, Electrospinning: a fascinating method for the preparation of ultrathin fibers, Angewandte Chemie International Edition 46(30) (2007) 5670-5703.
[97] J. Doshi, D.H. Reneker, Electrospinning process and applications of electrospun fibers, Conference Record of the Industry Applications Society Annual Meeting, IEEE, 1993, 1698-1703.
[98] D. Reneker, A. Yarin, E. Zussman, H. Xu, Electrospinning of nanofibers from polymer solutions and melts, Advances in applied mechanics 41 (2007) 43-346.
[99] J. Lyons, C. Li, F. Ko, Melt-electrospinning part I: processing parameters and geometric properties, Polymer 45(22) (2004) 7597-7603.
[100] L. Rayleigh, On the equilibrium of liquid conducting masses charged with electricity, The London, Edinburgh, and Dublin Philosophical Magazine and Journal of Science 14(87) (1882) 184-186.
[101] M. Komarek, L. Martinova, Design and evaluation of melt-electrospinning electrodes, Proceedings of the 2nd Nanocon International Conference, 2010, 72-77.
[102] T.D. Brown, P.D. Dalton, D.W. Hutmacher, Melt Electrospinning Today: An Opportune Time for an Emerging Polymer Process, Progress in Polymer Science 56 (2016) 116–166.
[103] G. Taylor, Disintegration of water drops in an electric field, Proceedings of the Royal Society of London A: Mathematical, Physical and Engineering Sciences, The Royal Society, 1964, 383-397.

[104] G. Taylor, Electrically driven jets, Proceedings of the Royal Society of London A: Mathematical, Physical and Engineering Sciences, The Royal Society, 1969, 453-475.
[105] D. Giancoli, Physics for Scientists & Engineers Third Edition, Upper Saddle River: Prentice Hall, 2000.
[106] D.C. Giancoli, Physik: Lehr-und Übungsbuch, Pearson Deutschland GmbH (2010).
[107] C. Wei, J. Dong, Direct fabrication of high-resolution three-dimensional polymeric scaffolds using electrohydrodynamic hot jet plotting, Journal of Micromechanics and Microengineering 23(2) (2013) 025017.
[108] X. Wu, R.D. Oleschuk, N.M. Cann, Characterization of microstructured fibre emitters: in pursuit of improved nano electrospray ionization performance, Analyst 137(18) (2012) 4150-4161.
[109] D. Saville, Electrohydrodynamics: the Taylor-Melcher leaky dielectric model, Annual review of fluid mechanics 29(1) (1997) 27-64.
[110] V. Kirichenko, S.I. PETRYANOV, N. Suprun, A. Shutov, Asymptotic radius of a slightly conducting liquid jet in an electric field, SOVIET PHYSICS DOKLADY (1986).
[111] A.F. Spivak, Y.A. Dzenis, Asymptotic decay of radius of a weakly conductive viscous jet in an external electric field, Applied Physics Letters 73(21) (1998) 3067–3069.
[112] J.H. Jeans, The mathematical theory of electricity and magnetism, University Press (1908).
[113] D.H. Reneker, A.L. Yarin, H. Fong, S. Koombhongse, Bending instability of electrically charged liquid jets of polymer solutions in electrospinning, Journal of Applied physics 87(9) (2000) 4531-4547.
[114] M.M. Hohman, M. Shin, G. Rutledge, M.P. Brenner, Electrospinning and electrically forced jets. I. Stability theory, Physics of Fluids (1994-present) 13(8) (2001) 2201-2220.
[115] S.V. Fridrikh, H.Y. Jian, M.P. Brenner, G.C. Rutledge, Controlling the fiber diameter during electrospinning, Phys Rev Lett 90(14) (2003) 144502.
[116] Y. Shin, M. Hohman, M. Brenner, G. Rutledge, Experimental characterization of electrospinning: the electrically forced jet and instabilities, Polymer 42(25) (2001) 9955-9967.
[117] Y. Shin, M. Hohman, M. Brenner, G. Rutledge, Electrospinning: A whipping fluid jet generates submicron polymer fibers, Applied physics letters 78(8) (2001) 1149-1151.
[118] D. Li, G. Ouyang, J.T. McCann, Y. Xia, Collecting electrospun nanofibers with patterned electrodes, Nano letters 5(5) (2005) 913-916.

[119] U. Boudriot, R. Dersch, A. Greiner, J.H. Wendorff, Electrospinning approaches toward scaffold engineering—a brief overview, Artificial organs 30(10) (2006) 785-792.
[120] P. Katta, M. Alessandro, R. Ramsier, G. Chase, Continuous electrospinning of aligned polymer nanofibers onto a wire drum collector, Nano letters 4(11) (2004) 2215-2218.
[121] D. Zhang, J. Chang, Electrospinning of three-dimensional nanofibrous tubes with controllable architectures, Nano letters 8(10) (2008) 3283-3287.
[122] P.D. Dalton, D. Klee, M. Möller, Electrospinning with dual collection rings, Polymer 46(3) (2005) 611-614.
[123] M.M. Arras, C. Grasl, H. Bergmeister, H. Schima, Electrospinning of aligned fibers with adjustable orientation using auxiliary electrodes, Science and technology of advanced materials (2016).
[124] J. Deitzel, J. Kleinmeyer, J. Hirvonen, N.B. Tan, Controlled deposition of electrospun poly (ethylene oxide) fibers, Polymer 42(19) (2001) 8163-8170.
[125] J. Lee, S.Y. Lee, J. Jang, Y.H. Jeong, D.-W. Cho, Fabrication of patterned nanofibrous mats using direct-write electrospinning, Langmuir 28(18) (2012) 7267-7275.
[126] S.L. Shenoy, W.D. Bates, H.L. Frisch, G.E. Wnek, Role of chain entanglements on fiber formation during electrospinning of polymer solutions: good solvent, non-specific polymer–polymer interaction limit, Polymer 46(10) (2005) 3372-3384.
[127] A. Ganan-Calvo, J. Davila, A. Barrero, Current and droplet size in the electrospraying of liquids. Scaling laws, Journal of Aerosol Science 28(2) (1997) 249-275.
[128] A. Jaworek, A. Sobczyk, Electrospraying route to nanotechnology: an overview, Journal of Electrostatics 66(3) (2008) 197-219.
[129] G. Hochleitner, T. Jungst, T.D. Brown, K. Hahn, C. Moseke, F. Jakob, P.D. Dalton, J. Groll, Additive manufacturing of scaffolds with sub-micron filaments via melt electrospinning writing, Biofabrication 7(3) (2015) 035002.
[130] L.-H. Zhang, X.-P. Duan, X. Yan, M. Yu, X. Ning, Y. Zhao, Y.-Z. Long, Recent Advances in Melt Electrospinning, RSC Advances 6(58) (2016) 53400-53414.
[131] C. Luo, E. Stride, M. Edirisinghe, Mapping the influence of solubility and dielectric constant on electrospinning polycaprolactone solutions, Macromolecules 45(11) (2012) 4669-4680.
[132] D.H. Reneker, A.L. Yarin, Electrospinning jets and polymer nanofibers, Polymer 49(10) (2008) 2387-2425.
[133] A. Frenot, I.S. Chronakis, Polymer nanofibers assembled by electrospinning, Current opinion in colloid & interface science 8(1) (2003) 64-75.

[134] D. Sun, C. Chang, S. Li, L. Lin, Near-field electrospinning, Nano letters 6(4) (2006) 839-842.
[135] J.-U. Park, M. Hardy, S.J. Kang, K. Barton, K. Adair, D. kishore Mukhopadhyay, C.Y. Lee, M.S. Strano, A.G. Alleyne, J.G. Georgiadis, High-resolution electrohydrodynamic jet printing, Nature materials 6(10) (2007) 782-789.
[136] G. Hochleitner, J.F. Hümmer, R. Luxenhofer, J. Groll, High definition fibrous poly(2-ethyl-2-oxazoline) scaffolds through melt electrospinning writing, Polymer 55(20) (2014) 5017-5023.
[137] T.D. Brown, P.D. Dalton, D.W. Hutmacher, Direct Writing By Way of Melt Electrospinning, Advanced Materials 23(47) (2011) 5651–5657.
[138] J.M. Deitzel, N.C. BeckTan, J.D. Kleinmeyer, J. Rehrmann, D. Tevault, Generation of Polymer Nanofibers Through Electrospinning, DTIC Document, 1999.
[139] D.H. Reneker, I. Chun, Nanometre diameter fibres of polymer, produced by electrospinning, Nanotechnology 7(3) (1996) 216-223.
[140] T.A. Osswald, Understanding Polymer Processing: Processes and Governing Equations, Carl Hanser Verlag GmbH Co KG (2015).
[141] I.J. Goldfarb, R. McGuchan, Thermal Degradation of Polyesters: Part 1. Aliphatic Polymers, DTIC Document, 1968.
[142] I. McNeill, H. Leiper, Degradation studies of some polyesters and polycarbonates—2. Polylactide: degradation under isothermal conditions, thermal degradation mechanism and photolysis of the polymer, Polymer degradation and stability 11(4) (1985) 309-326.
[143] H.A. Pohl, The thermal degradation of polyesters, Journal of the American Chemical Society 73(12) (1951) 5660-5661.
[144] T.D. Brown, F. Edin, N. Detta, A.D. Skelton, D.W. Hutmacher, P.D. Dalton, Melt electrospinning of poly (ε-caprolactone) scaffolds: Phenomenological observations associated with collection and direct writing, Materials Science and Engineering: C 45 (2014) 698-708.
[145] Y. Kadomae, Y. Maruyama, M. Sugimoto, T. Taniguchi, K. Koyama, Relation between tacticity and fiber diameter in melt-electrospinning of polypropylene, Fibers and Polymers 10(3) (2009) 275-279.
[146] J. Deitzel, J. Kleinmeyer, D. Harris, N.B. Tan, The effect of processing variables on the morphology of electrospun nanofibers and textiles, Polymer 42(1) (2001) 261-272.
[147] C.S. Kalra, M. Kossitsyn, K. Iskenderova, A. Chirokov, Y.I. Cho, A. Gutsol, A. Fridman, Electrical discharges in the reverse vortex flow–tornado discharges, Electronic Proceedings of 16th International Symposium on Plasma Chemistry, Taormina, Italy, Citeseer, 2003.

[148] E. Zhmayev, D. Cho, Y.L. Joo, Electrohydrodynamic quenching in polymer melt electrospinning, Physics of Fluids 23(7) (2011).

[149] S. Tripatanasuwan, D.H. Reneker, Corona discharge from electrospinning jet of poly (ethylene oxide) solution, Polymer 50(8) (2009) 1835-1837.

[150] F.W. Peek, Dielectric phenomena in high voltage engineering, McGraw-Hill Book Company, Incorporated (1920).

[151] D.B. Go, R.A. Maturana, T.S. Fisher, S.V. Garimella, Enhancement of external forced convection by ionic wind, International Journal of Heat and Mass Transfer 51(25) (2008) 6047-6053.

[152] M. Havet, Effect of process parameters on the EHD airflow, Journal of Electrostatics 67(2) (2009) 222-227.

[153] M. Goldman, A. Goldman, R. Sigmond, The corona discharge, its properties and specific uses, Pure and Applied Chemistry 57(9) (1985) 1353-1362.

[154] S. Laohalertdecha, P. Naphon, S. Wongwises, A review of electrohydrodynamic enhancement of heat transfer, Renewable and Sustainable Energy Reviews 11(5) (2007) 858-876.

[155] J. Zhang, A. Gupta, J. Baker, Effect of relative humidity on the prediction of natural convection heat transfer coefficients, Heat transfer engineering 28(4) (2007) 335-342.

[156] M. Still, H. Venzke, F. Durst, A. Melling, Influence of humidity on the convective heat transfer from small cylinders, Experiments in fluids 24(2) (1998) 141-150.

[157] E. Koscher, R. Fulchiron, Influence of shear on polypropylene crystallization: morphology development and kinetics, Polymer 43(25) (2002) 6931-6942.

[158] G. Kumaraswamy, A.M. Issaian, J.A. Kornfield, Shear-enhanced crystallization in isotactic polypropylene. 1. Correspondence between in situ rheo-optics and ex situ structure determination, Macromolecules 32(22) (1999) 7537-7547.

[159] D.M. Shin, J.S. Lee, H.W. Jung, J.C. Hyun, High-speed fiber spinning process with spinline flow-induced crystallization and neck-like deformation, Rheologica acta 45(5) (2006) 575-582.

[160] E. Zhmayev, D. Cho, Y.L. Joo, Modeling of melt electrospinning for semi-crystalline polymers, Polymer 51(1) (2010) 274-290.

[161] A. Ziabicki, G.C. Alfonso, A simple model of flow-induced crystallization memory, Macromolecular Symposia, Wiley Online Library, 2002, 211-231.

[162] A. Ziabicki, Fundamentals of Fiber Formation, Willey, London (1976).

[163] W.D. Callister, D.G. Rethwisch, Materials science and engineering: an introduction, Wiley New York (2007).

[164] G. Collins, J. Federici, Y. Imura, L.H. Catalani, Charge generation, charge transport, and residual charge in the electrospinning of polymers: a review of issues and complications, Journal of Applied Physics 111(4) (2012) 044701.
[165] A. Mishra, Studies of polymer electrets. II. Factors governing the stabilities of homoelectrets obtained from polystyrene and its derivatives, Journal of Applied Polymer Science 27(4) (1982) 1107-1118.
[166] M. Stournara, R. Ramprasad, A first principles investigation of isotactic polypropylene, Journal of materials science 45(2) (2010) 443-447.
[167] Y. Arita, S.S. Shiratori, K. Ikezaki, A method for detection and visualization of charge trapping sites in amorphous parts in crystalline polymers, Journal of Electrostatics 57(3) (2003) 263-271.
[168] N. Ristovski, N. Bock, S. Liao, S.K. Powell, J. Ren, G.T. Kirby, K.A. Blackwood, M.A. Woodruff, Improved fabrication of melt electrospun tissue engineering scaffolds using direct writing and advanced electric field control, Biointerphases 10(1) (2015) 011006.
[169] B. Dhandayuthapani, Y. Yoshida, T. Maekawa, D.S. Kumar, Polymeric scaffolds in tissue engineering application: a review, International Journal of Polymer Science (2011).
[170] R. Langer, J.P. Vacanti, Tissue engineering, Science 260(5110) (1993) 920-926.
[171] L.G. Griffith, G. Naughton, Tissue engineering--current challenges and expanding opportunities, Science 295(5557) (2002) 1009-1014.
[172] P.X. Ma, Scaffolds for tissue fabrication, Mater Today 7(5) (2004) 30-40.
[173] A.S. Mistry, A.G. Mikos, Tissue engineering strategies for bone regeneration, Regenerative medicine II 94 (2005) 129-129.
[174] D. Hutmacher, T. Woodfield, P. Dalton, J. Lewis, Scaffold design and fabrication, Ieee T Autom Sci Eng 5(3) (2008) 446-456.
[175] J.E. Babensee, J.M. Anderson, L.V. McIntire, A.G. Mikos, Host response to tissue engineered devices, Advanced drug delivery reviews 33(1) (1998) 111-139.
[176] F.J. O'brien, Biomaterials & scaffolds for tissue engineering, Mater Today 14(3) (2011) 88-95.
[177] L.S. Nair, C.T. Laurencin, Biodegradable polymers as biomaterials, Progress in polymer science 32(8) (2007) 762-798.
[178] J. Andrade, V. Hlady, Protein adsorption and materials biocompatibility: a tutorial review and suggested hypotheses, Biopolymers/Non-Exclusion HPLC, Springer (1986), 1-63.
[179] M. Vert, Aliphatic polyesters: great degradable polymers that cannot do everything, Biomacromolecules 6(2) (2005) 538-546.

[180] J. Heller, J. Barr, S.Y. Ng, K.S. Abdellauoi, R. Gurny, Poly (ortho esters): synthesis, characterization, properties and uses, Advanced Drug Delivery Reviews 54(7) (2002) 1015-1039.

[181] D. Das, Z. Zhang, T. Winkler, M. Mour, C.I. Günter, M.M. Morlock, H.-G. Machens, A.F. Schilling, Bioresorption and degradation of biomaterials, Tissue Engineering III: Cell-Surface Interactions for Tissue Culture, Springer (2011), 317-333.

[182] J.A. Pedersen, M.A. Swartz, Mechanobiology in the third dimension, Annals of biomedical engineering 33(11) (2005) 1469-1490.

[183] T.A. Wren, S.A. Yerby, G.S. Beaupré, D.R. Carter, Mechanical properties of the human Achilles tendon, Clinical Biomechanics 16(3) (2001) 245-251.

[184] A.S. Rowlands, P.A. George, J.J. Cooper-White, Directing osteogenic and myogenic differentiation of MSCs: interplay of stiffness and adhesive ligand presentation, American Journal of Physiology-Cell Physiology 295(4) (2008) C1037-C1044.

[185] R.Y. Kannan, H.J. Salacinski, K. Sales, P. Butler, A.M. Seifalian, The roles of tissue engineering and vascularisation in the development of micro-vascular networks: a review, Biomaterials 26(14) (2005) 1857-1875.

[186] J. Rouwkema, N.C. Rivron, C.A. van Blitterswijk, Vascularization in tissue engineering, Trends in biotechnology 26(8) (2008) 434-441.

[187] J.H. Brauker, V.E. Carr-Brendel, L.A. Martinson, J. Crudele, W.D. Johnston, R.C. Johnson, Neovascularization of synthetic membranes directed by membrane microarchitecture, Journal of biomedical materials research 29(12) (1995) 1517-1524.

[188] G.J. Picha, R.F. Drake, Pillared-surface microstructure and soft-tissue implants: Effect of implant site and fixation, Journal of biomedical materials research 30(3) (1996) 305-312.

[189] A.A. Sharkawy, B. Klitzman, G.A. Truskey, W.M. Reichert, Engineering the tissue which encapsulates subcutaneous implants. I. Diffusion properties, Journal of biomedical materials research 37(3) (1997) 401-412.

[190] A. Von Recum, T. Van Kooten, The influence of micro-topography on cellular response and the implications for silicone implants, Journal of Biomaterials Science, Polymer Edition 7(2) (1996) 181-198.

[191] J.D. Bryers, C.M. Giachelli, B.D. Ratner, Engineering biomaterials to integrate and heal: the biocompatibility paradigm shifts, Biotechnology and bioengineering 109(8) (2012) 1898-1911.

[192] D.W. Hutmacher, Scaffold design and fabrication technologies for engineering tissues—state of the art and future perspectives, Journal of Biomaterials Science, Polymer Edition 12(1) (2001) 107-124.

[193] D.W. Hutmacher, Scaffolds in tissue engineering bone and cartilage, Biomaterials 21(24) (2000) 2529-2543.
[194] J.M. Karp, K. Rzeszutek, M.S. Shoichet, J.E. Davies, Fabrication of precise cylindrical three-dimensional tissue engineering scaffolds for in vitro and in vivo bone engineering applications, J Craniofac Surg 14(3) (2003) 317-323.
[195] L.D. Harris, B.-S. Kim, D.J. Mooney, Open pore biodegradable matrices formed with gas foaming, J Biomed Mater Res 42(3) (1998) 396-402.
[196] M. Borden, M. Attawia, Y. Khan, C.T. Laurencin, Tissue engineered microsphere-based matrices for bone repair: design and evaluation, Biomaterials 23(2) (2002) 551-559.
[197] H.-W. Kang, Y. Tabata, Y. Ikada, Fabrication of porous gelatin scaffolds for tissue engineering, Biomaterials 20(14) (1999) 1339-1344.
[198] T. Weiß, G. Hildebrand, R. Schade, K. Liefeith, Two-Photon polymerization for microfabrication of three-dimensional scaffolds for tissue engineering application, Engineering in Life Sciences 9(5) (2009) 384-390.
[199] Y. Fukano, M. Usui, R. Underwood, S. Isenhath, A. Marshall, K. Hauch, B. Ratner, J. Olerud, P. Fleckman, Epidermal and dermal integration into sphere-templated porous poly (2-hydroxyethyl methacrylate) implants in mice, Journal of Biomedical Materials Research Part A 94(4) (2010) 1172-1186.
[200] A. Seidi, M. Ramalingam, I. Elloumi-Hannachi, S. Ostrovidov, A. Khademhosseini, Gradient biomaterials for soft-to-hard interface tissue engineering, Acta biomaterialia 7(4) (2011) 1441-1451.
[201] M. Singh, C. Berkland, M.S. Detamore, Strategies and applications for incorporating physical and chemical signal gradients in tissue engineering, Tissue Engineering Part B: Reviews 14(4) (2008) 341-366.
[202] N. Lee, J. Robinson, H. Lu, Biomimetic strategies for engineering composite tissues, Current opinion in biotechnology 40 (2016) 64-74.
[203] W. Friess, Collagen–biomaterial for drug delivery, European Journal of Pharmaceutics and Biopharmaceutics 45(2) (1998) 113-136.
[204] A. Di Martino, M. Sittinger, M.V. Risbud, Chitosan: a versatile biopolymer for orthopaedic tissue-engineering, Biomaterials 26(30) (2005) 5983-5990.
[205] A.D. Augst, H.J. Kong, D.J. Mooney, Alginate hydrogels as biomaterials, Macromolecular bioscience 6(8) (2006) 623-633.
[206] Y. Luo, K.R. Kirker, G.D. Prestwich, Cross-linked hyaluronic acid hydrogel films: new biomaterials for drug delivery, Journal of controlled release 69(1) (2000) 169-184.
[207] C. Collombel, O. Damour, C. Gagnieu, F. Poinsignon, C. Echinard, J. Marichy, Biomaterials with a base of mixtures of collagen, chitosan and glycosaminoglycans, process for preparing them and their application in human medicine, U.S. Patent No. 5,166,187, Google Patents, 1992.

[208] W.F. Daamen, J. Veerkamp, J. Van Hest, T. Van Kuppevelt, Elastin as a biomaterial for tissue engineering, Biomaterials 28(30) (2007) 4378-4398.
[209] C. Wong, E. Inman, R. Spaethe, S. Helgerson, Fibrin-based biomaterials to deliver human growth factors, Thrombosis and haemostasis 89(3) (2003) 573-582.
[210] P.A. Gunatillake, R. Adhikari, Biodegradable synthetic polymers for tissue engineering, Eur Cell Mater 5(1) (2003) 1-16.
[211] E. Klüver, M. Meyer, Preparation, processing, and rheology of thermoplastic collagen, Journal of Applied Polymer Science 128(6) (2013) 4201-4211.
[212] K.E. Uhrich, S.M. Cannizzaro, R.S. Langer, K.M. Shakesheff, Polymeric systems for controlled drug release, Chemical reviews 99(11) (1999) 3181-3198.
[213] C.K. Williams, Synthesis of functionalized biodegradable polyesters, Chemical Society Reviews 36(10) (2007) 1573-1580.
[214] J.O. Hollinger, Preliminary report on the osteogenic potential of a biodegradable copolymer of polyactide (PLA) and polyglycolide (PGA), Journal of biomedical materials research 17(1) (1983) 71-82.
[215] J.O. Hollinger, G.C. Battistone, Biodegradable Bone Repair Materials Synthetic Polymers and Ceramics, Clinical orthopaedics and related research 207(207) (1986) 290-306.
[216] N. Ashammakhi, P. Rokkanen, Absorbable polyglycolide devices in trauma and bone surgery, Biomaterials 18(1) (1997) 3-9.
[217] Y. Ikada, H. Tsuji, Biodegradable polyesters for medical and ecological applications, Macromolecular rapid communications 21(3) (2000) 117-132.
[218] S. Vainionpää, Biodegradation of polyglycolic acid in bone tissue: An experimental study on rabbits, Archives of orthopaedic and traumatic surgery 104(6) (1986) 333-338.
[219] P. Christel, F. Chabot, J. Leray, C. Morin, M. Vert, Biodegradable composites for internal fixation, Biomaterials 1 (1980) 271-280.
[220] M. Vert, P. Christel, F. Chabot, J. Leray, Bioresorbable plastic materials for bone surgery (1984).
[221] M. Meek, J. Coert, Clinical use of nerve conduits in peripheral-nerve repair: review of the literature, Journal of reconstructive microsurgery 18(02) (2002) 97-110.
[222] B.C. Benicewicz, P.K. Hopper, Review: Polymers for Absorbable Surgical Sutures—Part II, Journal of Bioactive and Compatible Polymers 6(1) (1991) 64-94.
[223] T. Shinozaki, R. Hayashi, M. Ebihara, M. Miyazaki, T. Tomioka, Mucosal defect repair with a polyglycolic acid sheet, Japanese journal of clinical oncology 43(1) (2013) 33-36.

[224] L. Avérous, Polylactic acid: synthesis, properties and applications, Elsevier: Oxford, UK (2008).
[225] B.D. Ulery, L.S. Nair, C.T. Laurencin, Biomedical applications of biodegradable polymers, Journal of polymer science Part B: polymer physics 49(12) (2011) 832-864.
[226] W. Hoogsteen, A. Postema, A. Pennings, G. Ten Brinke, P. Zugenmaier, Crystal structure, conformation and morphology of solution-spun poly (L-lactide) fibers, Macromolecules 23(2) (1990) 634-642.
[227] P. Mainil-Varlet, B. Rahn, S. Gogolewski, Long-term in vivo degradation and bone reaction to various polylactides: 1. One-year results, Biomaterials 18(3) (1997) 257-266.
[228] G. Narayanan, V.N. Vernekar, E.L. Kuyinu, C.T. Laurencin, Poly (lactic acid)-based biomaterials for orthopaedic regenerative engineering, Advanced drug delivery reviews 107 (2016) 247-276.
[229] M. Labet, W. Thielemans, Synthesis of polycaprolactone: a review, Chemical Society Reviews 38(12) (2009) 3484-3504.
[230] N. Bölgen, Y.Z. Menceloğlu, K. Acatay, I. Vargel, E. Pişkin, In vitro and in vivo degradation of non-woven materials made of poly (ε-caprolactone) nanofibers prepared by electrospinning under different conditions, Journal of Biomaterials Science, Polymer Edition 16(12) (2005) 1537-1555.
[231] J. Ray, N. Doddi, D. Regula, J. Williams, A. Melveger, Polydioxanone (PDS), a novel monofilament synthetic absorbable suture, Surgery, gynecology & obstetrics 153(4) (1981) 497-507.
[232] S.F. Williams, S. Rizk, D.P. Martin, Poly-4-hydroxybutyrate (P4HB): a new generation of resorbable medical devices for tissue repair and regeneration, Biomedizinische Technik/Biomedical Engineering 58(5) (2013) 439-452.
[233] J.P. Fisher, J.W. Vehof, D. Dean, J.P. van der Waerden, T.A. Holland, A.G. Mikos, J.A. Jansen, Soft and hard tissue response to photocrosslinked poly (propylene fumarate) scaffolds in a rabbit model, Journal of biomedical materials research 59(3) (2002) 547-556.
[234] A. Merkli, J. Heller, C. Tabatabay, R. Gurny, Synthesis and characterization of a new biodegradable semi-solid poly (ortho ester) for drug delivery systems, Journal of Biomaterials Science, Polymer Edition 4(5) (1993) 505-516.
[235] J.-M. Lü, X. Wang, C. Marin-Muller, H. Wang, P.H. Lin, Q. Yao, C. Chen, Current advances in research and clinical applications of PLGA-based nanotechnology, Expert review of molecular diagnostics (2014).
[236] T. Ryynänen, A. Nykänen, J. Seppälä, Poly (CL/DLLA-b-CL) multiblock copolymers as biodegradable thermoplastic elastomers, eXPRESS Polymer Letters 2(3) (2008) 184-193.

[237] R. Hoogenboom, H.M.L. Thijs, M.J.H.C. Jochems, B.M. van Lankvelt, M.W.M. Fijten, U.S. Schubert, Tuning the LCST of poly(2-oxazoline)s by varying composition and molecular weight: alternatives to poly(N-isopropylacrylamide)?, Chemical Communications (44) (2008) 5758–5760.
[238] R. Luxenhofer, R. Jordan, Click Chemistry with Poly(2-oxazoline)s, Macromolecules 39(10) (2006) 3509-3516.
[239] R. Hoogenboom, Poly(2-oxazoline)s: A Polymer Class with Numerous Potential Applications, Angewandte Chemie International Edition 48(43) (2009) 7978-7994.
[240] H. Schlaad, C. Diehl, A. Gress, M. Meyer, A.L. Demirel, Y. Nur, A. Bertin, Poly(2-oxazoline)s as Smart Bioinspired Polymers, Macromolecular Rapid Communications 31(6) (2010) 511-525.
[241] M. Hartlieb, D. Pretzel, C. Englert, M. Hentschel, K. Kempe, M. Gottschaldt, U.S. Schubert, Matrix supported poly(2-oxazoline)-based hydrogels for DNA catch and release, Biomacromolecules 15(6) (2014) 1970–1978.
[242] A. Dworak, A. Utrata-Wesołek, N. Oleszko, W. Wałach, B. Trzebicka, J. Anioł, A.L. Sieroń, A. Klama-Baryła, M. Kawecki, Poly(2-substituted-2-oxazoline) surfaces for dermal fibroblasts adhesion and detachment, Journal of Materials Science: Materials in Medicine 25(4) (2014) 1149-1163.
[243] R. Hoogenboom, Poly (2-oxazoline) s: Alive and Kicking, Macromolecular Chemistry and Physics 208(1) (2007) 18-25.
[244] M.M. Bloksma, R.M. Paulus, H.P.C. van Kuringen, F. van der Woerdt, H.M.L. Lambermont-Thijs, U.S. Schubert, R. Hoogenboom, Thermoresponsive Poly(2-oxazine)s, Macromolecular Rapid Communications 33(1) (2012) 92–96.
[245] D. Christova, R. Velichkova, W. Loos, E.J. Goethals, F.D. Prez, New thermo-responsive polymer materials based on poly(2-ethyl-2-oxazoline) segments, Polymer 44(8) (2003) 2255-2261.
[246] F.C. Gaertner, R. Luxenhofer, B. Blechert, R. Jordan, M. Essler, Synthesis, biodistribution and excretion of radiolabeled poly (2-alkyl-2-oxazoline) s, Journal of Controlled Release 119(3) (2007) 291-300.
[247] R. Hoogenboom, Poly (2-oxazoline) s: a polymer class with numerous potential applications, Angewandte Chemie International Edition 48(43) (2009) 7978-7994.
[248] P. Goddard, L.E. Hutchinson, J. Brown, L.J. Brookman, Soluble polymeric carriers for drug delivery. Part 2. Preparation and in vivo behaviour of N-acylethylenimine copolymers, Journal of Controlled Release 10(1) (1989) 5-16.
[249] R. Luxenhofer, A. Schulz, C. Roques, S. Li, T.K. Bronich, E.V. Batrakova, R. Jordan, A.V. Kabanov, Doubly amphiphilic poly (2-oxazoline) s as high-capacity delivery systems for hydrophobic drugs, Biomaterials 31(18) (2010) 4972-4979.

[250] R. Luxenhofer, Y. Han, A. Schulz, J. Tong, Z. He, A.V. Kabanov, R. Jordan, Poly (2-oxazoline) s as Polymer Therapeutics, Macromolecular rapid communications 33(19) (2012) 1613-1631.
[251] R. Konradi, B. Pidhatika, A. Mühlebach, M. Textor, Poly-2-methyl-2-oxazoline: a peptide-like polymer for protein-repellent surfaces, Langmuir 24(3) (2008) 613-616.
[252] G. Hochleitner, A. Youssef, A. Hrynevich, J.N. Haigh, T. Jungst, J. Groll, P.D. Dalton, Fibre pulsing during melt electrospinning writing, BioNanoMaterials 17(3-4) (2016) 159-171.
[253] M.L. Abell, J.P. Braselton, J.A. Rafter, Statistics with mathematica, Academic Press (1999).
[254] C.J. Petrie, M.M. Denn, Instabilities in polymer processing, Aiche J 22(2) (1976) 209-236.
[255] H.H. George, Model of steady-state melt spinning at intermediate take-up speeds, Polymer Engineering & Science 22(5) (1982) 292-299.
[256] K. Min, J.L. White, J.F. Fellers, High density polyethylene/polystyrene blends: phase distribution morphology, rheological measurements, extrusion, and melt spinning behavior, Journal of applied polymer science 29(6) (1984) 2117-2142.
[257] S. Kase, Studies on melt spinning. IV. On the stability of melt spinning, Journal of Applied Polymer Science 18(11) (1974) 3279-3304.
[258] A. Bergonzoni, A. DiCresce, The phenomenon of draw resonance in polymeric melts. Part I—qualitative view, Polymer Engineering & Science 6(1) (1966) 45-49.
[259] H.W. Jung, J.C. Hyun, Instabilities in extensional deformation polymer processing, Rheology Reviews 2006 (2006) 131.
[260] S. Kase, T. Matsuo, Studies on melt spinning. II. Steady-state and transient solutions of fundamental equations compared with experimental results, Journal of Applied Polymer Science 11(2) (1967) 251-287.
[261] P. Lamb, Analysis of fabrication processes, SCI Monograph 26 (1967) 296.
[262] H. Ishihara, S. Kase, Studies on melt spinning. VI. Simulation of draw resonance using Newtonian and power law viscosities, Journal of Applied Polymer Science 20(1) (1976) 169-191.
[263] R.J. Fisher, M.M. Denn, A theory of isothermal melt spinning and draw resonance, Aiche J 22(2) (1976) 236-246.
[264] W.-K. Lee, A correlation of the onset of draw resonance spinline instability, Chemical engineering communications 53(1-6) (1987) 117-130.
[265] K.A.G. Katsogiannis, G.T. Vladisavljević, S. Georgiadou, Porous electrospun polycaprolactone (PCL) fibres by phase separation, European Polymer Journal 69 (2015) 284-295.

[266] F. Croisier, A.-S. Duwez, C. Jérôme, A. Léonard, K. Van Der Werf, P. Dijkstra, M. Bennink, Mechanical testing of electrospun PCL fibers, Acta biomaterialia 8(1) (2012) 218-224.
[267] K. Lee, H. Kim, M. Khil, Y. Ra, D. Lee, Characterization of nano-structured poly (ε-caprolactone) nonwoven mats via electrospinning, Polymer 44(4) (2003) 1287-1294.
[268] L. Van der Schueren, B. De Schoenmaker, Ö.I. Kalaoglu, K. De Clerck, An alternative solvent system for the steady state electrospinning of polycaprolactone, European Polymer Journal 47(6) (2011) 1256-1263.
[269] E. Formo, E. Lee, D. Campbell, Y. Xia, Functionalization of electrospun TiO2 nanofibers with Pt nanoparticles and nanowires for catalytic applications, Nano Letters 8(2) (2008) 668-672.
[270] S. Sharma, A. Sharma, Y.-K. Cho, M. Madou, Increased graphitization in electrospun single suspended carbon nanowires integrated with carbon-MEMS and carbon-NEMS platforms, ACS applied materials & interfaces 4(1) (2012) 34-39.
[271] X. Wang, C. Drew, S.-H. Lee, K.J. Senecal, J. Kumar, L.A. Samuelson, Electrospun nanofibrous membranes for highly sensitive optical sensors, Nano letters 2(11) (2002) 1273-1275.
[272] S. Cavaliere, S. Subianto, I. Savych, D.J. Jones, J. Rozière, Electrospinning: designed architectures for energy conversion and storage devices, Energy & Environmental Science 4(12) (2011) 4761-4785.
[273] K.M. Yun, C.J. Hogan, Y. Matsubayashi, M. Kawabe, F. Iskandar, K. Okuyama, Nanoparticle filtration by electrospun polymer fibers, Chemical Engineering Science 62(17) (2007) 4751-4759.
[274] R. Gopal, S. Kaur, Z. Ma, C. Chan, S. Ramakrishna, T. Matsuura, Electrospun nanofibrous filtration membrane, Journal of Membrane Science 281(1) (2006) 581-586.
[275] H. Yoshimoto, Y. Shin, H. Terai, J. Vacanti, A biodegradable nanofiber scaffold by electrospinning and its potential for bone tissue engineering, Biomaterials 24(12) (2003) 2077-2082.
[276] D. Grafahrend, K.-H. Heffels, M.V. Beer, P. Gasteier, M. Möller, G. Boehm, P.D. Dalton, J. Groll, Degradable polyester scaffolds with controlled surface chemistry combining minimal protein adsorption with specific bioactivation, Nature materials 10(1) (2011) 67-73.
[277] J. Groll, T. Ameringer, J.P. Spatz, M. Moeller, Ultrathin coatings from isocyanate-terminated star PEG prepolymers: layer formation and characterization, Langmuir 21(5) (2005) 1991-1999.

[278] S.E. Haynesworth, J. Goshima, V.M. Goldberg, A.I. Caplan, Characterization of cells with osteogenic potential from human marrow, Bone 13(1) (1992) 81-88.

[279] K. Klinkhammer, N. Seiler, D. Grafahrend, J. Gerardo-Nava, J. Mey, G.A. Brook, M. Möller, P.D. Dalton, D. Klee, Deposition of electrospun fibers on reactive substrates for in vitro investigations, Tissue Engineering Part C: Methods 15(1) (2008) 77-85.

[280] D. Gross, W. Hauger, J. Schröder, W.A. Wall, J. Bonet, Engineering Mechanics 2: Mechanics of Materials, Springer Science & Business Media (2011).

[281] D. Ahmed, Z. Hongpeng, K. Haijuan, L. Jing, M. Yu, Y. Muhuo, Microstructural developments of poly (p-phenylene terephthalamide) fibers during heat treatment process: a review, Materials Research 17(5) (2014) 1180-1200.

[282] V. Gupta, V. Kothari, Manufactured fibre technology, Springer Science & Business Media (2012).

[283] C. Lim, E. Tan, S. Ng, Effects of crystalline morphology on the tensile properties of electrospun polymer nanofibers, Applied Physics Letters 92(14) (2008) 141908.

[284] A. Baji, Y.-W. Mai, S.-C. Wong, M. Abtahi, P. Chen, Electrospinning of polymer nanofibers: effects on oriented morphology, structures and tensile properties, Composites science and technology 70(5) (2010) 703-718.

[285] J.J. Weeks, Melting temperature and change of lamellar thickness with time for bulk polyethylene, J. Res. Natl Bur. Stand. A 67(5) (1963) 441-451.

[286] G. Gottstein, Physical foundations of materials science, Springer Science & Business Media (2013).

[287] V. Korsukov, V. Marichin, L. Miasnikova, I. Novak, The influence of supermolecular structure on linear polyethylene drawing, Journal of Polymer Science: Polymer Symposia, Wiley Online Library, 1973, 847-853.

[288] G.H. Michler, F.J. Baltá-Calleja, Nano-and micromechanics of polymers: structure modification and improvement of properties, Carl Hanser Verlag GmbH Co KG (2012).

[289] P.-T. Brun, B. Audoly, N.M. Ribe, T.S. Eaves, J.R. Lister, Liquid ropes: a geometrical model for thin viscous jet instabilities, Phys Rev Lett 114(17) (2015) 174501.

[290] N.M. Ribe, M. Habibi, D. Bonn, Liquid rope coiling, Annual review of fluid mechanics 44 (2012) 249-266.

[291] P.-T. Brun, N.M. Ribe, B. Audoly, A numerical investigation of the fluid mechanical sewing machine, Physics of Fluids (1994-present) 24(4) (2012) 043102.

[292] S.W. Morris, J.H. Dawes, N.M. Ribe, J.R. Lister, Meandering instability of a viscous thread, Physical Review E 77(6) (2008) 066218.

[293] N. Ribe, H. Huppert, M. Hallworth, M. Habibi, D. Bonn, Multiple coexisting states of liquid rope coiling, Journal of Fluid Mechanics 555 (2006) 275-297.

[294] N.M. Ribe, Coiling of viscous jets, Proceedings of the Royal Society of London A: Mathematical, Physical and Engineering Sciences, The Royal Society, 2004, 3223-3239.

[295] L. Govaert, T. Peijs, Tensile strength and work of fracture of oriented polyethylene fibre, Polymer 36(23) (1995) 4425-4431.

[296] M. Bergou, B. Audoly, E. Vouga, M. Wardetzky, E. Grinspun, Discrete viscous threads, ACM Transactions on Graphics (TOG), ACM, 2010, 116.

[297] M.A. Woodruff, D.W. Hutmacher, The return of a forgotten polymer—polycaprolactone in the 21st century, Progress in Polymer Science 35(10) (2010) 1217-1256.

[298] G.W. Ehrenstein, Polymeric materials: structure, properties, applications, Carl Hanser Verlag GmbH Co KG (2012).

[299] L. Wang, W. Ma, R. Gross, S. McCarthy, Reactive compatibilization of biodegradable blends of poly (lactic acid) and poly (ε-caprolactone), Polymer Degradation and Stability 59(1-3) (1998) 161-168.

[300] J. Atance, M.J. Yost, W. Carver, Influence of the extracellular matrix on the regulation of cardiac fibroblast behavior by mechanical stretch, Journal of cellular physiology 200(3) (2004) 377-386.

[301] C.B. Khatiwala, S.R. Peyton, A.J. Putnam, Intrinsic mechanical properties of the extracellular matrix affect the behavior of pre-osteoblastic MC3T3-E1 cells, American Journal of Physiology-Cell Physiology 290(6) (2006) C1640-C1650.

[302] D.E. Discher, D.J. Mooney, P.W. Zandstra, Growth factors, matrices, and forces combine and control stem cells, Science 324(5935) (2009) 1673-1677.

[303] D.E. Discher, P. Janmey, Y.-l. Wang, Tissue cells feel and respond to the stiffness of their substrate, Science 310(5751) (2005) 1139-1143.

[304] G. Chen, C. Dong, L. Yang, Y. Lv, 3D scaffolds with different stiffness but the same microstructure for bone tissue engineering, ACS applied materials & interfaces 7(29) (2015) 15790-15802.

[305] R.G. Breuls, T.U. Jiya, T.H. Smit, Scaffold stiffness influences cell behavior: opportunities for skeletal tissue engineering, The open orthopaedics journal 2(1) (2008) 103-109.

[306] J.A. Brydson, Plastics materials, Butterworth-Heinemann (1999).

[307] H.E. Meijer, L.E. Govaert, Mechanical performance of polymer systems: The relation between structure and properties, Progress in polymer science 30(8) (2005) 915-938.

[308] J.R. Martin, J.F. Johnson, A.R. Cooper, Mechanical properties of polymers: the influence of molecular weight and molecular weight distribution, Journal of Macromolecular Science—Reviews in Macromolecular Chemistry 8(1) (1972) 57-199.
[309] I.M. Ward, J. Sweeney, Mechanical properties of solid polymers, John Wiley & Sons (2012).
[310] J.E. Mark, Physical properties of polymers handbook, Springer (2007).
[311] M.P. Hiljanen-Vainio, P.A. Orava, J.V. Seppälä, Properties of ϵ-caprolactone/DL-lactide (ϵ-CL/DL-LA) copolymers with a minor ϵ-CL content, Journal of biomedical materials research 34(1) (1997) 39-46.
[312] C. Martins, V. Pinto, R.M. Guedes, A.T. Marques, Creep and Stress Relaxation Behaviour of PLA-PCL Fibres–A Linear Modelling Approach, Procedia Engineering 114 (2015) 768-775.
[313] A. Vieira, R. Medeiros, R.M. Guedes, A. Marques, V. Tita, Visco-elastic-plastic properties of suture fibers made of PLA-PCL, Materials Science Forum, Trans Tech Publ, 2013, 56-61.
[314] D.C. Surrao, S.D. Waldman, B.G. Amsden, Biomimetic poly (lactide) based fibrous scaffolds for ligament tissue engineering, Acta biomaterialia 8(11) (2012) 3997-4006.
[315] M. Azevedo, R. Reis, M. Claase, D. Grijpma, J. Feijen, Development and properties of polycaprolactone/hydroxyapatite composite biomaterials, Journal of materials science: Materials in medicine 14(2) (2003) 103-107.
[316] D. Puppi, N. Detta, A.M. Piras, F. Chiellini, D.A. Clarke, G.C. Reilly, E. Chiellini, Development of Electrospun Three-arm Star Poly (ε-caprolactone) Meshes for Tissue Engineering Applications, Macromolecular bioscience 10(8) (2010) 887-897.
[317] R.F. Landel, L.E. Nielsen, Mechanical properties of polymers and composites, CRC Press (1993).
[318] G. Holzapfel, J. Simo, Entropy elasticity of isotropic rubber-like solids at finite strains, Computer Methods in applied mechanics and engineering 132(1) (1996) 17-44.
[319] Y. Wang, G.A. Ameer, B.J. Sheppard, R. Langer, A tough biodegradable elastomer, Nature biotechnology 20(6) (2002) 602-606.
[320] A. Moshiri, A. Oryan, Tendon and ligament tissue engineering, healing and regenerative medicine, Journal of Sports Medicine & Doping Studies 3(2) (2013) 1000126.
[321] C.N. Maganaris, J.P. Paul, In vivo human tendon mechanical properties, The Journal of physiology 521(1) (1999) 307-313.
[322] F. Chen, G. Hochleitner, T. Woodfield, J. Groll, P.D. Dalton, B.G. Amsden, Additive manufacturing of a photo-cross-linkable polymer via direct melt

electrospinning writing for producing high strength structures, Biomacromolecules 17(1) (2015) 208-214.
[323] V. Mucci, C. Vallo, Efficiency of 2, 2-dimethoxy-2-phenylacetophenone for the photopolymerization of methacrylate monomers in thick sections, Journal of Applied Polymer Science 123(1) (2012) 418-425.
[324] D.L. Kurdikar, N.A. Peppas, Method of determination of initiator efficiency: application to UV polymerizations using 2, 2-dimethoxy-2-phenylacetophenone, Macromolecules 27(3) (1994) 733-738.
[325] D. Meschede, Gerthsen physik, Springer-Verlag (2015).
[326] J. Vlachopoulos, D. Strutt, The role of rheology in polymer extrusion, New Technology for Extrusion Conference. Milan, Italy. Nov, 2003, 20-21.
[327] G. Hochleitner, F. Chen, C. Blum, P.D. Dalton, B.G. Amsden, J. Groll, Melt electrowriting below the critical translation speed to fabricate crimped elastomer scaffolds with non-linear extension behaviour mimicking that of ligaments and tendons, Acta Biomaterialia 72 (2018) 110-120.
[328] J. Magill, Review Spherulites: A personal perspective, Journal of Materials Science 36(13) (2001) 3143-3164.
[329] L. Gránásy, T. Pusztai, G. Tegze, J.A. Warren, J.F. Douglas, Growth and form of spherulites, Physical Review E 72(1) (2005) 011605.
[330] J. Kastelic, I. Palley, E. Baer, A structural mechanical model for tendon crimping, J Biomech 13(10) (1980) 887-93.
[331] C. Yilgor, P. Yilgor Huri, G. Huri, Tissue engineering strategies in ligament regeneration, Stem cells international 2012 (2011) 374676.
[332] C.K. Kuo, J.E. Marturano, R.S. Tuan, Novel strategies in tendon and ligament tissue engineering: advanced biomaterials and regeneration motifs, BMC Sports Science, Medicine and Rehabilitation 2(1) (2010) 1.
[333] D. Kirkendall, W. Garrett, Function and biomechanics of tendons, Scandinavian journal of medicine & science in sports 7(2) (1997) 62-66.
[334] L. Papula, Mathematische Formelsammlung für Ingenieure und Naturwissenschaftler, Springer (2006).
[335] J.H.-C. Wang, Mechanobiology of tendon, Journal of biomechanics 39(9) (2006) 1563-1582.
[336] L. David, E.S. Grood, F.R. Noyes, R.E. Zernicke, Biomechanics of ligaments and tendons, Exercise and sport sciences reviews 6(1) (1978) 125-182.
[337] L. Xu, N. Sheybani, W.A. Yeudall, H. Yang, The effect of photoinitiators on intracellular AKT signaling pathway in tissue engineering application, Biomaterials science 3(2) (2015) 250-255.
[338] I. Mironi-Harpaz, D.Y. Wang, S. Venkatraman, D. Seliktar, Photopolymerization of cell-encapsulating hydrogels: crosslinking efficiency versus cytotoxicity, Acta biomaterialia 8(5) (2012) 1838-1848.

10 Acknowledgements

First of all, I would like to thank Prof. Dr. Jürgen Groll sincerely for his supervision and his great support. He believed in me and my work, guided me through science, ever had a sympathetic ear for me and provided all the necessary little and big things a PhD student needs: money, place and a fascinating topic. Here, I also want to thank Prof. Dr. Robert Luxenhofer for supporting me and spending his valuable time for assessing my thesis.

Further, I also want to thank Prof. Dr. Paul Dalton for spending hours in very creative discussions showing how much fun applied science can be. I learned a lot from him, how to write and present in a simple and efficient way for instance. I want to point this out, because we do science for everyone and not just for ourselves.

In addition, I would like to thank all my colleagues from the FMZ department making it a wonderful place to work at. As my colleagues, I had years full of ups and downs including vociferous conflicts, nearly despair, but also burning enthusiasm and hugs full of joy – everything that life entails and everything that young people need to experience to grow a bit older. I'm not exaggerating to say I'm really grateful for a good time, learning incredible much about research, but also about myself and last but not least, I found friends.

Because it is not possible to list all the people, a brief summary only. My warm thanks to Almoatazbellah "Moataz" Youssef, Dr. Ana Sancho, Andrei Hrynevich, Anton "Toni" Hofmann, Carina Blum, Dr. Claus Moseke, Christoph Böhm, Dr. Elke Vorndran, Harald Hümpfer, Judith Friedlein, Julia Hümmer, Dr. Kai Stuckensen, Dr. Matthias Kuhlmann, Dr. Michael Schmitz, Mylene de Ruijter, Tanja Dambach, Theresa Brückner, Tomasz Jüngst and Prof. Dr. Uwe Gbureck.

At this point, I want to particularly thank my like-minded colleagues and friends Markus and Susanne “Susi” Meininger as well as Manuel Roesener. These guys spend countless lunch times with me, deepened in discussions about this and that and listened when I was frustrated or upset and needed someone to vent off.

Here, I further want to say thanks to the two special and selfless colleagues Isabell Biermann and Dr. Jörg Teßmar, both cornerstones of a well running department. Without these both a lot of things would have went worse, if at all.

Moreover, I don’t want to forget all the interesting people I met at conferences, seminars, business travels or even here in Würzburg. They made me feeling welcome wherever I went and were sincerely willing to help me. Thus, especially thanks to Prof. Dr. Brian Amsden, Dr. Miguel Castilho, Dr. Pedro Costa and Dr. Riccardo Levato.

Last but not least, I want to thank my family for helping me, loving me, supporting me, believing in me and sometimes even enduring me. Without my wife, I wouldn’t be at this point now. Thanks Sara for spending and sharing your life with me, you make my life worth living.

11 Supplementary Information

11.1 G-code files

11.1.1 PEtOx fibre scaffolds[136]

11.1.1.1 G-code of the scaffold shown in Figure 35 B on page 81

```
G17 G21 G40 G49 G54 G80 G94 G91
m98 p1
m98 p6 l90
m98 p7
m30
o1
g1                  x0                  y0                                      f400
g4 p1
m99
o2
g1                  x-40.000            y0                                      f400
g1                  x0                  y-0.250                                 f10
g1                  x40.000             y0                                      f400
g1                  x0                  y-0.250                                 f10
m99
o3
g1                  x-40.000            y0                                      f400
g4 p1
g1                  x0                  y-15.000                                f400
g1                  x15.000             y0                                      F400
g4 p1
m99
o4
g1                  x0                  y40.000                                 f400
g1                  x0.250              y0                                      f10
g1                  x0                  y-40.000                                f400
g1                  x0.250              y0                                      f10
m99
o5
g1                  x0                  y15.000                                 f400
g4 p1
g1                  x15.000             y0                                      f400
g1                  x0                  y-15.000                                F400
g4 p1
m99
o6
m98 p2 l20
m98 p3
m98 p4 l20
m98 p5
m99
o7
g4 p1
g1                  x0.250              y0.250                                  f400
m99
```

11.1.1.2 G-code of the scaffold shown in Figure 35 C-F on page 81

```
G17 G21 G40 G49 G54 G80 G94 G91
m98 p1
m98 p6 l15
m98 p7
m30
o1
g1              x0              y0                              f400
g4 p1
m99
o2
g1              x-80.000        y0                              f400
g1              x0              y-0.500                         f150
g1              X80.000         y0                              f400
g1              x0              y-0.500                         f150
m99
o3
g1              x-80.000        y0                              f400
g4 p2
g1              x0              y-35.000                        f400
g4 p1
g1              x35.000         y0                              F400
g4 p3
m99
o4
g1              x0              y80.000                         f400
g1              x0.500          y0                              f150
g1              x0              y-80.000                        f400
g1              x0.500          y0                              f150
m99
o5
g1              x0              y80.000                         f400
g4 p2
g1              x35.000         y0                              f400
g4 p1
g1              x0              y-35.000                        F400
g4 p3
m99
o6
m98 p2 l10
m98 p3
m98 p4 l10
m98 p5
m99
o7
g4 p1
g1              x0.50           y0.50                           f400
m99
```

11.1.2 Submicron PCL fibre scaffolds[129]

11.1.2.1 G-code of the scaffold shown in Figure 40 on page 98

```
G17 G21 G40 G49 G54 G80 G94 G91
m98 p1
m98 p6 l50
m98 p7
m30
o1
g01             x-1.500         y-1.500                         f5500
g4 p1
m99
o2
g01             x-15.000        y0                              f5500
g03             x0              y-0.100         r-0.500         f1000
g01             x15.000         y0                              f5500
g02             x0              y-0.100         r-0.500         f1000
m99
o3
g01             x-15.000        y0                              f5500
m99
o4
g01             x0              y15.000                         f5500
g02             x0.100          y0              r-0.500         f1000
g01             x0              y-15.000                        f5500
g03             x0.100          y0              r-0.500         f1000
m99
o5
g01             x0              y15.000                         f5500
m99
o6
m98 p2 l75
m98 p3
m98 p4 l75
m98 p5
m99
o7
g4 p1
g1              x3.000          y3.000                          f5500
m99
```

11.1.3 Printing below CTS

11.1.3.1 Line array example for pattern quantification

```
G17 G21 G40 G49 G54 G80 G94 G91
m98 p1
m98 p2
m30
o1
g01 x-1.000      y-1.000    f200
g4 p1
m99
o2
g01                 x-50.000            y0                                      f50
g03                 x0                  y-0.100             r-0.500             f200
g01                 x50.000             y0                                      f50
g02                 x0                  y-0.100             r-0.500             f200
      ⇨     REPITITION (5 times in total) …
g01                 x-50.000            y0                                      f75
g03                 x0                  y-0.100             r-0.500             f200
g01                 x50.000             y0                                      f75
g02                 x0                  y-0.100             r-0.500             f200
      ⇨     REPITITION (5 times in total) …
…
      ⇨     Δf+25 until CTS has been matched
m99
```

11.1.3.2 Scaffold example for mechanical testing

```
DVAR $VarX $VarY $VarZ
$VarX = 0
$VarY = 0
$VarZ = 0
ENABLE X Y Z
VELOCITY off
CALL rein
WHILE $VarZ LT 5
        CALL layer
        $VarZ = $VarZ + 1
        DWELL 0.3
ENDWHILE
CALL raus
Velocity off
END PROGRAM
DFS layer
        WHILE $VarX LT 50
                CALL linieX
                $VarX = $VarX +1
                IF $VarX = 50 THEN
                        Linear      X-30.000   Y0                        F1.9
                        DWELL 0.3
                        Linear                            Z0.000         F0.5
                ENDIF
        ENDWHILE
```

```
          WHILE $VarY LT 50
                    CALL linieY
                    $VarY = $VarY +1
                    IF $VarY EQ 50 THEN
                              Linear    X0        Y30.000             F1.9
                              DWELL 0.3
                              Linear                        Z0.000    F0.5
                    ENDIF
          ENDWHILE
$VarX = 0
$VarY = 0
ENDDFS
DFS rein
          LINEAR X-3.000      Y-3.000                                 F1.9
          DWELL 0.3
ENDDFS
VELOCITY off
DFS linieX
          LINEAR    X-30.000            Y0                            F1.9
          CCW       X0                  Y-0.300   R0.3000             F1.9
          LINEAR    X30.000             Y0                            F1.9
          CW        X0                  Y-0.300   R0.3000             F1.9
ENDDFS
DFS linieY
          Linear    X0                  Y30.000                       F1.9
          CW        X0.300              Y0        R0.3000             F1.9
          Linear    X0                  Y-30.000                      F1.9
          CCW       X0.300              Y0        R0.3000             F1.9
ENDDFS
DFS raus
          LINEAR    X3.000              Y3.000                        F1.9
          DWELL 0.3
ENDDFS
Velocity off
```

11.2 Surface coating SOP

VORBEREITUNG:

- Rückseite mit **R** markieren
- Splitter entfernen mit staubfreiem Tuch (DASTEX) + Isopropanol
- Substrate in Träger, REINIGUNG in Ultraschallbad (jeweils ca. 10 min):
    - Aceton
    - Dest. H_2O
    - Isopropanol
- Substrate mit Druckluft trocknen

AKTIVIERUNG:

- Ätzen der Glasoberfläche mit Piranha (H_2O_2:H_2SO_4, 1:2) → Glassubstrate in Träger, 30 mL H_2O_2 in Becherglas, Glassubstrate hinzu, 60 mL H_2SO_4 hinzu → 30 min.
- Träger in H_2O (millipore), 3-4 mal Wasserwechsel (bis pH = neutral)
- Substrate mit Druckluft trocknen
- Exsikkator mit 3-Aminopropyl-trimethoxysilan in Uhrglas bestücken (≈ 100 µL)
- Träger in Petrischalen hinzu (Richtige Seite Oben)
- Vakuum auf ≈ 100 mbar einstellen
- Über Nacht stehen lassen
- Nächsten Tag belüften

BESCHICHTUNG:

- Lösung ansetzen:
    - 25 mg sPEG („echtes“, SS30A aus Kühlschrank)
    - In 250 µL THF **lösen**
    - **erst dann:** 2.25 mL H_2O hinzu! NICHT rühren, nur einmal kurz umdrehen
- Lösung 5 min. vorvernetzen
- Beschichten der Wafer mit sPEG-Lösung:
    - 1 mL Spritze mit Spritzenfilter (0.5 µm) für 5-6 Wafer (Rest der Lsg. wird verworfen!)
    - Spin-Coater mit Programm „Run static“ (→40 sek bei 2500 Rpm)
    -